

# $\eta$ production in p+p reactions in the HADES spectrometer at 2.2 GeV

Inaugural-Dissertation  
zur Erlangung des Doktorgrades der Naturwissenschaften  
der Justus Liebig Universität Gießen  
Fachbereich 07 (Mathematik und Informatik, Physik, Geographie)

vorgelegt von

**Tiago Pérez Cavalcanti**  
aus Rio de Janeiro (Brasilien)

II. Physikalisches Institut  
der Justus Liebig Universität Gießen  
27th July 2006

Dekan: Prof. Dr. V. Metag

I. Berichterstatter: Prof. Dr. W. Kühn

II. Berichterstatter: Prof. Dr. Dr. W. Cassing

Tag der mündlichen Prüfung: 29th August 2006

# Zusammenfassung

Das HADES (High Acceptance DiElectron Spectrometer) Experiment an der GSI (Gesellschaft für Schwerionenforschung) in Darmstadt untersucht die Produktion von Mesonen in Proton-Proton- und Kern-Kern-Reaktionen bei Strahlenergien von 1-4 GeV. Im Rahmen dieser Arbeit wurde eine technische Fragestellung und eine physikalische Fragestellung für HADES bearbeitet.

Im Rahmen der technischen Fragestellung wurde eine neue Firmware für Teile des HADES Trigger Systems, sogenannte Detector Trigger Units (DTU), entwickelt. Das ursprünglich als elektrischer Schaltkreis fixierte DTU Design wurde in eine Hochsprache (VHDL) zur Definition von Logik-Schaltungen übertragen, und auf einem FPGA (Field Programmable Gate Array) implementiert. Diese Implementation ermöglicht die Integration neuer Detektoren in das HADES Trigger System, wie z.B. eines geplanten hochauflösenden RPC-Flugzeitdetektors mit 1024 Modulen.

Im Rahmen der physikalischen Fragestellung ist mit einer Datenanalyse die Produktion von eta-Mesonen in Proton-Proton-Stößen bei einer Strahlenergie von 2.2 GeV untersucht worden. Dabei wurden der hadronische Zerfall  $\eta \rightarrow \pi^+\pi^-\pi^0$  und erstmals an HADES auch der Zerfall  $\eta \rightarrow \pi^+\pi^-\gamma$  beobachtet. Mit Methoden von Analysen von Drei-Teilchen-Entzuständen (Dalitzplots) konnte mit der hohen Statistik (etwa 10 mal mehr eta Mesonen als vorherige Experimente) bestätigt werden, dass als dominanter Prozess der Produktion von eta Mesonen bei der vorliegenden Strahlenergie über die Nukleonenresonanz  $N^*(1535)$  vorliegt.



# Abstract

The HADES spectrometer had had its first production proton–proton beam time in January 2004. The major physical topics during this run were the reconstruction of the  $\eta$  and  $\pi^0$  mesons.

In this work, the reconstruction of the  $\eta$  meson via the analysis of its hadronic decays will be presented.

HADES has been designed to perform high resolution dielectron spectroscopy. For that purpose a dedicated online trigger system has been developed. The HADES trigger system is divided into two levels. The first level trigger performs a selection of central collisions based on the multiplicity. The second level trigger can select, online,  $e^+e^-$  pairs in a certain invariant mass region, enhancing this way the dielectron content of the recorded data sample.

The fast and reliable distribution of trigger signals is of vital importance to achieve high performance. During the course of this work, new firmware for the detector trigger units (DTU) has been developed. A thorough description of the trigger system, including the developments for the trigger distribution, as well as a discussion of the its performance will be shown.



# Contents

<b>I</b>	<b>Motivation</b>	<b>11</b>
<b>1</b>	<b>Introduction</b>	<b>13</b>
<b>2</b>	<b>Quantum Chromo Dynamics</b>	<b>17</b>
2.1	Chiral Symmetry . . . . .	19
2.1.1	Broken Symmetry . . . . .	20
2.2	In-Medium Effects . . . . .	21
2.2.1	Chiral Symmetry Restoration . . . . .	22
2.2.2	Hadronic Scenario . . . . .	24
<b>3</b>	<b>Probing In-Medium Effects</b>	<b>27</b>
3.1	Dilepton Spectroscopy . . . . .	27
3.2	HADES . . . . .	33
<b>II</b>	<b>The HADES Detector System</b>	<b>35</b>
<b>4</b>	<b>The Spectrometer</b>	<b>37</b>
4.1	Overview . . . . .	37
4.2	The Single Detectors . . . . .	39
4.2.1	The Targets . . . . .	39
4.2.2	The START and VETO detectors . . . . .	41
4.2.3	Ring Image Cherenkov Detector . . . . .	41
4.2.4	The Tracking System . . . . .	44
4.2.5	The META . . . . .	46
4.3	New Developments . . . . .	51
4.3.1	Resistive Plate Chambers: RPC . . . . .	51
<b>5</b>	<b>The Trigger System</b>	<b>53</b>
5.1	The First Level Trigger: Centrality Trigger . . . . .	54
5.2	The Second Level Trigger: Lepton Trigger . . . . .	55

5.2.1	The RICH Image Processing Unit . . . . .	56
5.2.2	The TOF Image Processing Unit . . . . .	58
5.2.3	The Shower IPU . . . . .	60
5.2.4	The Matching Unit . . . . .	62
5.3	The Trigger Distribution System . . . . .	64
5.3.1	The Trigger Bus . . . . .	65
5.3.2	The CTU/DTU Hardware . . . . .	67
5.3.3	The DTU logic . . . . .	68
5.4	Trigger Performance . . . . .	71
<b>III</b>	<b>Analysis of Elementary Reactions with HADES</b>	<b>75</b>
<b>6</b>	<b>The Analysis Software Framework</b>	<b>77</b>
6.1	Data Flow . . . . .	77
6.2	The Event Reconstruction Framework . . . . .	78
6.2.1	Overview . . . . .	79
6.2.2	The HYDRA Structure . . . . .	81
<b>7</b>	<b>The Event Hypothesis</b>	<b>85</b>
7.1	Overview . . . . .	85
7.2	Software Structure . . . . .	86
7.3	The “Delta TOF” Algorithm . . . . .	88
<b>8</b>	<b>Exclusive Reconstruction of the <math>\eta</math> Meson</b>	<b>91</b>
8.1	Introduction . . . . .	91
8.2	Reaction Overview . . . . .	92
8.3	Reconstruction of the $\eta \rightarrow \pi^+\pi^-\pi^0$ Channel . . . . .	95
8.3.1	Identification of the Missing $\pi^0$ . . . . .	96
8.3.2	Identification of $\eta$ . . . . .	98
8.3.3	$\eta$ Angular Distribution. . . . .	100
8.3.4	Dalitz Plot . . . . .	101
8.4	Reconstruction of the $\eta \rightarrow \pi^+\pi^-\gamma$ Channel . . . . .	102
8.4.1	Missing Mass. . . . .	103
8.4.2	Missing Momentum. . . . .	104
8.4.3	Simulations. . . . .	106
8.4.4	Energy Distribution of the Missing Gamma. . . . .	108
8.5	Comparison $\eta_\gamma/\eta_{\pi^0}$ . . . . .	111

# Preface

In the last decades, experimental nuclear and particle physicists have had a great influence in the development of modern technologies. With any new generation of detectors together with accelerator facilities, continuously more demanding requirements on speed and load made physicist become leading edge researches in electronics (DAQ, Trigger...) as well as in computer science (Data Analysis). In this latter field, physicist have been traditionally, together with meteorologists, the most intensive users of all the supercomputer facilities all around the world. Now, due to the extreme challenging requirements of the experiments planned for the new accelerator facility at CERN, the Large Hadron Collider (LHC), the nuclear physics community had become the leader of one of the most successful developments on computer science in the last years, the GRID.

In this line, it has been fun to participate in the re-elaboration of the firmware for the trigger distribution system units of HADES, as well as to participate in the development of the RCU modules for the ALICE FMD detector. Everything related to the HADES trigger system and electronic developments can be found in chapter 5.

The data analysis involved in the results presented in chapter 8 also implied a long term contact with large and complex software frameworks. This has been gratifying sometimes but very often irritating. Nevertheless, it has been for sure an enriching experience.

Besides these technicalities, probably, only interesting for experimentalist, the major reason and motivation of this works was the eager to know, or at least to get an idea, of the fundamental questions of nature. The origin of the so heavy baryonic masses, responsible for more than 99.9 % of the mass we *see*, the nature of the *dark matter* or why there is matter instead of anti-matter in the cosmos, are some of those questions.

In the next chapter, some of these astrophysical unknowns will be presented. The aim of the chapter is to introduce the work into the context of the whole without going deep into details. Anyhow, the reader is encouraged to follow the citations for more information, some of them really enjoyable.

More scientific rigour will be found in chapter 2. Here, some aspects of Quantum Chromo Dynamics (QCD), the theory of the strong interaction, the interaction between protons and neutrons, will be discussed. Especially those aspects dealing with chiral symmetry and the properties of hadrons in media with finite temperature and density, as those aspects are the most relevant for the experimental results presented, finally, in chapter 8.

Part I  
Motivation



# Chapter 1

## Introduction

Why is there more matter than antimatter? What is the nature of *Dark Matter*? Where does the heavy mass of the Baryons come from? And how to unify Quantum mechanics and General Relativity in a general theory? These are probably the major topics that, in the beginning of the XXI century, we are missing in order to understand the nature.

It is not the purpose of the present work to give answers to all those questions, but to contribute with some experimental results which may help the physics community to understand the strong interaction better.

### **Dark Matter.**

In 1933 F. Zwicky realised that the velocity dispersion in rich clusters of galaxies require between 10 to 100 times more gravitational mass than the one accounted by the luminous galaxies themselves [Zwi33]. The most external stars move much too fast than predicted by Newtons dynamics (eq. 1.1) and too fast to be kept in the galaxies by the gravitation of the visible matter (see figure 1.1).

$$v = \sqrt{\frac{GM(r)}{r}} \quad (1.1)$$

Moreover gravitational dark matter is also required in order to enable gravity to amplify the small fluctuations in the Cosmic Microwave Background (figure 1.2) enough to form the large-scale structures that we see in the universe today. A nice review can be found in [Ber04].

Several ideas and models have been developed to address that problem. Some propose modifications of the Newtonian dynamics at low velocities [Mil83] and others assume the existence of some *hidden* gravitational mass, *Dark*

*Matter.* From the latter, several sources have been postulated as ingredients of that hidden mass. They can be divided into two major groups :

**Baryonic :** MACHOs (Massive Astrophysical Compact Halo Objects).

**Non Baryonic :** WIMPS, Axions, Massive Neutrinos...

Several experimental evidences have been found in the last years that corroborate the existence of massive compact objects: *Brown Dwarfs*, *Neutron Stars* and *Black Holes*. They are certainly responsible for part of the missing mass-energy. Even though it is not yet clear in which percentage.

The existence of massive particles with extremely small electromagnetic cross sections of non baryonic nature, and therefore non strong interacting, may account for the rest of the non detected mass-energy in the Cosmos. Among them we have massive neutrinos, axions and the so called *Weakly Interactive Massive Particles* [Eid04] or WIMPS.

It is very unlikely that any of the presented processes alone could explain the origin of all dark matter. But rather a combination of several processes may do it.

## Baryogenesis

The Dirac equation [Dir28], formulated by Paul Dirac in 1928 as part of the development of relativistic quantum mechanics, predicts the existence of antiparticles along with the expected solutions for the corresponding particles. Since then, it has been verified experimentally that every particle has a corresponding antiparticle. The CPT Theorem implies that a particle and its anti-particle have exactly the same mass and lifetime, and exactly the opposite charge. Given this symmetry, it is unsettling that the universe does not have equal amounts of matter and antimatter. Indeed, there is no evidence that there are any significant concentrations of antimatter in the observable universe.

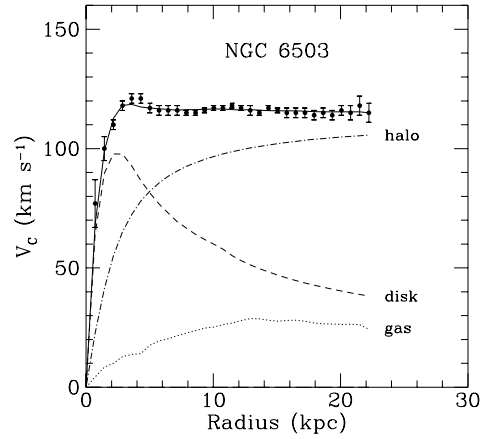


**Figure 1.1:** Rotation curve of NGC 6503. The dotted, dashed and dash-dotted lines are the contributions of gas, disk and dark matter, respectively [Beg91].

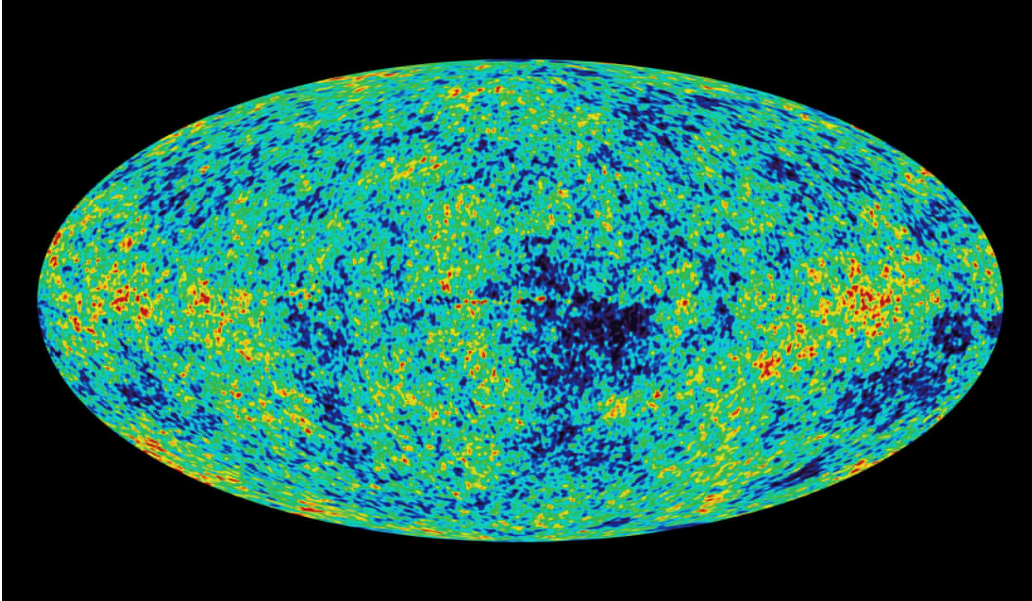


**Figure 1.2:** The Cosmic Microwave Background, CMB. From [NAS].

### Origin of the Mass

In the Standard Model [Gla61, Wei67] the electroweak interaction is described by a gauge field theory based on the  $SU(2)_L \times U(1)_Y$  symmetry group. In this theory, the mass of the elementary particles is obtained through the Higgs mechanism [Hig64], i.e. the spontaneous symmetry breaking of the ground state of the system leads to the existence of, at least, one massive gauge field and its associated boson, the Higgs particle or boson.

Higgs boson has not been observed yet. Its mass is unknown and it cannot be calculated. Anyhow, estimations have been drawn based upon measurements of electroweak observables like the masses of the top quark and the  $W^\pm$  bosons. They have set an upper limit for the Higgs boson at  $m_{H^0} \leq 219$  GeV at the 95 % confidence level [LEP05]. Experimentally, a lower bound has been determined by the detectors in the *Large Electron Positron Collider* (LEP) at CERN. ALEPH, DELPHI, L3 and OPAL jointly reached a sensitivity to the Higgs mass up to about 117 GeV [Eid04].

Nowadays, the *Tevatron* [Tev] collider located at the Fermi National Accelerator Laboratory (USA) with a centre of mass energy of  $\sqrt{s} = 2$  TeV and, in the near future, the *Large Hadron Collider* [LHC] at CERN (Switzerland) with  $\sqrt{s}$  up to 14 TeV should have enough energy to produce Higgs particles in sufficient quantity so that some experiments, CDF and CØ (Tevatron) and

ATLAS and CMS (LHC) should be sensitive to detect their decays.

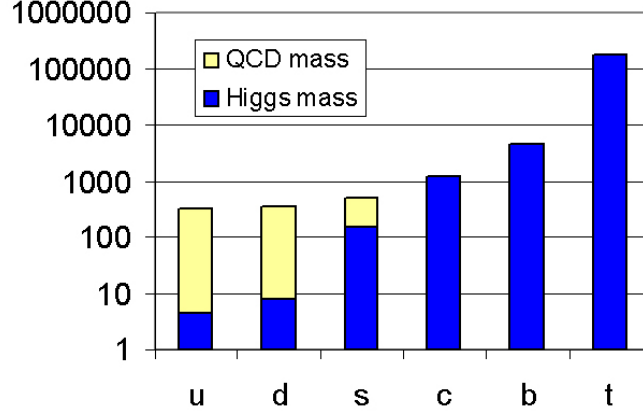


**Figure 1.3:** Masses of the six quark flavours. Masses generated by electroweak symmetry breaking (*current quark mass*) are shown in blue. The additional term portion of the light quarks mass, generated by chiral symmetry breaking in QCD (*constituent quark mass*) are shown in yellow [Mul04].

The Higgs mechanism explained before, is responsible for the mass of leptons, bosons of the weak interaction and, partially, quarks. This is the so called *current quark mass* or mass of *naked* quarks ( $m_{u,d} \sim 5$  MeV [Eid04]). Nevertheless, the heavy mass of baryons deviates strongly from the naïf sum of three light quarks.

Quark masses receive additional contributions from the quark and gluon condensates in the QCD vacuum [Mul04]. This process, the spontaneous breaking of chiral symmetry (see subsection 2.1.1), is responsible for more than 90% of the mass of the light *up* and *down* quarks [Mul04] (figure 1.3) and it also contributes significantly to the mass of the *strange* quark.

## Chapter 2

# Quantum Chromo Dynamics

Quantum Chromo Dynamics, QCD, is the theory of the strong interaction, the fundamental interaction of quarks and gluons.

In the decade of 1960, the discovery of many hadrons and their ordering in families lead to the postulate by Gell-Mann and Zweig in 1963 that all those particles could not be elementary. They should be composed of point like fermions, quarks.

In QCD, quarks have a *colour charge* with three different states; either red, blue or green. Gluons are vector gauge bosons that mediate colour charge interactions of quarks and, carry one colour and one anti-colour at the same time.

QCD is characterize by two asymptotic cases for different regimes of the quark-quark distance,  $r$ :

**Asymptotic Freedom.** In the limit of zero distance,  $r \rightarrow 0$ , the interaction between quarks become arbitrarily weak. At small distances a quark is surrounded by a infinite number of low momentum virtual gluons which are polarized and lead to screening of the colour potential.

**Confinement.** In the case when  $r \rightarrow \infty$ , the force between quarks increases as the distance between them increases. It would take an infinite amount of energy to separate two quarks. They are, therefore, bound into colour neutral objects called hadrons. Whenever two quarks become separated, at some point it is energetically more favourable to create a quark/anti-quark pair, and hence two new hadrons, than to allow the quarks to separate any further.

Even though in normal conditions quarks are to be confined in hadrons, different states of quark configurations are possible depending upon the tem-

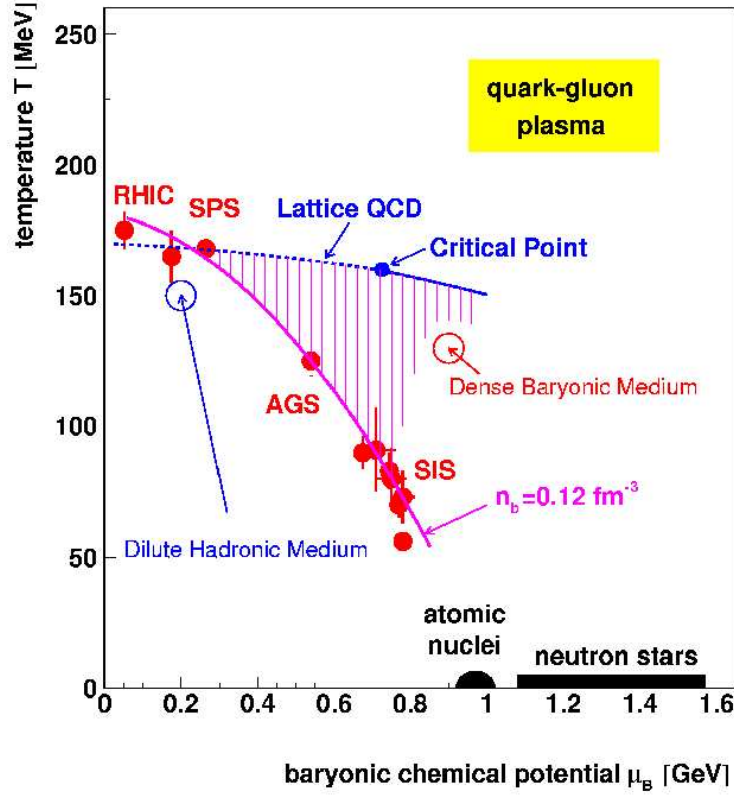


**Figure 2.1:** The QCD phase diagram. Red dots show the experimental freeze-out parameters deduced from hadro-chemical analyses of particle production yields at SIS, AGS and SPS energies [Bra98b, Bra01, Sto99]. The Pink line is the Cleymans-Redlich curve  $E/N = 1\text{ GeV}$  [Cle98]. The blue line represents the phase boundaries calculated from Lattice QCD [Fod01].

perature ( $T$ ), the density ( $\rho$ ) and the barion chemical potential ( $\mu_B$ ). The figure 2.1 shows the QCD phase diagram as a function of  $T$  and  $\mu_B$ . At high temperatures, larger than a critical temperature  $T_c$  predicted to be about 150 – 200 MeV, the elementary quark and gluon degrees of freedom are released from their confinement in hadrons. In that phase, quarks and gluons would be free to move like in an ideal fluid. Below  $T_c$ , and at low baryon density, matter exists only as colour-singlets or aggregates of colour neutral objects, i.e. hadrons.

At very high baryon chemical potential or very large Fermi momenta, it is expected that Cooper pairing of quarks sets in. That would induce to complex patterns of colour superconducting and superfluid phases [Bar77].

Figure 2.1 shows a diagram of the different possible QCD phases. The blue line in the figure depicts the boundary between the deconfined phase and the hadronic phase as calculate by lattice QCD models [Fod01]. The different *freeze-out* points, calculated for several of the accelerator facilities available at the present time, are shown with red dots [Bra98b, Bra01, Sto99]. The pink line, is the curve introduced by Cleymans and Redlich which follows a constant energy density ( $E/N \sim 1$  GeV) [Cle98].

QCD can be described in terms of its Lagrangian as [Fri73] (for simplicity colour, flavor and spin indices are omitted):

$$\mathcal{L}_{QCD} = \bar{\psi}[i\gamma^\mu \mathcal{D}_\mu - m]\psi - \frac{1}{4}G^{\mu\nu}G_{\mu\nu}. \quad (2.1)$$

$\psi$  represents the quark fields,  $\gamma_\mu$  are the Dirac matrices and  $G^{\mu\nu}$  is the gluon field tensor:

$$G_{\mu\nu}^a(x) = \partial_\mu A_\nu^a(x) - \partial_\nu A_\mu^a(x) + gf^{abc}A_\mu^b(x)A_\nu^c(x). \quad (2.2)$$

$D_\mu$  represents the covariant derivative:

$$\mathcal{D}_\mu = \partial_\mu - igA_\mu^j. \quad (2.3)$$

In the equations 2.2 and 2.3, the gluon field is represented by  $A_\mu$  and  $g$  is a dimensionless coupling constant.

## 2.1 Chiral Symmetry

In the limit of massless quarks ( $m = 0$  in eq. 2.1), the QCD Lagrangian exhibits a symmetry related to the conservation of the left- and right-handedness or chirality of the zero-mass spin-1/2 particles. The left- and right-handed quark fields can be written as:

$$\psi_{R,L} = \frac{1}{2}(1 \pm \gamma_5)\psi, \quad (2.4)$$

and we observe that the global unitary transformations of these fields,

$$\psi_R = \exp\left[i\theta_R^a \frac{\lambda_a}{2}\right]\psi_R \quad \text{and} \quad \psi_L = \exp\left[i\theta_L^a \frac{\lambda_a}{2}\right]\psi_L, \quad (2.5)$$

with  $\lambda_a$  ( $a=1,2,3$ ) being the generators of the  $SU(3)$  flavour group, leave the  $\mathcal{L}_{QCD}$  invariant. In the chiral limit, left- and right handed components of the

massless quark fields do not mix. This implies the chiral  $SU(3)_R = \times SU(3)_L$  symmetry of the QCD, what implies sixteen conserved Noether currents,

$$J_{R,a}^\mu = \bar{\psi}_R \gamma^\mu \frac{\lambda_a}{2} \psi_R, \quad J_{L,a}^\mu = \bar{\psi}_L \gamma^\mu \frac{\lambda_a}{2} \psi_L \quad (2.6)$$

with  $\partial_\mu J_{R,a}^\mu$  and  $\partial_\mu J_{L,a}^\mu$  both equal to zero.

It is possible to rewrite these currents in the form of the vector,

$$V_a^\mu = J_{R,a}^\mu + J_{L,a}^\mu, \quad (2.7)$$

and the axial current

$$A_a^\mu = J_{R,a}^\mu - J_{L,a}^\mu. \quad (2.8)$$

The charges corresponding to the vector and axial currents are:

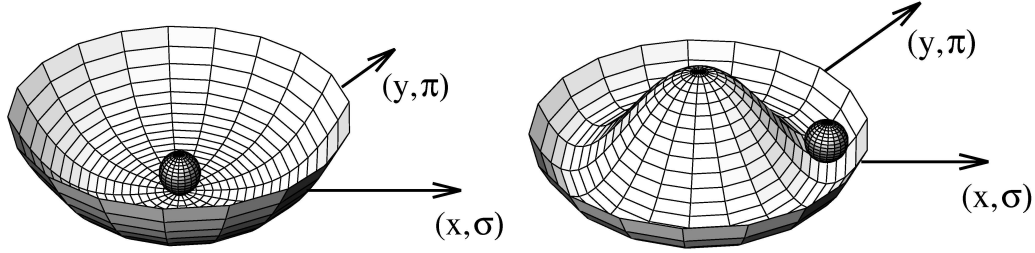
$$Q_a^V = \int d^3x \psi^\dagger(x) \frac{\lambda_a}{2} \psi(x), \quad Q_a^A = \int d^3x \psi^\dagger(x) \gamma_5 \frac{\lambda_a}{2} \psi(x). \quad (2.9)$$

### 2.1.1 Broken Symmetry

Chiral symmetry is spontaneously broken in nature. The ground state of QCD, i.e. the vacuum, is symmetric only under the subgroup  $SU(3)_v$  generated by the vector charges; the so called isospin symmetry. If the ground state would be symmetric, vector and axial charge operator would annihilate in the vacuum:  $Q_a^V|0\rangle = Q_a^A|0\rangle = 0$ . This would imply the appearance of parity doublets in the hadron spectrum [Wei05]. However, hadron states of different parities have significantly different masses. For example the vector meson  $\rho$ , with mass,  $m(\rho) = 0.77$  GeV and parity  $J^\pi = 1^-$  has a substantially lower mass than  $a_1$  with  $m(a_1) = 1.26$  GeV and parity  $J^\pi = 1^+$ .

Spontaneously broken chiral symmetry implies the existence of massless Goldstone bosons. With  $Q_a^V|0\rangle \neq 0$ , there must exist a physical state generated by the axial charge and energetically degenerated with the vacuum  $|\phi_a\rangle = Q_a^V|0\rangle$ . Choosing  $H_0$  as the QCD Hamiltonian which commutes with the axial charge, and assuming the energy of the ground state equal to 0, we have  $H_0|\phi_a\rangle = Q_a^V|0\rangle = 0$ . In the case of  $N_f = 2$ ,  $|\phi_a\rangle$  represents three massless pseudo-scalar bosons. Which can be identified with the pion isotriplet. Going to  $N_f = 3$ , the Goldstone bosons are identified with the members of the light pseudo-scalar octet; pions, kaons and the  $\eta$  meson.

The fact that the current quark masses are small but not zero, implies that  $H_0|\phi_a\rangle = Q_a^V|0\rangle = 0$  is not true anymore. Consequently, the Goldstone



(a) Lagrangian and ground state exhibit rotational symmetry.

(b) Now, even though the Lagrangian is still symmetric, the ground state is not itself rotational invariant.

**Figure 2.2:** The *Mexican Hat* potential, a mechanical example of spontaneous symmetry breakdown.

bosons, identified as the light pseudo-scalar meson octet, do have a finite mass.

A nice way to illustrate a symmetric potential where the ground state is not symmetric is with the mechanical analogy of the figure 2.2 [Koc95].

In (a), the minimum of the potential is just in the centre; and potential and ground state are invariant under rotations. In (b), the potential is rotational invariant, but the minimum lies in a ring at a certain distance from the centre. The central point is a maximum in this case and, therefore, a point of unstable equilibrium. A ball put in the centre will certainly fall down to the ring of minimum potential, thus breaking the symmetry of the system. In this example, even though the symmetry has been broken, the system still maintains its inherent rotational symmetry. Rotational excitations will not cost any energy whereas radial excitations do. In this simple model, rotational excitations could be identified with the Goldstone bosons.

## 2.2 In-Medium Effects

Since the decade of the 1990 the behaviour and characteristics of vector mesons in dense media have been a very debated issue.

This was initiated by the results published by the CERES and DLS collaborations which showed an enhancement of the dielectron yield over the known sources in the region below the mass of the  $\rho$  meson. An overview of experimental results about in-medium modifications will be given in the chapter 3.

In order to address these results, several theoretical model have been released.

They evaluate basically two possibilities to explain the mentioned dielectron enhancement.

In very high energy collisions (CERES at CERN SPS), the quark and gluon degrees of freedom may be released from their hadronic confinement. In this scenario, the annihilation of quark/anti-quark pairs,  $q\bar{q} \rightarrow l\bar{l}$ , may account for the enhancement in the  $e^+e^-$  pair spectrum.

At lower energies, in the energy regime of DLS and HADES, the dielectron enhancement was predicted to be related to the modification of the properties of vector mesons in dense media.

This modifications can be achieved by the partial restoration of chiral symmetry. However, there are also calculations based on the chiral symmetry restoration scenario which predict a rising of the  $\rho$  mass [Pis95]. They argue that in the symmetry restored environment the  $\rho$  meson becomes degenerate with its chiral partner, the  $a_1$  meson, and hence its mass should increase.

Modifications of vector mesons have been also successfully reproduced using only hadronic degrees of freedom [Pet98], without requiring any restoration of symmetry.

### 2.2.1 Chiral Symmetry Restoration

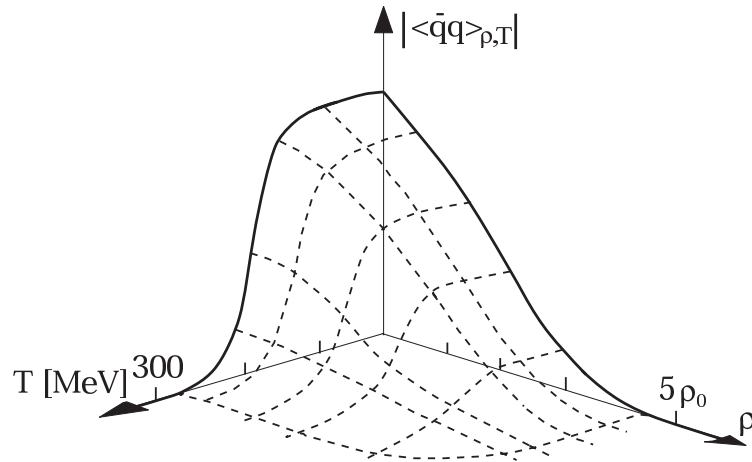


**Figure 2.3:** The quark condensate value as a function of the nuclear matter temperature (T) and the density ( $\rho$ ) according to the Nambu-Jona-Lasinio (NJL)[Nam61] model, from [Kli90, Wei93].

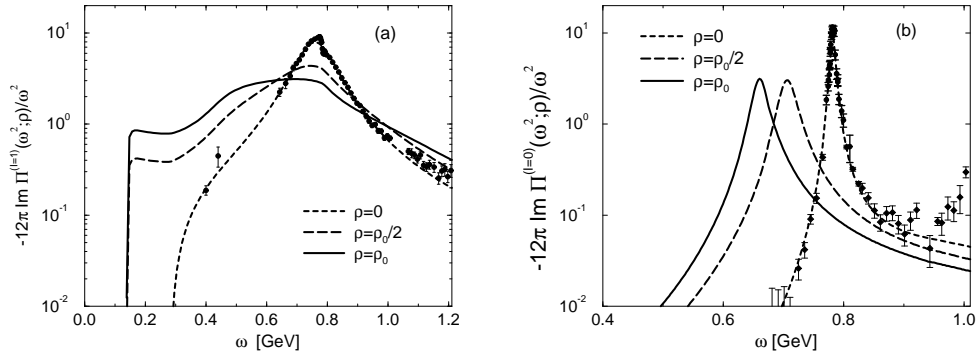


**Figure 2.4:** Calculated spectra of current-current correlation functions. The dashed lines show the vacuum spectra in the  $\rho$  and  $\omega$  channels normalised such that they can be compared directly with the corresponding  $e^+e^- \rightarrow$  hadrons data. The long dashed and solid lines show the spectral functions in nuclear matter at densities  $\rho_0/2$  and  $\rho_0 = 0.17 = fm^{-3}$  (figures from [Kli98]).

In the limit of zero temperature and low density, the quark-antiquark condensate can be calculated as [Dru90, Coh92, Lut92]:

$$m\langle\bar{\psi}\psi\rangle_\rho = m\langle\bar{\psi}\psi\rangle_0 + \sigma_{\pi N}\rho, \quad (2.10)$$

where  $\rho$  is the density and  $\sigma_{\pi N}$  is the pion-nucleon sigma term [Koc95]. This leads to a value of the chiral condensate as a function of density as:

$$\frac{\langle\bar{\psi}\psi\rangle_\rho}{\langle\bar{\psi}\psi\rangle_0} = 1 - \frac{\sigma_{\pi N}}{f_\pi^2 m_\pi^2} \rho \quad (2.11)$$

with  $f_\pi$  being the pion decay constant.

Equation 2.11 results in a reduction of the expectation value of the quark condensate of around 30 % already at normal nuclear density ( $\rho_0 = 0.17 FM^{-3}$ ), and it would lead to chiral symmetry being fully restored at densities around three times  $\rho_0$ . This is, however, beyond the boundaries of the low temperature and low density limit. Hence, such an extrapolation is not valid.

Model dependent calculations have been performed to obtain the value of  $\langle\bar{q}q\rangle$  as a function of density and temperature.

The figure 2.3 shows the result obtained from a calculation [Kli90, Wei93] based on the Nambu-Jona-Lasinio model [Nam61]. This calculation predicts

chiral symmetry restoration at temperatures of the order of  $T \sim 300\text{MeV}$  at 0 density or densities of  $\rho \sim 5\rho_0$  at low temperature. At densities on the order of  $\rho \sim 3\rho_0$ , it shows already an important decrease of the value of the  $\langle \bar{q}q \rangle$  condensate. This would imply that partial restoration of chiral symmetry may be achieved at low energy collisions as those produced at the SIS synchrotron at GSI.

It has been predicted that, in the conditions achieved in heavy ion collisions at the SIS at GSI, the properties of hadrons are modified. Most hadron masses, except  $\pi$ 's due to its Goldstone boson nature [Lut92], are expected to drop when embedded in nuclear matter.

Brown and Rho [Bro91] proposed a simple scaling law to calculate the mass of vector mesons at finite density:

$$\frac{m_v^*(\rho)}{m_v} \simeq \Phi(\rho) \equiv \frac{f_\pi^*(\rho)}{f_\pi}. \quad (2.12)$$

I.e. the mass of vector mesons should drop proportionally to the change of the pion decay rate ( $f_\pi$ ) with density.

Modern calculations based on effective Lagrangians predict a strong modification of the spectral functions of vector mesons as a function of the density [Kli96, Kli98]. The spectral functions of  $\rho$ ,  $\omega$  (see fig. 2.4) and  $\phi$  would be widened and their maxima shifted to lower masses.

## 2.2.2 Hadronic Scenario

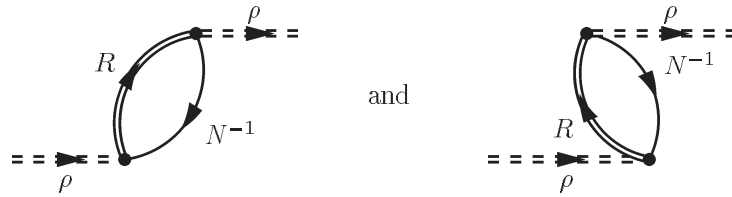


**Figure 2.5:** Resonance-hole self-energy diagrams for the rho meson. The double dashed line stands for a physical rho meson that contains the  $\pi\pi$ -width [Pet98].

Calculations based on pure hadronic scenarios also lead to modifications of the  $\rho$  spectral function [Leu98].

Modification of the pions in nuclear medium [Cha92, Her92, Cha96] as well as

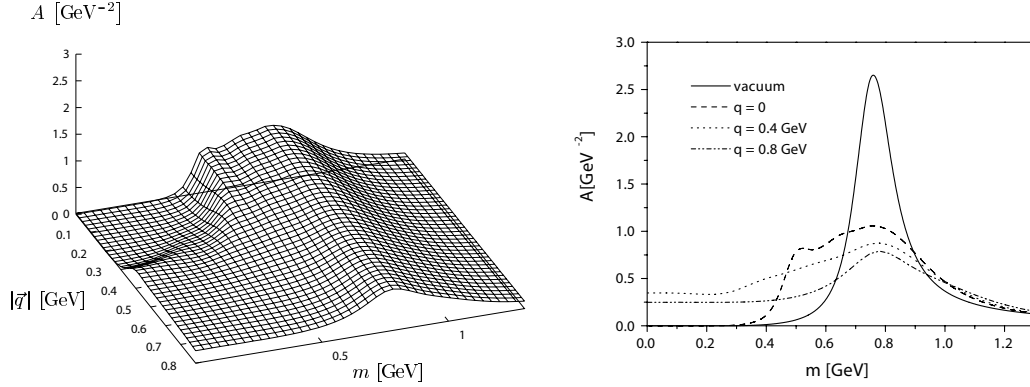


**Figure 2.6:** Self-consistent spectral function of the rho meson for  $\rho_N = \rho_o$ . On the right: Cuts through the spectral function for different three-momenta together with the vacuum spectral function [Pet98].

collisions of the vector mesons with nucleons of the Fermi sea [Fri97, Rap97, Pet98] lead to a broadening of the rho spectral function in medium. In all these references, the  $\rho$  spectral function becomes much broader in medium without any substantial change of its pole position [Leu98]. Precisely, W. Peters and collaborators [Pet98] propose a modification of the  $\rho$  spectral function due to its coupling to resonance-hole states in the dense medium. This implies that the transverse channel of the vector meson is completely washed out in matter and can no longer be seen as a resonance of the vacuum. The statistically averaged spectral function ( $A = \frac{1}{3}(2A^T + A^L)$ ) from this calculation is shown on the figure 2.6. There we can see how, in contrast to what was shown on the figure 2.4 [Kli98], the shape of the  $\rho$  spectral function is not shifted at all but only strongly widens.

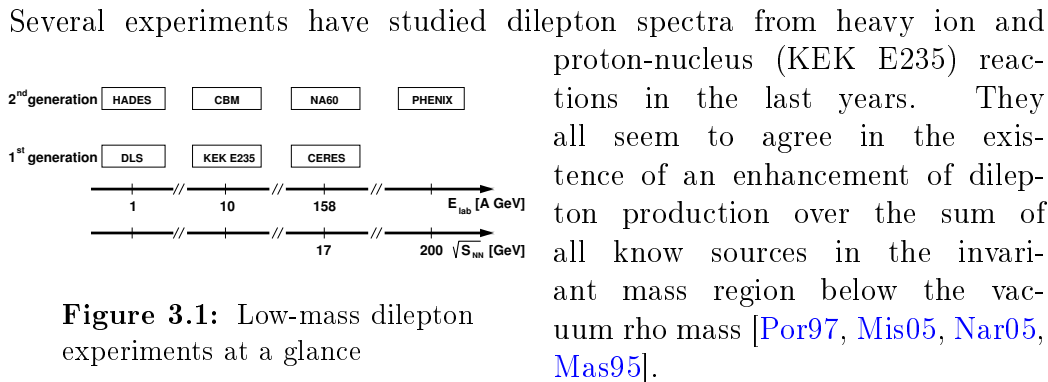


# Chapter 3

## Probing In-Medium Effects

### 3.1 Dilepton Spectroscopy

For the study of the in-medium modification of vector mesons, their decays to dilepton pairs, either  $e^+e^-$  or  $\mu^+\mu^-$ , are ideal probes because they do not interact strongly with the surroundings, hence they leave practically undistorted the medium.



A sketch showing the main experiments focused on the study of low-mass dilepton production can be seen in the figure 3.1. The first generation; DLS at BEVALAC [Por97] in the energy range of  $\sim 1$  AGeV, E325 at KEK [Nar05] and CERES [Mis05] at the CERN-SPS did already complete their measurements and have published their results.

Parallel to the  $e^+e^-$  channel, the dimuon spectrum up to the  $J/\Psi$  region has been measured by the HELIOS-3 [Mas95] and the NA38/NA50 [Abr96b, Abr96a] collaborations at the CERN SPS. Experiments with dimuons are

very successfully being carried on by the NA60 collaboration at CERN-SPS [Arn06] (figure 3.5).

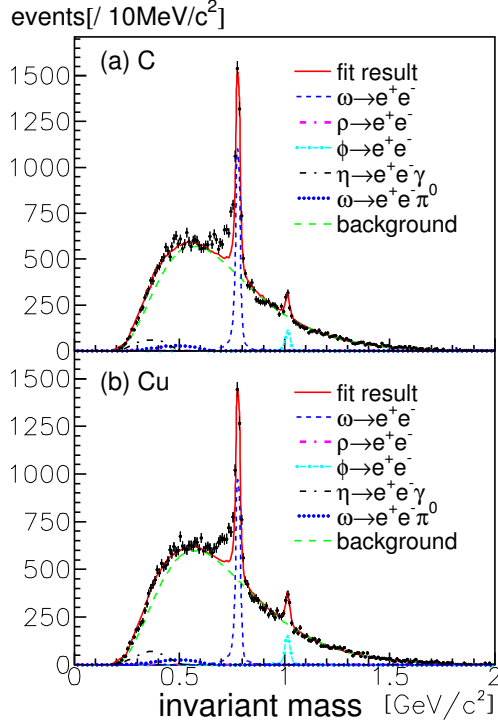


**Figure 3.2:** Dielectron invariant mass spectra from the KEK-PS E325 experiment obtained with a Carbon target (up) and a Cooper target (down). In red sum of all known sources and green, estimated combinatorial background. An enhancement  $e^+e^-$  pairs below the  $\omega$  meson mass is apparent, as well as the *dissolving* of the  $\rho$  meson [Nar05].

carbon targets, are in clear agreement with the disappearance of the  $\rho$  resonance [Nar05].

Even though the mentioned models allow a good description of the dilepton spectra in ultrarelativistic heavy ion collisions, the situation in the low energy regime is not so well understood. In the energy range of  $E_{beam} \sim 1 \text{ AGeV}$  only

An overview of the results obtained by E325, DLS, CERES and NA60 can be seen on the figures 3.2, 3.3, 3.4 and 3.5 respectively.

Several scenarios have been postulated to explain the excess of dilepton from the different experiments.

At high energies, possible transition to a deconfined phase may account for part of the enhancement [Sri96], but not for all of it [Cas95]. On the other hand, calculations based on the modification of the mass and width of vector mesons in a hot and dense hadronic environment can reproduce CERES data very accurately [Li95, Cas95].

There are indications that the  $\rho$ -resonance mass may drop down to  $M_\rho \sim 550 \text{ MeV}/c^2$  and its width may be broad so wide that it may lead to the resonance being *dissolved* in the background [Kli98, Pet98] (fig. 2.4). The spectra from the E325 experiment (fig. 3.2), produced in reactions of 12 GeV proton beams colliding against fixed copper and carbon targets, are in clear agreement with the disappearance of the  $\rho$  resonance [Nar05].

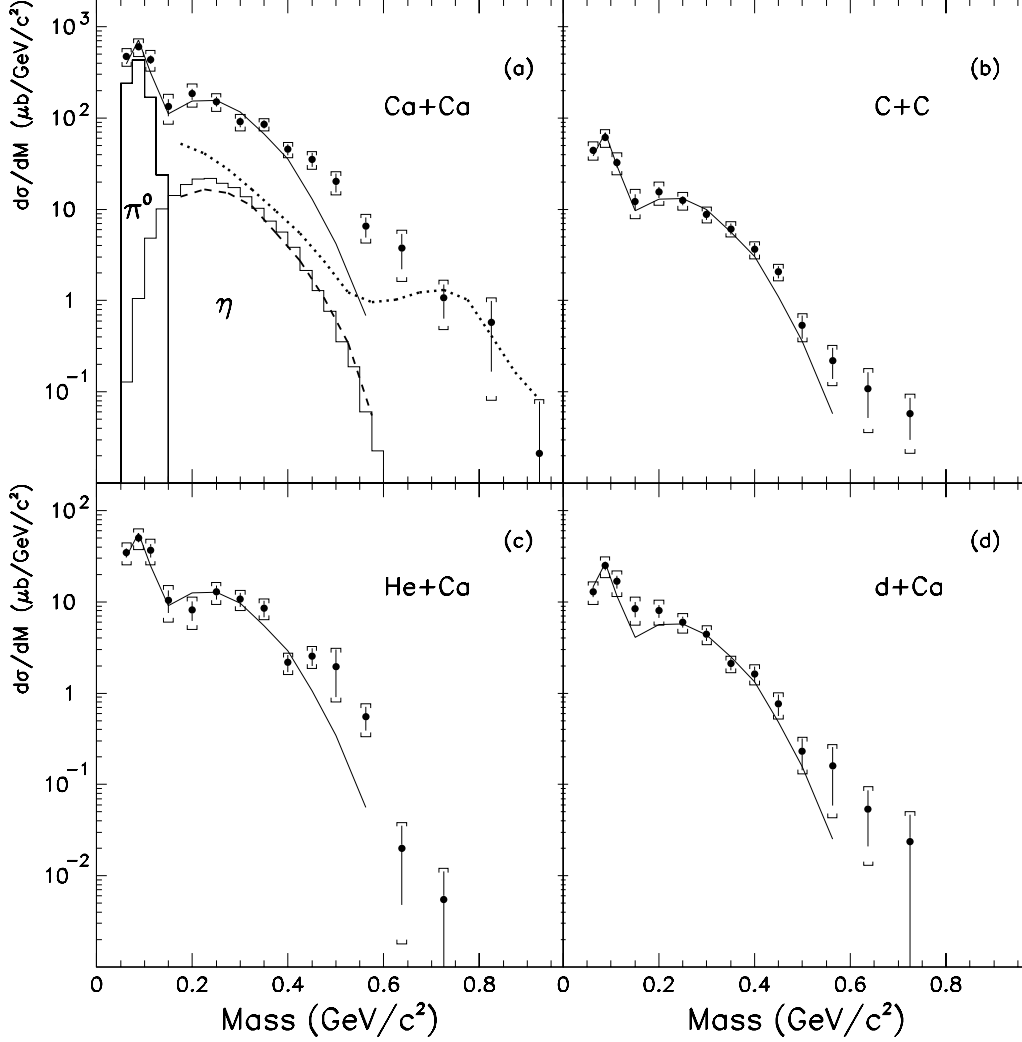


**Figure 3.3:** DLS measurements of the dielectron cross sections from (a) Ca+Ca, (b) C+C, (c) He+Ca and (d) d+Ca reactions. Panel (a) also contains the calculated signal from BUU simulations and histograms showing the  $\pi^0$  and  $\eta$  decay contributions as estimated from TAPS measurements and an isotropic thermal model. The dashed line represents the  $\eta$  component of the BUU calculations. The solid lines in the four panels show fits to the low-mass data using  $\pi^0$  and  $\eta$  decay estimate with adjustable normalisations [Por97].

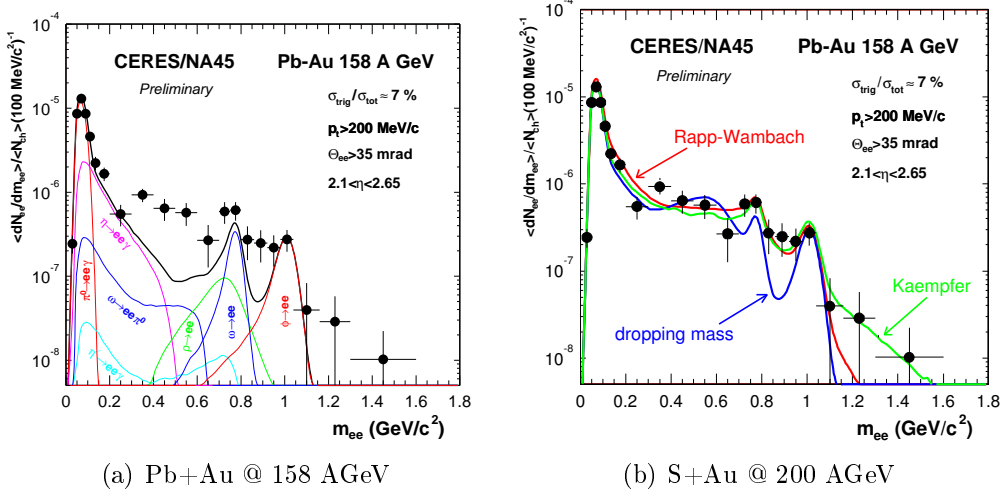


**Figure 3.4:** Dielectron mass spectrum with the hadron decay cocktail (left) and with the models (right). The spectrum contains  $2571 \pm 224$   $e^+e^-$  pairs with  $M_{inv} > 0.2$   $\text{GeV}/c^2$ , with the signal to background ratio of 1:21. The multiplicity of charged particles, averaged over event centralities and over the acceptance, is  $\langle dN_{ch}/d\eta \rangle = 335$  [Mis05].

data from the DLS experiment are available [Por97] (fig. 3.3). These data show an enhancement in the dilepton spectrum over the estimations from elementary reactions which led to several controversial theoretical interpretations in the last years. Early calculations [Bra98a, Bra99], which were able to accurately describe CERES data, failed to describe DLS data. Only more modern calculations [She03, Fuc04], which include in-medium modifications of vector mesons as well as decoherent dilepton emission from heavy ions reactions through vector mesons, have succeeded in reproducing the experimental spectra. Moreover, the  $\eta$  and  $\pi^0$  production rates obtained by DLS disagree greatly with the results obtained from the TAPS collaboration [Ave97]. A discrepancy that can not be explained by the final-state interaction of the measured hadronic channel [Bra98a].

Experimentally, DLS had several limitations. A very poor mass resolution, of about 12 %, and a small geometrical acceptance (0.5–1.0 %). The poor mass resolutions makes impossible to distinguish among all the individual sources contributing to the  $e^+e^-$  spectrum. The small geometrical acceptance featured led to a limited amount of recorded statistics. Also, the transverse momentum of the single leptons is limited by the acceptance. This had consequences on the mass spectrum below  $0.2 \text{ GeV}/c^2$  as well as on the whole

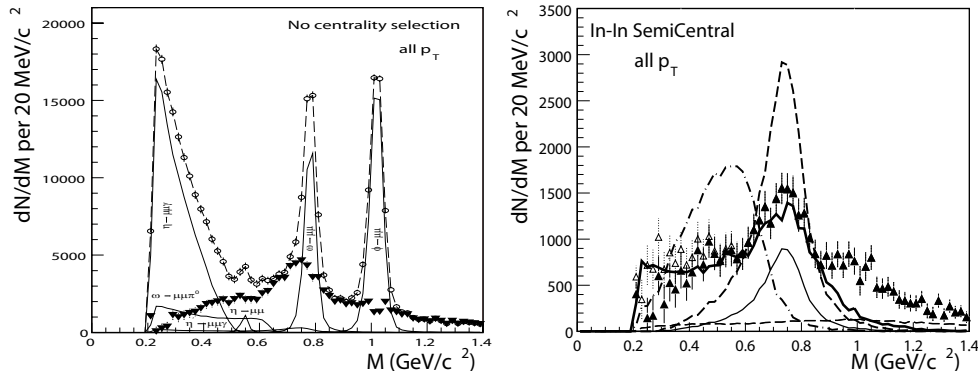


**Figure 3.5:** Experimental dimuon spectrum (open circles) from In-In collisions at 158 AGeV recorded by the NA60 [Arn06] experiment. The triangles show the excess of dimuon yield over the hadronic decay cocktail. On the right, comparison of the excess spectrum with various theoretical predictions for the  $\rho$  meson in-medium. free  $\rho$ , solid thin line. The thick solid line depict in-medium broadening [Cha96, Rap00] models and the dotted-dashed line models predicting broadening plus shifting [Bro91] of the  $\rho$  mass (event though the actual calculation of this curve is arguable, see recent letters of Brown and Rho in [Bro05]).

range of the rapidity and transverse momentum spectra. New measurements are needed in order to clarify this controversy around the dielectron production in heavy ion reactions in the energy regime between 1–2 AGeV/c<sup>2</sup>.

### Recent results

A second generation of experiments has been built to continue with the research of the in-medium modifications of vector mesons. They have the aim to reproduce the already mentioned results with better resolution and more statistics.

Nowadays there are two experiments dedicated to dilepton spectroscopy running. The first one is HADES at the GSI SIS ( $E_{lab} \sim 1\text{AGeV}$ ), which runs in an energy regime comparable with that of DLS. The second is the NA60 experiment, at the CERN SPS ( $E_{lab} \sim 158\text{AGeV}$ ).

NA60 is taking data on di-muon in an energy regime similar to what CERES has measured. An overview of the latest NA60 spectra from In-In collisions at 158 AGeV is shown in the figure 3.5. The left panel shows the inclusive  $\mu^+\mu^-$  invariant mass spectrum. All known individual sources (except  $\rho$ ) are

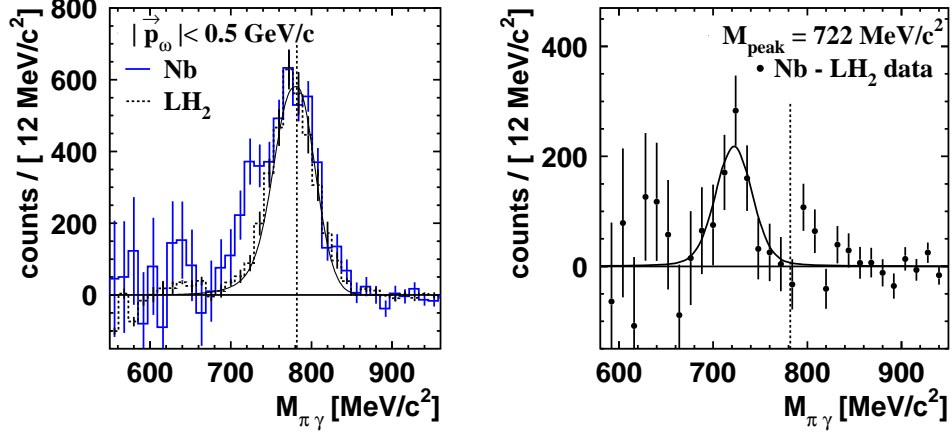


**Figure 3.6:** Left:  $\pi^0\gamma$  invariant mass spectrum for Nb data (solid histogram) and LH<sub>2</sub> data (dashed histogram) after background subtraction. Right: In-medium decays of the  $\omega$  meson. The vertical dashed line indicates the vacuum  $\omega$  mass [Trn05].

depicted with solid lines. The difference between the inclusive spectrum and the *cocktail* is shown on the right panel. Here it looks that the excess of  $\mu^+\mu^-$  pairs could be attributed to the  $\rho$  meson. Which under this conditions would have a mass centred at its nominal vacuum value whereas its width largely broadened [Arn06].

Complementary to the presented dilepton spectra, the TAPS collaborations has recently published data on the photoproduction of  $\omega$  in Nb and LH<sub>2</sub> targets [Trn05]. The reaction they analyzed was:

$$\gamma + A \rightarrow \omega + X \rightarrow \pi^0\gamma + X',$$

where the final state contains a  $\pi^0$  that may undergo strong final state interaction with the surrounding medium.

The left panel of figure 3.6 shows the  $\pi^0\gamma$  invariant mass after background subtraction for the Nb target (solid blue) and the LH<sub>2</sub> target (black dotted). The excess of omega yield in  $\gamma$ Nb over  $\gamma$ LH<sub>2</sub> is shown on the right panel. This indicates a shifting of  $\omega$  to lower masses when embedded in a medium of finite density [Trn05].

After all that was here presented it looks clear that more data on the  $e^+e^-$  spectrum and in medium production of vector mesons are needed.

Specially, the comparison of the, somehow, contradictory latest results presented from CBELSA/TAP [Trn05] and NA60 [Arn06] (both seem to indicate the existence of strong in-medium modification but in different directions) justifies new experiments in this field.

In this scenario, the HADES experiment at GSI SIS has successfully measure dielectron spectra from C+C collisions at 1 and 2 AGeV.

## 3.2 HADES

It was already mentioned in this chapter that there is a need of accurate data on  $e^+e^-$  pair production from heavy ions collisions in the energy range from 1-2 AGeV.

The HADES experiment [HAD, HAD94] aims to measure dielectron spectra from pp,  $\pi$ A, pA and AA collisions, with energies for proton beams up to 4.7 GeV and for heavy ions up to 2.2 AGeV.

### In-medium effects

As a second generation experiment, HADES aims to reproduce the presented data with higher statistics and better mass resolution.

To improve the statistics, HADES features a large geometrical acceptance ( $2\pi$  in azimuthal direction and from  $18^\circ$  to  $85^\circ$  degrees in polar direction) and a dedicated dilepton trigger (permits an enhancement of the recorded dielectron sample in the order of a factor 10–15).

The momentum resolution reached during the C+C at 2.2AGeV beamtime was in the order of  $\Delta P/P \sim 2.5\%$ . This may help to obtain a cleaner spectra and to be able to resolve the signals from the decays of the  $\rho$  and  $\omega$  resonances.

meson	mass (MeV/c <sup>2</sup> )	FWHM (MeV/c <sup>2</sup> )	$c\tau$ (fm)	main decay	$e^+e^-$ branching ratio
$\rho$	776	150	1.3	$\pi\pi$	$4.7 \times 10^{-5}$
$\omega$	782	8.49	23.4	$\pi^+\pi^-\pi^0$	$7.1 \times 10^{-5}$
$\phi$	1019	4.26	44.4	$K^+K^-$	$3.0 \times 10^{-4}$

**Table 3.1:** Main characteristics of vector mesons [Eid04].

**pp program**

In January 2004, HADES has measured its first production proton–proton run. The reaction measured, protons of 2.2 GeV kinetic energy on a LH<sub>2</sub> target, was chosen to study the productions of the  $\eta$  - and  $\pi^0$ –mesons.

With the perspective of the heavy ion  $e^+e^-$  spectrum, it is necessary to have a good understanding of the elementary sources of dilepton production in the low invariant mass region. Below 400 MeV/ $cc^2$  it is known that  $\pi^0$  and  $\eta$  are the main contributors to the spectrum (see published CERES [Mis05] and DLS [Por97] spectra, figures 3.4 and 3.3). Deep understanding of the elementary cross sections are of great theoretical interest, as they are the input for transport model calculations used to describe heavy ion spectra [Shy03].

Besides the baseline studies to compare with heavy ions experiments, the analysis of the  $\eta$  production is one of the major topics of the HADES p+p program.

In the vicinity of the production threshold, the inclusive  $\eta$  cross sections are well known, but at higher energies the existing data have large errors which could be significantly reduced.

The exclusive reconstruction of the  $\eta$  decays is an optimal tool to study the  $\eta$  Dalitz decay, where the existing data [Lan85] is rather poor and is based on a sample of 80 counts.

In this context, this thesis will be dedicated partially to the analysis of the first HADES proton–proton run. More specifically, the results of the analysis of the  $\eta$  hadronic decays (chapter 8) along with an a description of the techniques used (chapter 7) will be presented.

## Part II

# The HADES Detector System



# Chapter 4

## The Spectrometer

The High Acceptance DiElectron Spectrometer (**HADES**) is a second generation high resolution dilepton spectrometer. It is installed in the *Heavy Ion Synchrotron*, SIS, at the GSI laboratory in Darmstadt, Germany. Its main objective is to accurately reconstruct the invariant mass of lepton pairs produced in the decay of light vector mesons. The design goals were to achieve a momentum resolution of  $\Delta p/p \sim 1\%$  at reaction rates in the order of  $10^6$  Hz [HAD94].

### 4.1 Overview

The branching ratio of light vector mesons to electron-positron pairs is in the order of  $10^{-5}$  [Eid04]. HADES was designed with the goal of maximizing the  $e^+e^-$  recorded sample. This is achieved by two means: a large geometrical acceptance and high counting rates. The latter achieved by the combination of high intensity beams and a intelligent online trigger system.

#### Geometry

The spectrometer has a six-fold geometry with the beam line as the symmetry axis (figures 4.1 and 4.2). It covers almost the full azimuthal direction ( $\phi$ ), except for the place where the six coils of the magnet are located. In the polar direction,  $\theta$ , the detection area covers from  $18^\circ$  to  $85^\circ$  degrees. As a fixed target experiment, where the resultant particles are *boosted* in forward direction, HADES's acceptance covers an important fraction of the available phase space for detecting  $e^+e^-$  pairs from light vector mesons (in the order of 40% [Sán03]). For elementary reactions, the hole at small polar angles leads

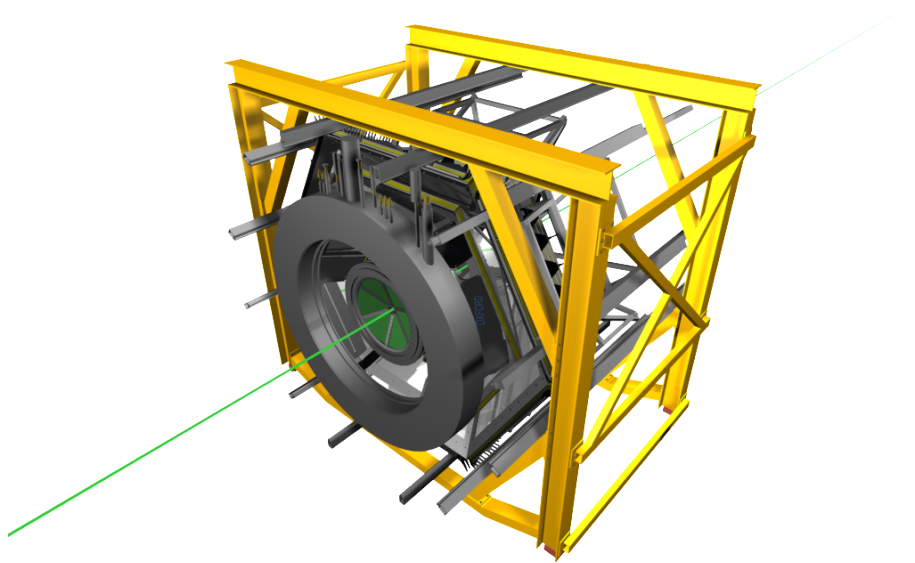


**Figure 4.1:** View of the HADES spectrometer at GSI. The beam (green line) enters the set up at a height of 2.5 m [Sch06].

to an important loss in the probability to reconstruct exclusively reactions, i.e. to detect all the outgoing charged particles of a reaction.

### High Intensity

The goal of HADES is to operate at beam intensities of up to  $10^8$  particles per second. A 1% interaction length target produces  $10^6$  minimum bias events per second, or about  $10^5$  central events. To cope with that figures, the data acquisition system needs fast electronics to transport, process and store a large amount of data. HADES's raw data production is in the order of 8 Giga-Bytes per second [Tra00].

### The Trigger System

The trigger system has the task to select events containing electron or positron traces in real time, thus enhancing the leptonic content of the data [HAD94, Leh99]. As the amount of data that can be written to the mass storage system is limited, the trigger system can enhance the fraction of electron-positron pairs per stored event. Its goal is to achieve an  $e^+e^-$  enhancement of the order 100 in Au+Au reactions [Leh99, Tra00].

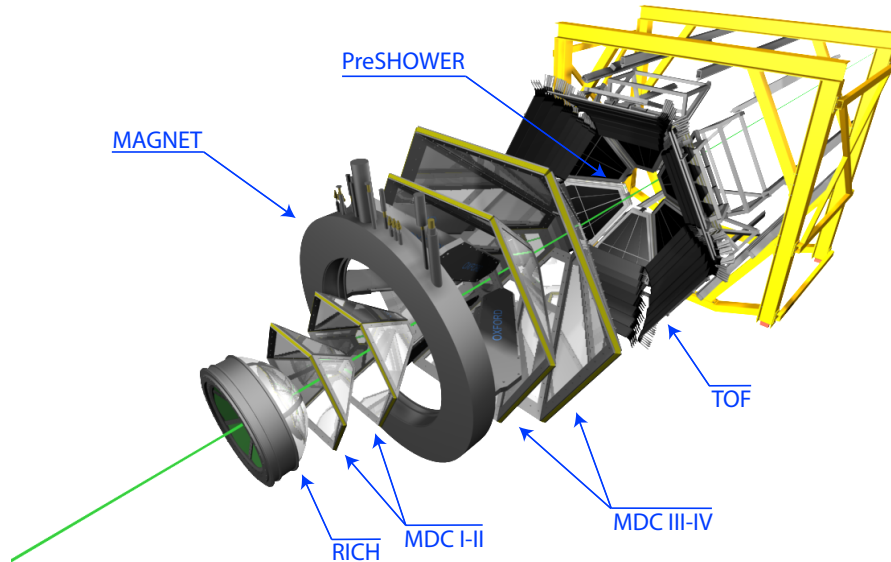


Figure 4.2: Extended view of HADES with all its subdetectors [Sch06].

## 4.2 The Single Detectors

HADES is a complex spectrometer made of a combination of several components. They can be divided into two groups:

### High Resolution Tracking

24 State-of-the-art Mini Drift Chambers, **MDC**, combined with a superconducting toroidal magnet.

### Particle Identification

The **R**ing **I**mage **C**herenkov detector, **RICH**, the **time of flight wall** and the **Pre-Shower** detector provide information to identify electrons and positrons.

Besides these main detectors, HADES has also several kinds of targets for the different experimental runs plus the START/VETO detector system which has the task to set the *time zero* of the heavy ion reactions.

### 4.2.1 The Targets

Up to now HADES has had production runs with different particle species, p+p, C+C and Ar+KCl. For the Carbon runs, the target was just a combination of one or more thin foils of pure carbon (graphite). More precisely, in

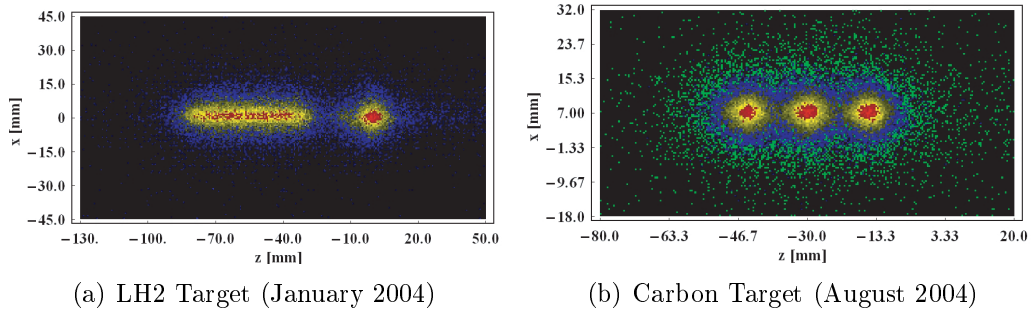


**Figure 4.3:** Reconstruction of two different targets.

the November 2001 run, C+C at 1–2 AGeV, the target was made of only one foil of 8 mm diameter and thickness of 5 mm with a density of  $2.15 \text{ g/cm}^3$  (5% interaction length). During the November 2002 run, the target was a combination of two Carbon foils, 3 mm thick each, separated 2 cm from each other ( $\pm 1 \text{ cm}$  from the nominal target position). The density of the foils was  $2.15 \text{ g/cm}^3$  and had a diameter of 3 mm.

### The Liquid Hydrogen Target

A liquid hydrogen target has been developed to fulfil the requirements of the study of the elementary processes through collisions of light projectiles;  $\pi$ , protons or deuterons, against a proton target.

The liquid hydrogen target consists of a cell 5 cm long and 2.5 cm in diameter (fig. 4.4) filled with liquid hydrogen at atmospheric pressure and a temperature of 20 K.

The cylindrical vessel containing the hydrogen is made up of  $100 \mu\text{m}$  Mylar foils glued together with Ecobond<sup>®</sup> 286 glue. The thermal isolation of the target cell is ensured by 10 layers of  $6 \mu\text{m}$  thick aluminized Mylar.

Thanks to the use of low Z material the interaction probability of the beam with the housing material is less than  $7 \cdot 10^{-4}$ , whereas the 5 cm long liquid



**Figure 4.4:** Photograph of the LH2 target cell.

hydrogen target itself yields a 1% interaction probability.

### 4.2.2 The START and VETO detectors

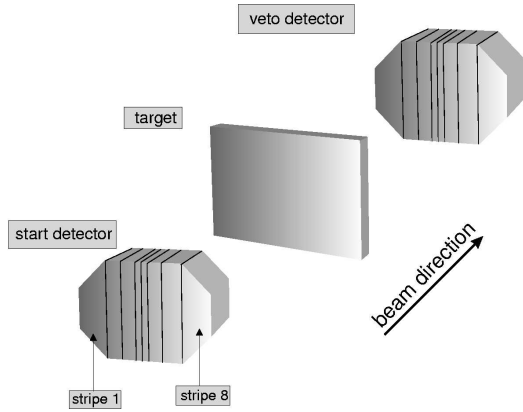


**Figure 4.5:** The start and veto

The START and VETO detectors are two CVD (chemical vapour deposition) diamond detectors of octagonal shape and an outer dimension of 25x15 mm (fig. 4.5).

Their task is to determine when a reaction occurred, to provide the start time and to monitor the beam quality. The HADES's START/VETO detectors can cope with primary particle rates up to  $10^8$  particles/second and it provides a time resolution of 30 ps.

The detectors are located at a distance of 75 cm before (START) and

after (VETO) the target (Fig. 4.5). The diamond layer has a thickness of 100  $\mu\text{m}$  and is segmented into eight strip of variable width (1.55–5.4 mm). They are thinner in the middle in order to keep the counting rates constant in all the strips [Ber99].

The START and VETO detectors work in anticoincidence mode, i.e. if there is a coincident detection on one of the START strips with three VETO strips the reaction will not be triggered. A coincident detection in START and VETO means that very likely no reaction took place inside the target. This algorithm yields an efficiency of 96.5% [Ber99] to detect a reaction in a heavy ion collision. For the proton-proton reaction, the figures are not so favourable. And hence the START/VETO detectors were not used during the proton-proton runs of January 2004 and May 2006.

### 4.2.3 Ring Image Cherenkov Detector

In modern nuclear physics experiments, due to the high energies, most of the particles travel at speeds next to the velocity of light in vacuum. Under certain conditions it may happened that these particles travel faster than the light in a medium,  $v_{part} \geq c/n$ , leading to the radiation of photons [Che37].

This effect, known after its discoverer P.A. Cherenkov, is the operation principle for the *Ring Image Cherenkov Detector*, or *RICH*.

The HADES' RICH is a Cherenkov detector designed to separate electrons and positrons from hadrons at SIS energies.

As the inner most detector, there are strong constraints upon the size of the detector. A small increase in diameter of the RICH would lead to a cubic increment of the volume of the outer detectors with the consequent increase in price. Hence the radiation volume has to be kept small, what implies a very few amount of photons radiated per electron. A strong effort has been made to minimise the loss of photons during their focusing towards the detection area.

The radiator used is  $C_4F_{10}$ , which has an index of refraction of  $n = 1.0015$ . This leads to a gamma threshold of  $\gamma_{th} = 18.2$  [Che37] (eq. 4.1).

$$\gamma \geq \sqrt{\frac{n^2}{n^2 - 1}} \quad (4.1)$$

From these figures, the minimum energy to produce light for the different species produced is:

- $E_{th}^p \simeq 15.9$  GeV
- $E_{th}^\pi \simeq 2.4$  GeV
- $E_{th}^e \simeq 8.5$  MeV.

At the energies available at the GSI SIS (1-2 AGeV in heavy ions and 4 GeV proton beams), most of the electrons produced will have energies over the Cherenkov threshold, while only some pions and, very unlikely, any proton will produce any radiation. It is important to notice as well that with momenta  $P > 100$  MeV/ $c$ , the emission angle of the photons (from electrons) reaches its asymptotic limit of  $\Theta_c = 3.18^\circ$  (eq. 4.2) [Che37]

$$\cos \Theta_c = \frac{1}{n\beta}. \quad (4.2)$$

As it can be seen in figure 4.6, the geometry of the detector has been set such that the light cone will be reflected in the front mirror producing rings of almost constant diameter on the detection plane.

The mirror is made of carbon of a thickness of 1% interaction length coated with a reflective layer of aluminium [Fab03a]. It features an overall reflectivity larger than 85% in the VUV region. The mirror has a spherical shape with a curvature radius of  $R = 870$  mm and it is 145 cm wide (fig. 4.6). The target is located at 402 mm, i.e.  $0.45 \cdot R$ , from the centre of the mirror. Thus the path length of the electrons through the radiator varies from 36 cm at

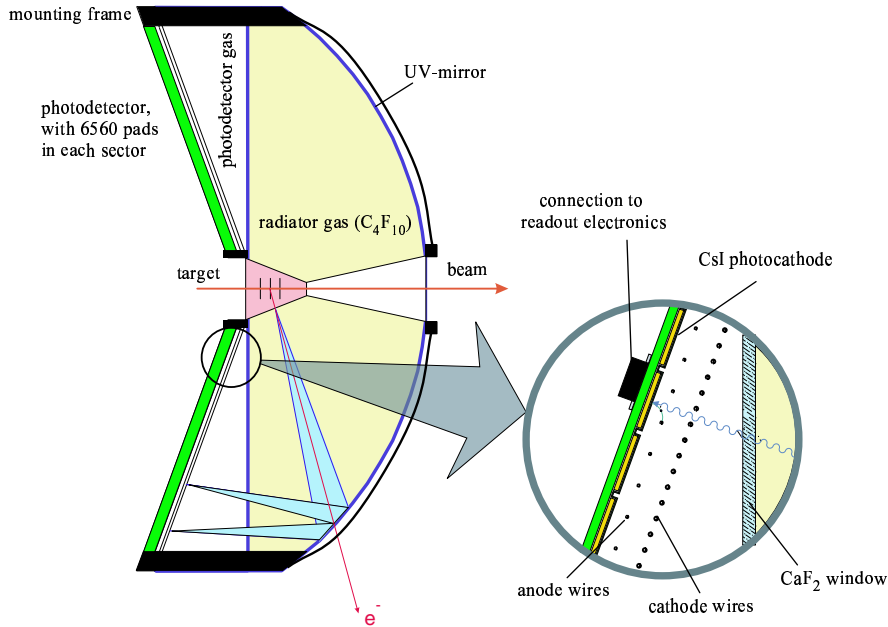


Figure 4.6: The RICH detector

forward angles to 65 cm in perpendicular direction. Due to this fact, the efficiency is not constant in all polar angles and there is a different average number of photons emitted per electron depending upon the polar direction. To separate the radiation volume from the detection gas, a window of 5 mm thick  $CaF_4$  is used.  $CaF_4$  features good transparency for VUV light with an average transmission of 70%.

The detector's gas is  $CH_4$ . It has been specially chosen for its good ultraviolet transparency.

The detection of photons is performed by photo-sensitive *multi-wire proportional chambers*, MWPC, with a cathodic pad plane. The pad plane is coated with a layer of CsI [Fri99].

The photocathode plane is mounted with an inclination of  $20^\circ$  respect to the plane perpendicular to the beam (fig. 4.6). In this way, it is possible to have the detection matrix quasi in the focal surface of the mirror. Due to the fact that the pad plane is only approximately on the focal plane, the size of the ring images are not constant. In order to get rings of constant radius ( $R_{ring} = 4pad$ ), the size of the pads varies from 7.1 mm x 6.6 mm to 4.6 mm x 6.6 mm [Fab03a].

The number of photons radiated per path length of radiator material is given by [Lit73]

$$\frac{dN_\gamma}{dL} = 2\pi\alpha Z^2 \int_{\lambda_1}^{\lambda_2} \left[ 1 - \frac{1}{\beta^2 n^2} \right] \frac{d\lambda}{\lambda^2} \quad (4.3)$$

This leads to an average number of photons produced per electron of [Toi04]

$$N_{min,max} = N_0 \frac{L_{min,max}}{\gamma_{thr}^2} \quad (4.4)$$

where  $L_{min,max} = 0.36 - 0.65 \text{ m}$  is the distance travelled by the electrons in the radiator, and  $N_0$  is the so called figure of merit, related to the VUV behaviour of all the material in the detector.

$$N_0 = 2\pi\alpha\epsilon_{se} \int_{\lambda_1}^{\lambda_2} R_{mirror} T_{C_4F_{10}} T_{CaF_4} T_{CH_4} \epsilon_Q d\lambda \quad (4.5)$$

The latest experimental values show minimum values for the figure of merit from  $N_0^{exp} = 78$  to 98. Hence the average lies between 17 and 30 photons per ring [Fab03b, Fri03].

#### 4.2.4 The Tracking System

The HADES tracking system is composed of high resolution Mini Drift Chamber (MDC) detectors and a Superconducting magnet. The latter is in charge to provide the momentum dependent deflection necessary to reconstruct the original momentum of the particles.

##### The Super conduction Magnet

The HADES magnet is composed of six superconducting coils, in a toroidal geometry, surrounding the beam axis (Figure 4.7). It produces an approximately toroidal magnetic field (i.e deflection is in polar direction:  $\hat{r} \times \hat{\varphi} = \hat{\theta}$ ) with a maximum field of around 0.7 T [Bre99] in the detection region. This has been chosen to keep the field around the target and in the RICH region almost null (important for lepton identification) and the transverse momentum kick as  $P_T^{field} \leq 100 \text{ MeV}$  [HAD94].

##### Mini Drift Chambers

The MDC detector of HADES is formed out of 24 low-mass, trapezoidal, planar multi layer Mini Drift Chambers with a total active area of about  $30 \text{ m}^2$  [Mün04].

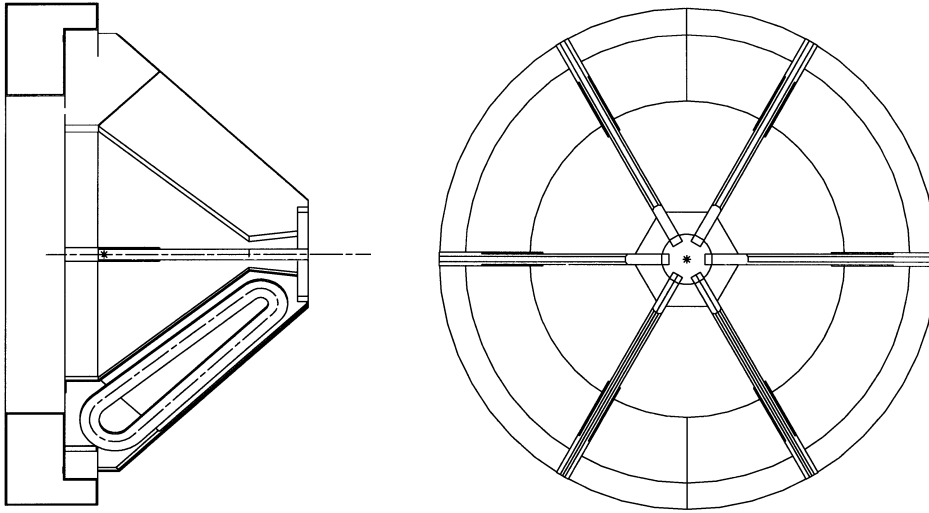


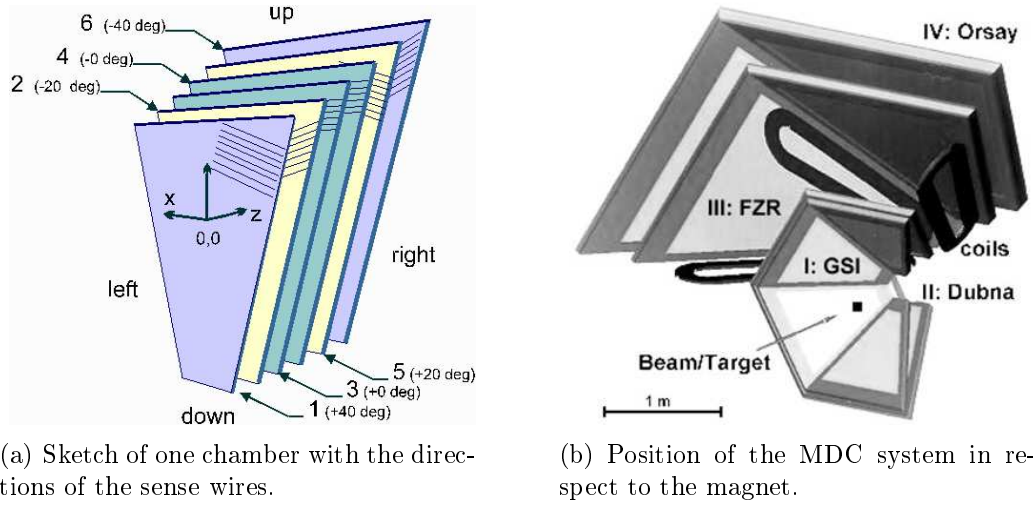
**Figure 4.7:** Vertical cut (left) and front view (right) of the superconducting toroid (schematically). 6 coils are mounted in individual vacuum chambers which are connected by a support ring upstream of the target. A hexagonal front plate compensates the magnetic forces between the coil cases.

They are placed symmetrically around the beam axis to cover the full azimuthal space and from  $18^\circ$  to  $85^\circ$  in the polar direction (figures 4.2 and 4.8).

The size of the chambers and the drift cells increase from plane I to IV. Plane areas vary from  $0.35 \text{ m}^2$  (plane I) to  $3.2 \text{ m}^2$  (plane IV), this way the solid angle covered by each plane stays constant. To keep the average cell occupancy constant, cell sizes vary from  $5 \times 5 \text{ mm}^2$ , in the inner most plane, to  $14 \times 14 \text{ mm}^2$  in the outer most plane or plane IV.

The 24 chambers are divided into six sectors following the symmetry given by the magnet. Each of the six sectors are formed by four planes (I–IV), two (I and II) before the magnet and two (III–IV) after, as it is shown in the figures 4.2 and 4.8. This way trajectories before and after the deflection of the particles in the magnetic field can be reconstructed providing the necessary information to reconstruct the original momentum.

To achieve a good momentum resolution, the tracking system needs to provide an accurate space resolution. For that purpose, thorough studies of the drift times inside the cells, as well as low mass elements to avoid multiple scattering of the particles, are essential. The low mass active area is achieved using a light gas mixture of helium and isobutane (quencher) in a ratio of 60:40 [Kan04], light cathode and field wires made of aluminium and entrance



(a) Sketch of one chamber with the directions of the sense wires.

(b) Position of the MDC system in respect to the magnet.

**Figure 4.8:** The MDC detector. The labels in (b) illustrate where each plane has been produced.

windows made of  $12 \mu\text{m}$  thick aluminized *mylar*. All in all, the total thickness of the detector in units of radiation length is kept below  $5 \cdot 10^{-4}$  [Mün04].

22 out of the 24 chamber are in place and operational since 2002. The last two chamber were installed in the spring of 2006 and were used by the first time during the beamtime of May 2006. The experimental average spatial resolution of the drift cells is between  $100$  and  $130 \mu\text{m}$  [Mün04]. Under clean testing conditions intrinsic spatial resolutions of  $70 \mu\text{m}$  have been achieved, consistent with the results obtained from simulations [Mar05].

### 4.2.5 The META

After the Tracking system, there is the so called *Multiplicity and Electron Trigger Array*, **META**, the outer most detector system. As parts of the META system we have the time of flight wall and the Pre-Shower detector. Their main task is to provide a fast determination of the event multiplicity for the LVL1 trigger and fast tracking and lepton identification for the LVL2 trigger.

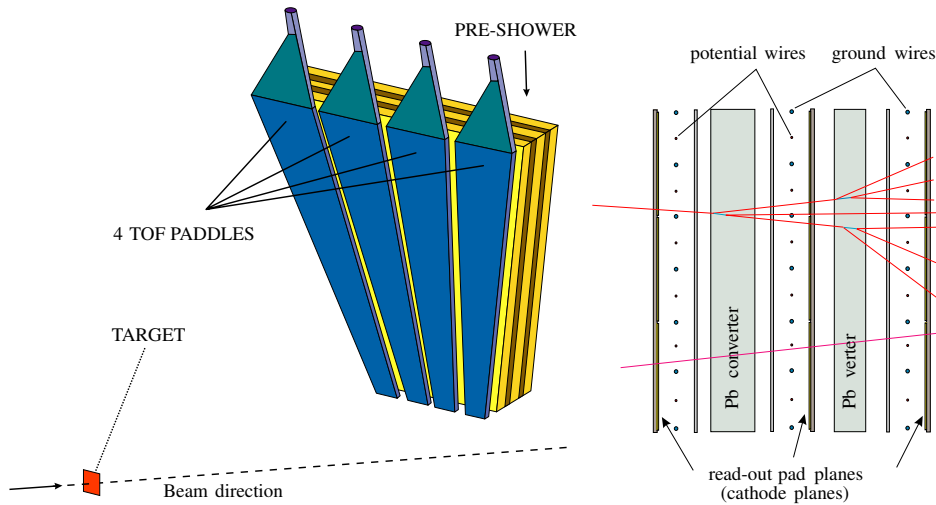


**Figure 4.9:** The SHOWER detector. Three gas chambers and two lead converters. Lepton/hadron discrimination is done by comparing the number of particles before and after the lead converters.

### The Pre-Shower Detector

Electrons (or positrons) travelling through any material lose energy by radiation (*Bremsstrahlung*). If the energy of the initial electron is sufficiently high, the radiated photons will have enough energy to produce an electron-positron pair which will again radiate photons via Bremsstrahlung. Thus, an initial high energy electron will produce a cascade of low energy particles after crossing any material, in what it is known as electromagnetic shower. The radiation probability of the bremsstrahlung radiations, which initiates the shower, is proportional to  $1/m^2$ . Hence, light particles like electrons or positrons are more susceptible to produce electromagnetic showers than heavier particles like pions or any hadron ( $m_e^2/m_\pi^2 \simeq 1.3 \cdot 10^{-5}$ ).

The Pre-Shower detector (fig. 4.9) uses the information of the generation of electromagnetic showers to separate electrons from hadrons at forward angles,  $\Theta = 18^\circ - 45^\circ$  [Bal04a, HAD].

As it can be noticed in the figure 4.9 (right), the detector is composed of a stack of three wire chambers (named *pre-chamber*, *post1-chamber*, *post2-chamber*), with two interleaved lead converter plates.

Charged particles flying through the gas chambers produce an ionisation avalanche with electrons drifting towards the closest anode wire. Moving electrons induce a positive charge on the nearby cathode pads. By integrating

the charge in the three read-out planes the occurrence of a shower can be determined. The searching algorithm works as follows:

- Find a local maximum of the charge distribution in the *pre-chamber*.
- Integrate the charge over an area of 3 x 3 pads for all the three chambers (see fig. 5.8).
- Apply the electron identification algorithm, i.e.

$$\frac{Sum_{post1}}{Sum_{pre}} \geq Threshold_1$$

or

$$\frac{Sum_{post2}}{Sum_{pre}} \geq Threshold_2$$

where  $Threshold_i$  can be a fixed number or a function of the momentum. The Pre-Shower detector has been working already for several years integrated in the HADES setup. The mass resolution achieved with the inner MDC chamber reaches  $\Delta M/M = 10\%$  (for  $p = 0.6 GeV/c$ ) with a electron detection efficiency of circa 80% and a hadron rejection ratio of 90 % (combined with the inner part of the time of flight wall, the TOFino detector, see next section) [Bal04a].

### The Time of Flight Wall

Due to their low mass, primary electrons in HADES travel faster than hadrons, almost with the velocity of light ( $\beta_{p=100MeV}^e = 0.9975$ ). This makes the measured time of flight a good parameter to distinguish leptons from hadrons, especially at low momentum.

In HADES as part of the META or outer-most detector system there is a time of flight wall (fig. 4.10), made of fast scintillating fibres, that covers the whole acceptance. The wall is divided in two parts. The so called **TOF** detector covers with high granularity the polar range from  $44^\circ - 85^\circ$ . The **TOFino** detector covers the  $\Theta$  region from  $18^\circ$  up to  $50^\circ$ . In this region, the time of flight measurement is complemented with the Pre-Shower detector, so no such high granularity as for TOF is needed. Finally, the TOF + TOFino system does more than measure time. It records information for trigger purposes. We can summarise its task in three point.

- **Determination of the particle multiplicity**

The TOF is probably the fastest detector to be readout in the spectrometer. The information of number of hits in the TOF wall can be



**Figure 4.10:** Photograph of the *Time Of Flight*, **TOF**, detector. The 6 sector symmetry is apparent.

retrieved very fast providing information about the centrality of the reaction in a heavy ions collision. This is used as *first level trigger* in the HADES DAQ [Tra01, Gar93].

In proton-proton reactions, the interest is to know whether or not an inelastic reaction took place. For that purpose configurations were set to trigger on events with a multiplicity equal or greater than four (relevant to detect one meson production like  $pp \rightarrow pp\eta \rightarrow pp\pi^+\pi^-\pi^0$  or  $\eta \rightarrow e^+e^-$ ), or events with two hits in opposite sectors (in elastic reactions the two proton are coplanar, hence  $\Delta\phi = 180^\circ$ ).

- **Fast tracking**

The TOF as part of META, provides fast rough position information of the hits used for the online matching of tracks in the LVL2 trigger system (see chap 5 about the Trigger System).

- **Determination of the *Time of Flight***

Necessary data to reconstruct the velocity of the particles and one of the signatures checked by the Trigger System while searching lepton traces.

### The TOF Detector

The Scintillating material chosen for TOF is BC408 from Bicron<sup>®</sup> [Bic]. Its speed (2.1 ns), efficiency ( $\approx 10^4$  photons/MeV) and attenuation (3.8 m in bulk), made it suitable for HADES purposes [Ago02].

The material is cut into 64 rods of square cross section per sector. The first 32 rods ( $\Theta = 44.0^\circ - 61.7^\circ$ ) have a size of 20x20 mm (i.e.  $\Delta\Theta \sim 4.5^\circ$ ). And rods from 32 on ( $\Theta = 61.7^\circ - 87.8^\circ$ ) have a section equals to 30x30 mm (or  $\Delta\Theta \sim 6.2^\circ$  to  $7.0^\circ$ ). This ensures a finer granularity in the more forward angular region, where more particles are being produced.

Each rod is being read out at both ends by photomultipliers, which record the information of time and amplitude.

With this data the time of flight ( $ToF$ ), hit position ( $x$ ), deposited energy ( $\Delta E$ ) and redundant hit position can be reconstructed like [Ago02]:



**Figure 4.11:** Photograph of one of the TOF Photomultipliers together with the curved light guides used to couple them to the scintillating rods.

$$ToF = \frac{1}{2} \left( t_{right} + t_{left} - \frac{L}{V_g} \right) \quad (4.6)$$

$$x = \frac{1}{2} (t_{right} - t_{left}) V_g \quad (4.7)$$

$$\Delta E = k \sqrt{a_{left} a_{right} e^{L/\lambda_{at}}} \quad (4.8)$$

$$\tilde{x} = \frac{\lambda_{at}}{2} \ln \left( \frac{a_{left}}{a_{right}} \right) \quad (4.9)$$

where  $t_{right, left}$  is the arrival time right/left,  $L$  the rod length,  $V_g$  the groups velocity  $a_{right, left}$  the light amplitude, and  $\lambda_{at}$  is the light attenuation length of the rod.

The TOF detector has proved an experimental time resolution of  $\sigma_{TOF} \leq 150$  ps and a spatial resolution along the rod of  $\sigma_X \leq 25$  mm with efficiencies next to 100% ( $\varepsilon \approx 0.959$  to  $0.957$ ) [Ago02].

### The TOFino Detector

At forward angles, due to the Lorentz boost, hadrons trend to have higher momentum. In that case the velocity, and hence the time of flight, difference of hadrons and lepton is not so significant. For that reason, in the polar region from  $18^\circ$  to  $50^\circ$ , the measure of time if complemented with the detection of electromagnetic avalanches produced by electrons in the Pre-Shower detector (section 4.2.5).

The **TOFino** detector (fig. 4.12) is constituted by four scintillating bars per sector which are read out at one end only [Toi04]. Therefore, the spatial, as well as, the time resolution and the double hit capabilities of the detector are considerably reduced. The TOFino detector is then only suitable for low multiplicity environments. It has been successfully used in p+p, C+C and Ar+KCl reactions. For heavier elements, the occupancy would be too high. To overcome this issue, a new detector is being developed. The *resistive plate chamber*, RPC (section 4.3.1). The RPC will provide the high granularity needed for heavy ion reactions like Au+Au.

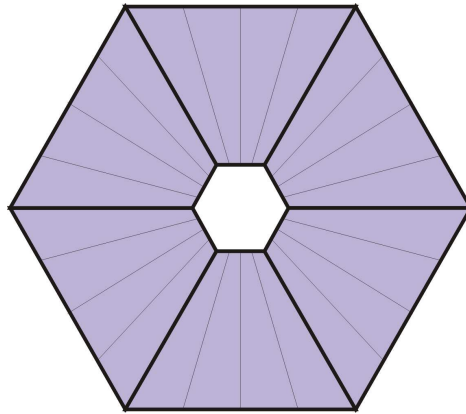


**Figure 4.12:** Schematic view of the **TOFino** detector with the four scintillator plates per sector.

## 4.3 New Developments

Due to the requirements needed for very heavy systems like Au+Au and the experiments with pion beams, the HADES detector has still room for improvement. It is foreseen that for very high multiplicity systems the **TOFino** detector will saturate; the occupancy would be next to 100%. For that reason the *Resistive Plate Chamber*, **RPC**, detector is being developed.

### 4.3.1 Resistive Plate Chambers: RPC

A Resistive Plate Chamber is a gaseous parallel-plate detector that combines the spatial resolution of the wire chambers with the time resolution typical of a scintillation counter. The chambers are constituted by 2 mm aluminium and glass electrodes with a surface of 20 x 600 mm [Alv04]. Each stack

of three aluminium plus two glass electrodes is encapsulated in a grounded shielding box in order to minimise the cross-talk. First in-beam test under realistic conditions shown time resolution in the order of  $\sigma \sim 75$  ps [[Alv04](#)].

# Chapter 5

## The Trigger System

The HADES's trigger system is a real-time computational system dedicated to select electron-positron pair candidates out of a high number of particles produced in nuclear collisions.

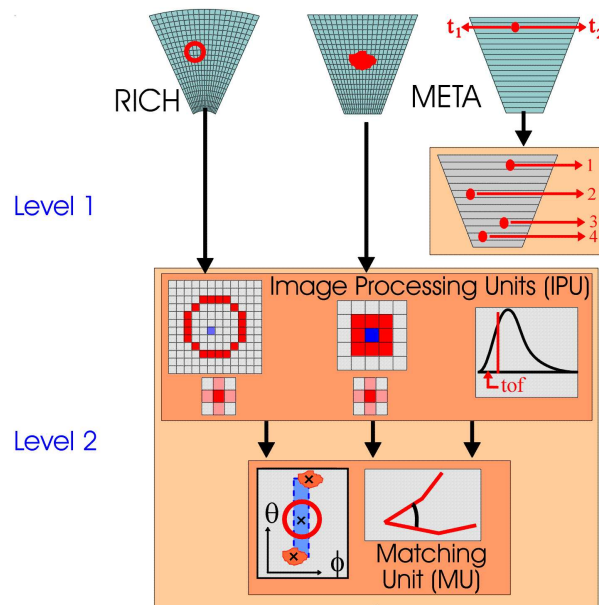


**Figure 5.1:** The two levels of the HADES Trigger System.

The trigger system is custom made to fit the requirements of HADES. Its processing units are based on Programmable Logic Devices (FPGA and CPLD) and DSP technologies. To achieve a high performance, it is necessary to optimise data throughput and latency. Latency is kept always below  $200 \mu s$

via pipelining and exploiting at maximum the parallelism of the problem, basically each hit of each track in each subdetector is an independent entity.

The selection of relevant events is performed in a two level system, as it is schematically shown in the figure 5.1 [Leh99, Tra00]. The first level filters the most central collisions and the second level searches for leptonic signatures in the tracks.

## 5.1 The First Level Trigger: Centrality Trigger

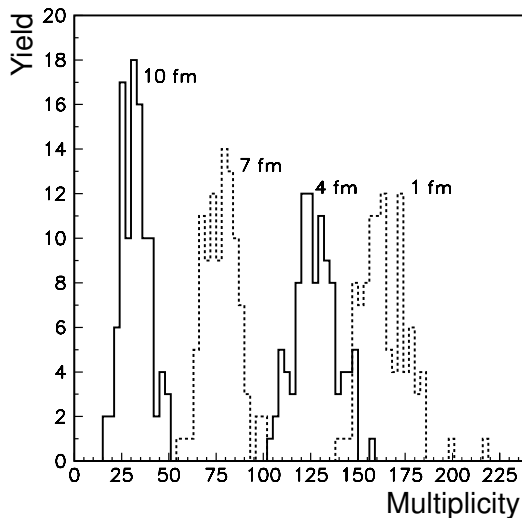


**Figure 5.2:** Histogram of charged particle multiplicities in simulated Au+Au collisions at 1 AGeV for several impact parameters  $b$  [Gar93].

The *First Level Trigger* (**LVL1**) selects the most central events by setting a filter on the particle multiplicity detected in the TOF wall. Higher the particle multiplicity implies more nucleons participating in the reaction and, therefore, smaller impact parameters.

The signals produced in the TOF wall (**TOF** + **TOFino**) are collected and added in the **Multiplicity Trigger Unit** or **MTU**, which, after a discrimination, delivers the LVL1 trigger.

Based on the simulations shown in the fig. hello 5.2 hello [Gar93], a proper selection of the impact parameter like  $b < 4 fm$  will reduce the event rate by a factor 10, bringing down the first level trigger to a rate of ca.  $10^5 Hz$  [Leh99, Tra01].

After a first level trigger is distributed to all the subdetectors (Fig. 5.3), the data are digitised, read out and then stored in FIFOs, the *First Level Pipe*. There they will remain until a second level trigger arrives. In case of a

positive LVL2 trigger decision, they will be sent to the *Event Builder*, where data from all subdetectors are combined together.

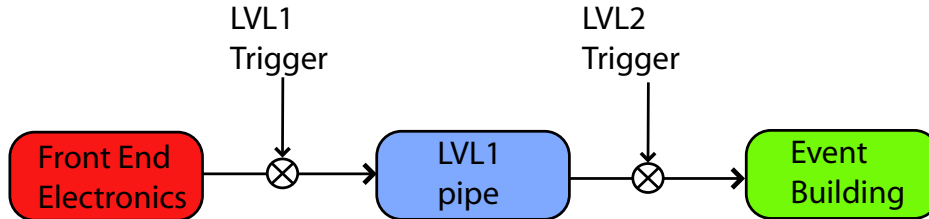


**Figure 5.3:** Data flow in the HADES trigger. After the LVL1 trigger, data are read out and stored in the first level pipe. Then, the system waits for the LVL2 trigger. If the LVL2 trigger is positive the data will be forwarded to the event builder, else they will be discarded.

## 5.2 The Second Level Trigger: Lepton Trigger

The Second level trigger (LVL2) is build to select events containing  $e^+e^-$  pairs in a certain invariant mass region. Out of the four detectors of HADES only data from the three fastest are evaluated online to produce a second level trigger decision. These are **TOF**, **Pre-Shower** and **RICH**.

The Second Level Trigger is split into two steps. First, independently in each detector, the Image Processing Units (IPU) collect a subsample of the data and evaluate the *lepton conditions*. These conditions are a *ring* in the RICH detector, an electromagnetic shower in the Pre-Shower and time of flight in a certain window in the TOF wall.

Each IPU, after evaluating the lepton condition, sends the data of the possible candidates and their angles to the **Matching Unit**, MU. In the Matching Unit, the information of the three IPUs is combined and a scan for electron/positron pair candidates is performed. From the combination of the momenta of electrons and positrons (it can be calculated from the polar deviation between RICH and META) and their opening angle the Matching Unit can reconstruct the invariant mass of the pair and, eventually, make a selection based on a certain programmed window.

Such a selection may bias the final shape of the dielectron spectrum and affect physics results. Therefore it is necessary to study how the different trigger conditions affect the data. For that purpose comparisons between triggered and downscaled data have been performed [Toi04, Leh03] (details about the performance of the trigger system will be shown in the section 5.4).

### 5.2.1 The RICH Image Processing Unit

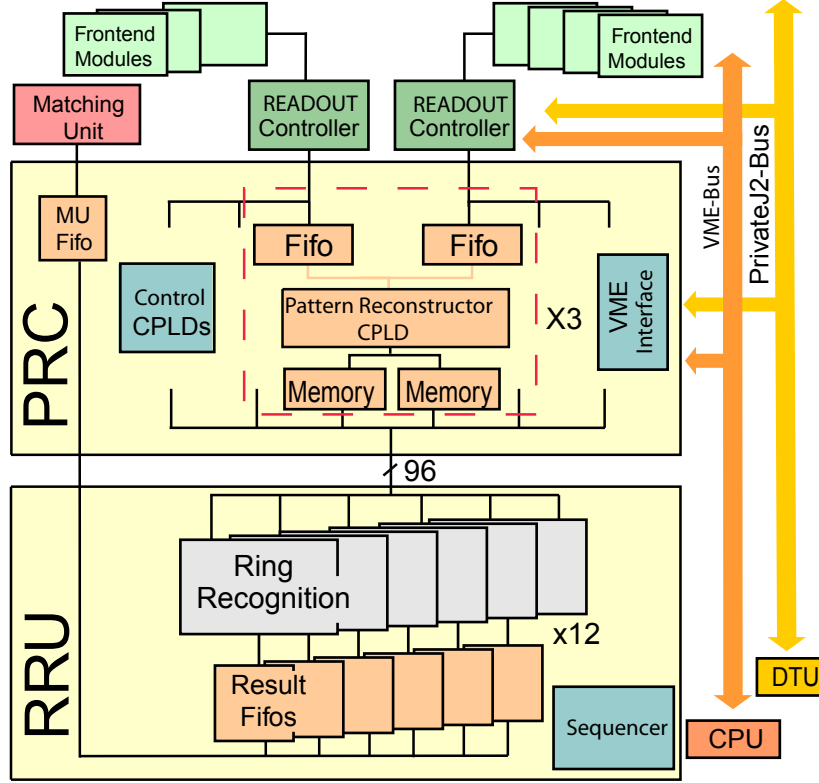


Figure 5.4: Block diagram of the RICH Image Processing Unit [Leh99].

The Image Processing of the RICH is the most selective algorithm of the second level trigger. In the SIS energy regime, almost all the electrons have velocities next to the velocity of light in vacuum ( $\beta_{P=100MeV/c}^e = 0.9999$ ). Therefore, they produce a Cherenkov light cone with a constant opening angle of  $\Theta_c = \arccos(1/n)$  (eq. 4.2) when traversing the radiator of the RICH detector. The Cherenkov light cone is reflected by the RICH mirror as rings of equal radius onto the detector pad plane.

To identify electron signatures out of all the signals in the detector, like electronic noise, fast pions or particles hitting directly the detector pad plane, the RICH IPU performs a parallel scan on each of the 96 columns of the pad plane searching for possible rings [Leh99].

In hardware, the IPU is implemented as two 6U-VME boards per sector. A *Pattern Reconstruction Card* (PRC) and a *Ring Reconstruction Unit* (RCU).

### Pattern Reconstruction Card

The position information of all the *fired* pads (amplitude over certain programmable thresholds) is transferred from the RICH readout controllers (RC) to the PRC. There, a virtual plane of 96x96 pads is reconstructed (The RICH pad plane has a circular shape divided into six sectors. For simplicity of the hardware implementation, each detector plane is mapped into a square of size 96x96 pads where many of them do not have a connection with the actual detector).

A schematic overview of the data path can be seen in the figure 5.4. Each RRU is attached to two readout controllers. The data words are transferred from the RCs in parallel and presorted in three FIFOs 32 columns wide. Each buffer FIFO is connected to two 16-bit wide dual ported SRAM where the hit pattern is stored. The SRAMs are divided into 32 pages, each of them containing the complete pattern of one event [Leh99]. The data are then transported to the RRU via a dedicated 96-bit wide bus.

### Ring Reconstruction Unit

The ring recognition is performed in parallel for all the 96 columns by 12 Xilinx XC4028EX FPGAs [XIL] (8 ring recognition units per FPGA). Every pad (96x96=9216) is evaluated as a possible centre candidate. For each candidate a square of size 13x13 is analysed (see Fig 5.5). In this area three regions are defined, an internal and external *veto* region (light grey in fig. 5.5), and a *ring* region (dark grey). In each ring and veto regions, the ensemble of pads linked with dots of the same colour are logically *OR*ed and the results are added. This is almost as efficient as adding all the pads while it reduces highly the amount of resources needed [Leh99]. *OR* gates are smaller than *adders* and abundant in FPGAs. A *ring* is found if the sum over the ring region is greater than the *Ring Threshold* and the sum over the veto region is smaller than the *Veto Threshold*. By varying the

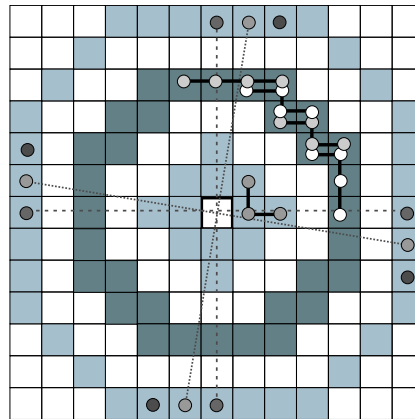


**Figure 5.5:** Ring recognition searching mask. The ring region and the inner/outer veto regions are shown. Pads are not added individually, but rather grouped to save resources [Leh99].

thresholds between ring and veto region one can find the best trade-off between ring finding efficiency and *fake* ring production [Leh99, Leh03]. These thresholds have to be evaluated for different operation conditions (system multiplicity, noise, high voltages in the detector etc). The pipelined realisation of the algorithm in the FPGAs allows the ring finding to be performed in about  $10 \mu\text{s}$ .

After the ring finding procedure, the results are collected in the PRC from where they are read out by the Matching Unit through the 20 MBytes/s RS485 common bus.

### 5.2.2 The TOF Image Processing Unit

As a lepton signature the TOF IPU searches for particles which reach the *time-of-flight* wall (angles from  $45^\circ - 85^\circ$ ) with a given velocity [Lin01]. Electrons, or positrons, due to their low mass, fly in average with higher velocities. Hence they are prone to reach the TOF wall faster than hadrons [Gar93] (see figure 5.6).

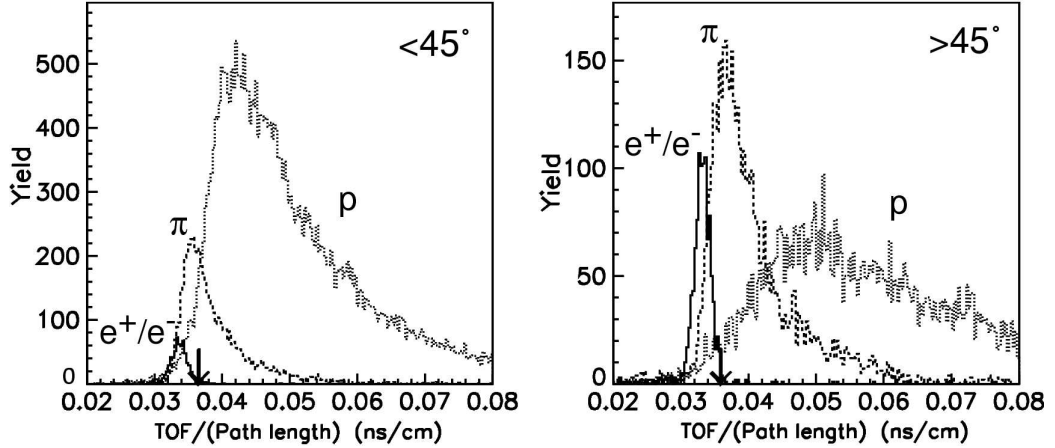


**Figure 5.6:** Simulation of velocity distribution for different particle species in central Au+Au collisions. Separation based on velocity is more effective for polar angles  $> 45^\circ$  (right) than for angles below  $45^\circ$  (left) [Gar93]. In that region the TOF measurements are complemented with the production of electromagnetic avalanches in the Pre-Shower detector.

The goal of the TOF trigger unit is to deliver the polar and azimuthal angles of lepton candidates to the Matching Unit [Frö02]. The IPU receives 2 TDC (Time to Digital Converter) and 2 ADC (Analog to Digital Converter) values per scintillation strip. The TDC values correspond to the time difference

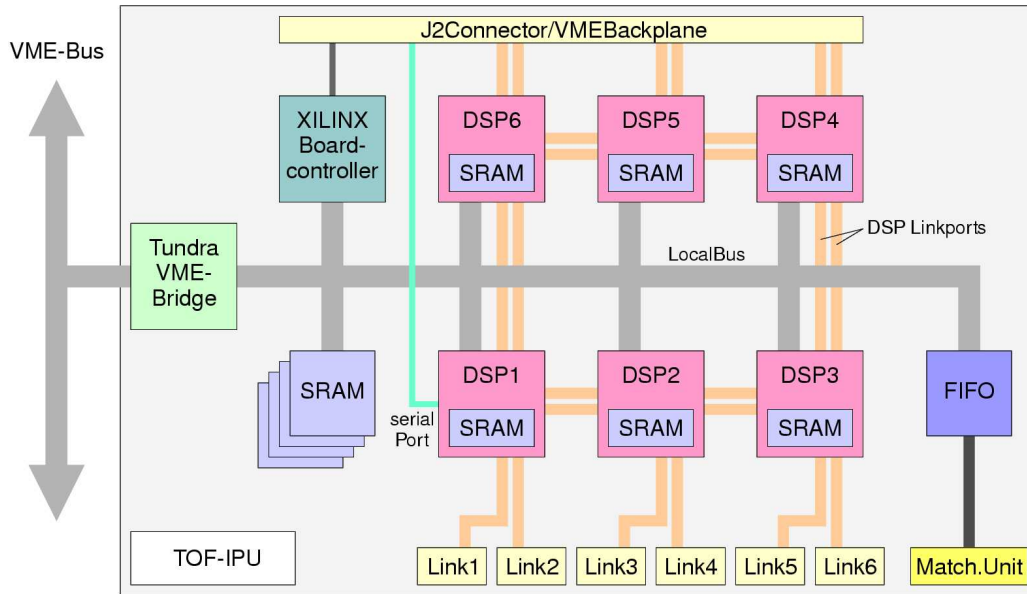


**Figure 5.7:** Block diagram of the Image Processing Unit of the Time-Of-Flight detector

between the start signal and the stop signal. On these values the IPU has to perform the following operations to extract the data to be send [Lin01, Frö02].

1. Calculate time out of TDC channel number (linear function).
2. Walk correction of ADC values.
3. Add time signals in both sides of the rods and, when present, correct the time-of-flight with the time in the START detector.
4. Calculate the position along the rod.
5. Extract  $\theta$  and  $\varphi$  from the position along the rod.
6. Apply the time-of-flight cut and send this information to the matching unit.

The algorithm on the IPU performs less operations than the one in the RICH IPU, but the kind of operations are more complicated. Hence the hardware was designed using DSPs instead of FPGAs as computational units [Lin01]. The chips selected were ADSP-21062 „Sharc” from Analog Devices [AD]. They are able to perform linear operations of the type  $a(x) = b \cdot x + c$  at rates of 40 millions per second (40 *MFlops*). A block diagram of the TOF

IPU can be seen in figure 5.7. The data flow approximately from left to right. They are, first, collected from the VME bus by the VME bridge (SCV64 from Tundra) and stored in the 4 MBytes SRAM which acts as LVL1 pipe, from where the master DSP (DSP XXX) will retrieve an event and dispatch the order to process it to the next free DSP. Events are stored in a FIFO after being processed. There they wait to be sent to the Matching Unit. After receiving a positive LVL2 trigger, the master DSP will initiate the transport of data from the LVL1 pipe to the concentrator module. Each IPU serves two TOF sectors. The concentrator receives data from the three TOF IPU's and builds up complete TOF subevents which are then send to a central workstation acting as event builder [Lin01].

### 5.2.3 The Shower IPU

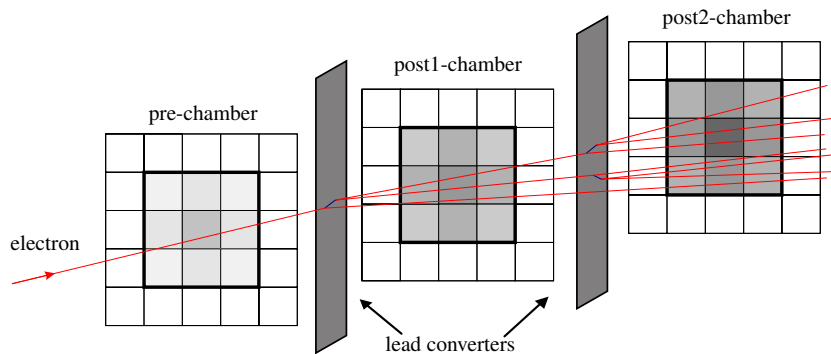


**Figure 5.8:** Scheme of an electromagnetic *shower* with the 3x3 pad integration area depicted.

The duty of the Shower IPU (figs. 5.8 and 5.9) is to identify electron/positron signatures in the Pre-Shower detector [Pet00]. This is performed by an on-line comparison of the charge deposited in each of the three wire chambers of the detector. The IPU is in charge of reading out the detector, meaning that it has to cope with the full 8 bit digital information of the pulse height in each of the 16956 pads. First level trigger rates of  $10^5$  Hz imply an input data rate in the order of 2 GBytes/s [Ba198, Pet00].

The algorithm is implemented in FPGAs, in parallel for every column and then pipelined row by row. Besides the operation needed as readout controller (sub-event building, zero suppression, calibration etc.), the image processing algorithm is segmented into two major steps.

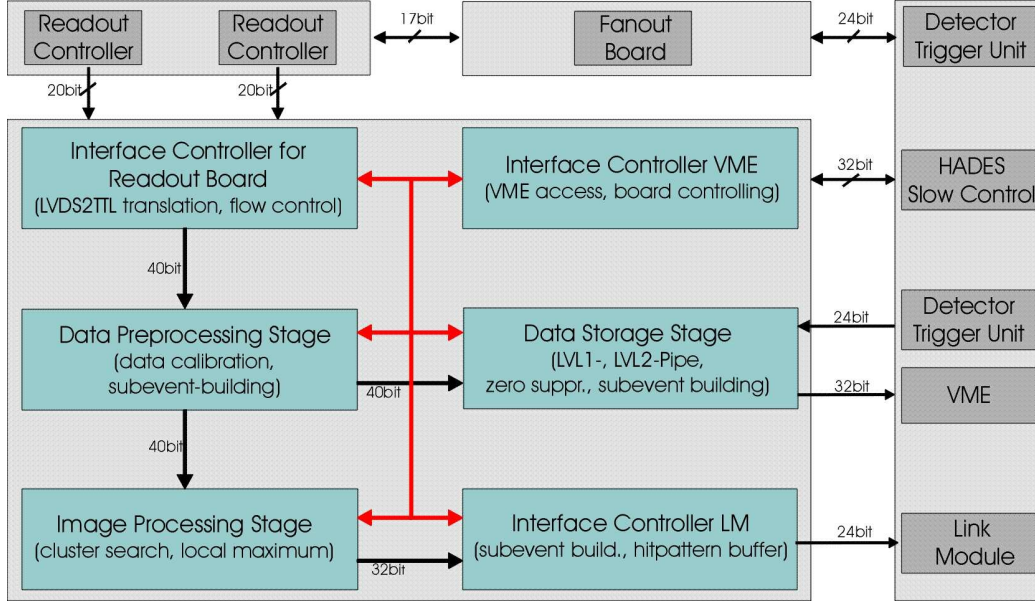


**Figure 5.9:** Diagram of the functional blocks of the Shower IPU. Black arrows show the data flow [Pet00].

### 1. Local maximum search.

In blocks of 3x3 pads a maximum is found evaluating the following relation:

$$Pad^{pre}(m, n) > Pad^{pre}(i, j)$$

where  $(i, j) = (m, n - 1); (m + 1, n)$ .

$$Pad^{pre}(m, n) \geq Pad^{pre}(i, j)$$

where  $(i, j) = (m - 1, n); (m, n + 1)$ . Note that the condition is asymmetric to ensure there is always a maximum found.

### 2. The shower condition.

By comparing the charge accumulated in a region of size 3x3 pads in each of the three layers as follows:

$$Q^{postI, postII}(m, n) > Q^{pre} + Q^{threshold}$$

where  $Q$  is defined as

$$Q(m, n) = \sum_{i=m-1}^{m+1} \sum_{j=n-1}^{n+1} Pad(i, j)$$

### 5.2.4 The Matching Unit

The Matching Unit, MU (fig. 5.11), is in charge of combining lepton signatures coming from the different IPUs and producing the second level decision [Tra00, Leh99].

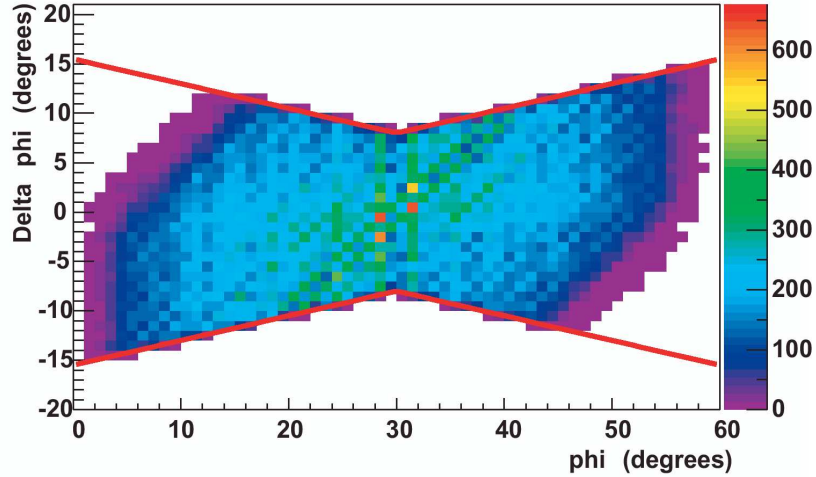


**Figure 5.10:**  $\Delta\phi$  ( $\phi_{RICH} - \phi_{META}$ ) as a function of  $\phi_{RICH}$  of all the leptons found by the Matching Unit. All the hits are inside the azimuthally variable matching window, marked in red [Toi04].

The position information of lepton candidates is sent from the IPUs to the Matching Unit. The Matching unit tries to correlate every ring in the RICH detector with any hit in META inside a *matching window*. As a first approximation, assuming a perfectly toroidal magnetic field, particles in the magnetic field suffer a deflection only in polar direction. In that case, the matching window should have a  $\Delta\phi$  in the order of the detector resolution and  $\Delta\theta$  which covers the whole detector range. In reality, due to the inhomogeneity of the magnetic field and other effects like misalignment or multiple scattering, particles are actually deflected also in the azimuthal direction. Therefore, the actual matching window has the irregular *butterfly* shape shown in the figure 5.10. It is narrow in the centre of the sector and wider towards the edges [Toi04].

Once the match is performed, from the polar deflection, calculated as  $\theta_{RICH} - \theta_{META}$ , the momentum of the particles can be reconstructed. From the sign of the deflection, electrons and positrons can be identified. Electrons are deflected towards the beam whereas positrons have a kick outwards.

The opening angle between two tracks is calculated as:

$$\cos \omega = \frac{\vec{a} \cdot \vec{b}}{a \cdot b}, \quad (5.1)$$

where  $\vec{a}$  and  $\vec{b}$  are the vectors calculated from the coordinates of the hits in RICH minus the target position. With the opening angle and the momentum of each lepton the invariant mass is calculated from:

$$m_0^2 = \frac{2p_1 p_2 (\sin \frac{\omega}{2})}{c^2}. \quad (5.2)$$

The Matching Unit is able to calculate the invariant mass of lepton pairs and, eventually, to apply cuts to enhance certain interesting physical regions. For the HADES programme that would be the mass region between 100 and 700 MeV [HAD94, Tra01].

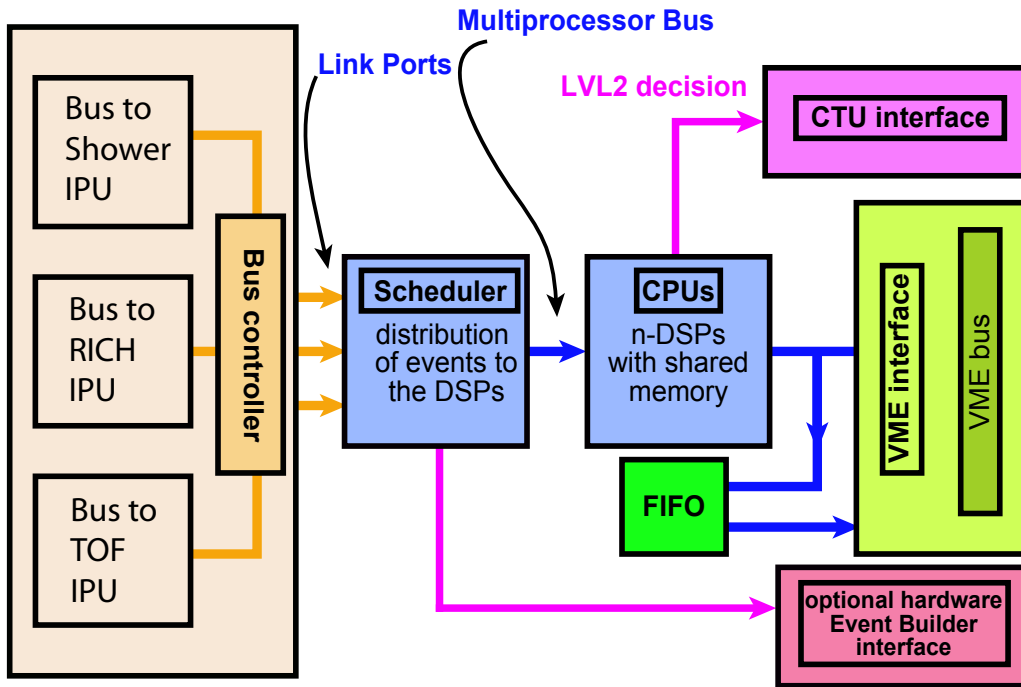
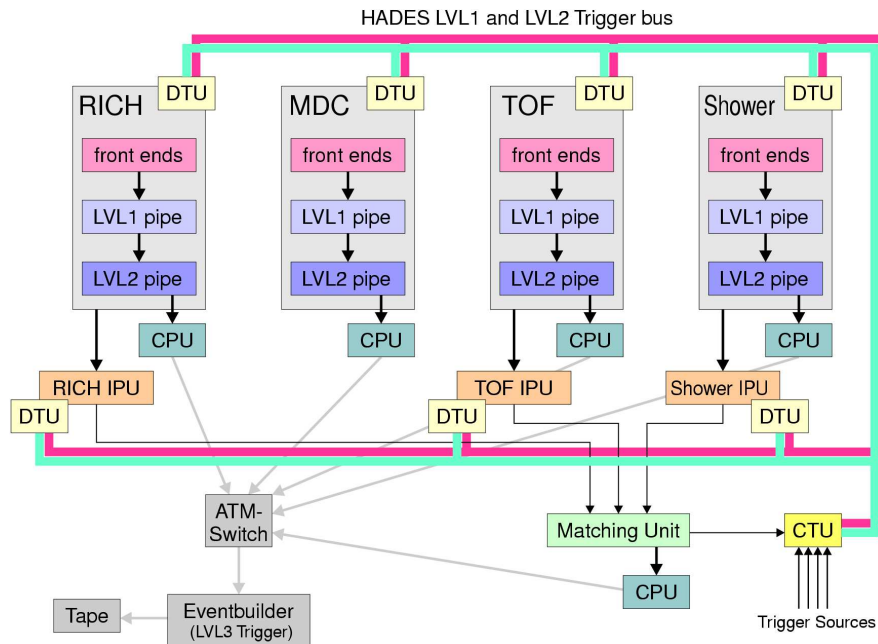


Figure 5.11: Block diagram of the Matching Unit [Tra01].

For the actual hardware a DSP based architecture implementation was chosen. To achieve the timing requirement of the online trigger, the Matching Unit exploits at maximum the parallelism of the problem. A central DSP acts as scheduler, it builds up the events and distributes them to the processing DSPs which will perform the matching algorithm. Each event is an

independent unit and is treated in parallel. Thus, even if the processing time for the single event is big, the average delay between two consecutive Matching Unit decisions can be kept below  $10 \mu\text{s}$  [Tra01].

### 5.3 The Trigger Distribution System



**Figure 5.12:** Schematic view of the Trigger Distribution System [Lin01].

The HADES spectrometer is composed of various independent subdetectors. They work independently and asynchronously from each other. The Trigger distribution system has the task to synchronise the data taking and information flow.

We can summarise the tasks of the trigger distribution system in three points:

- Distribute the trigger signal and trigger code. In order to keep all the subsystems synchronised, data taking is only allowed after a LVL1 trigger has been sent. A trigger will only be sent if all the detectors are not busy and ready to acquire data. Along with the trigger signal four bits of control data, the trigger code, are sent.
- To be able to build up an event out of the data coming from the different subdetectors, every subevent has to be *tagged* uniquely so that

the event builder can match subevents together. The trigger distribution system distributes along with each trigger a unique identifier, the trigger tag.

- HADES is a very complex and large system where electrical signals may travel several meters through cables between two modules. The trigger distribution system accounts for this delays by setting appropriate *deadtimes* to avoid race conditions.

A topology with a central hub, the *Central Trigger Unit (CTU)*, and several detector specific trigger units, *Detector Trigger Unit* or **DTU**, was chosen [Lin01]. The basic operation is illustrated in the figure 5.12.

### LVL1.

The **CTU** generates the LVL1 trigger out of one of the trigger sources (typically Multiplicity Trigger from MTU, downscaled or calibration triggers). Then, if none of the detectors is BUSY, it sends the LVL1 trigger to all DTUs through the HADES trigger bus. Each DTU interfaces the trigger bus with each subdetector and each IPU. The LVL1 trigger starts the data acquisition and digitisation in each of the detectors. The digitised data are stored in the LVL1 pipe (fig. 5.3).

### LVL2.

The Matching Unit, after processing an event, generates the LVL2 trigger, which is forwarded to the CTU. The CTU then distributes the LVL2 trigger in the same way as the LVL1 trigger. For the point of view of the trigger distribution system, LVL1 and LVL2 events are parallel and independent.

#### 5.3.1 The Trigger Bus

Each LVL1 and LVL2 trigger contains the trigger signal itself plus a trigger code and a trigger tag.

The distribution of the trigger data is done via a dedicated trigger bus. Each trigger level has 10 dedicated lines to communicate. A description of the signals in the trigger bus is shown in the table 5.1.

The timing diagram of the transmission of one trigger over the trigger bus can be seen in the figure 5.13. The transmission time is 1  $\mu$ s. To account for propagation time on the lines and delay in the response of the different

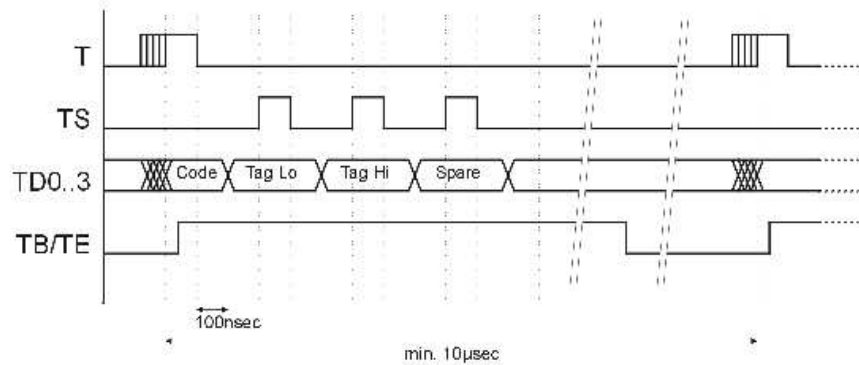


**Figure 5.13:** Timing diagram on the trigger bus. The total transmission time is  $1 \mu\text{s}$ ; TB is kept high longer to account for delays in the lines and reaction time of the different subsystems.

subdetectors to hold the BUSY, a programmable *deadtime* is implemented. The typical working deadtime is around  $1.6 \mu\text{s}$ .

Signal	Function
T	<b>Trigger</b> Trigger signal itself. Asserts the TRIGGER CODE
TS	<b>Trigger Strobe</b> Asserts each of the data words in the data lines
TD[0..3]	<b>Trigger Data [0 – 3]</b> Data line to transmit the TAG and CODE
TB	<b>Trigger Busy</b> "wired-OR" Busy signal of all DTUs
TE	<b>Trigger Error</b> "wired-OR" Error signal of all DTUs
TRES1/ TRES2	<b>Trigger Spare</b> not used

**Table 5.1:** Description of the signals in the HADES's Trigger Bus [Lin01].

### The Trigger Tag

The trigger tag is an 8-bit word (0 – 255) attached to every triggered event. It serves as unique identifier of the event. The normal length of the level one pipes is around 20 events for all the detectors [Tra01], so eight bits are more than sufficient. The trigger tag is transmitted with the first and second *trigger strobes*, TS (Fig. 5.13).

### The Trigger Code

The TRIGGERCODE is a 4 bit word that encodes information about the type of trigger. It is transmitted as the first data word in the trigger bus asserted by the Trigger signal (see 5.13).

### 5.3.2 The CTU/DTU Hardware

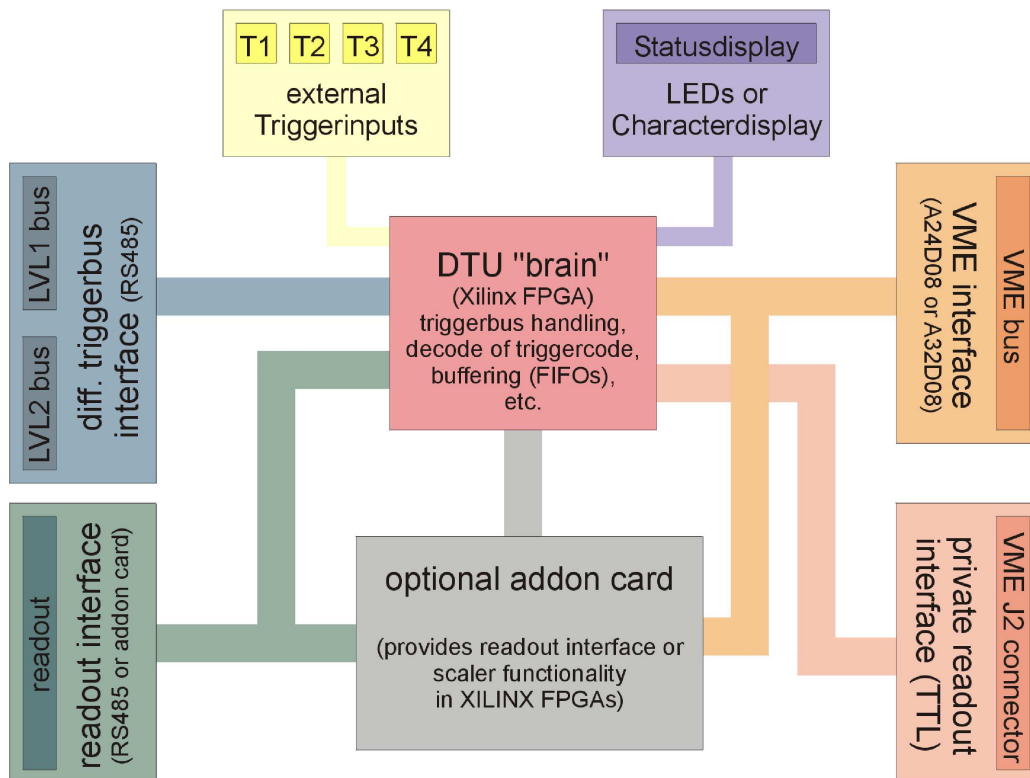


**Figure 5.14:** Diagram of the logic blocks in the DTU/CTU VME module [Lin01].

The CTU/DTU is implemented on a custom designed 6U-VME card with programmable electronic devices (FPGA and CPLD) as processing units and several interfaces to communicate with the different systems (trigger bus, VME interface plus the DTU-readout electronics communication for the different subdetector).

A block diagram of the DTU/CTU module can be seen in the figure 5.14.

The main component of the board is the “Xilinx XC4010E” FPGA. The FPGA can be programmed to adapt the board to the different needs of the

CTU of any of the different DTUs. The standard way to address the programming of FPGAs is either via a schematic based proprietary tool, like “View Logic” and “Xilinx ISE”, or using a high level programming language like VHDL, Verilog or SystemC. The programming of the CTU and the base functionality of the DTUs was developed by E. Lins and described in [Lin01] (for the development of the RICH DTU refer to [Böh99]). The programming of the CTU/DTU system was realised using a schematic based tool entry tool (“viewlogic, Workview Office v7.3”).

As a part of this thesis, the base functionality of the DTU has been ported to VHDL and the DTUs for MDC and TOF subdetector have been reprogrammed. VHDL offers important advantages over any schematic entry tool. It is a high level programming language and a IEEE standard. The design is written in plain text. Thus it is easier to maintain and modify. The design can be implemented with standard logical functions, this allows an abstraction of the actual hardware platform where the design is going to be fitted to. Hence the same code can be recompiled for several architectures.

This has been tested during the development of the firmware for the new readout electronics of the new RPC detector. The *basic* DTU code has been successfully embedded into a “Xilinx Spartan II” FPGA, *brain* of the new combined readout controller and Trigger module.

### 5.3.3 The DTU logic

As the LVL1 and LVL2 trigger buses work asynchronous and independently, the DTU also follows that philosophy and has two parallel pipes to process the LVL1 and LVL2 trigger data (fig. 5.15).

#### TriggerBusInterface

The trigger bus is interfaced by the `TRIGGERBUSINTERFACE` (LVL1 and LVL2). It receives the sequential data and sets the data on two buses, the `TRIGGERCODE` (4 bit) and the `TRIGGERTAG` (8 bit); then asserts the `DATAVALID` signal which starts the LVL1 and LVL2 State Machines.

#### LVL1/LVL2 State Machine

Code and Tag are received by the `LVL1StateMachine` or `LVL2StateMachine`. These modules are conceived as *Finite State Machines*. They check the `CODE`, and compare the `TAG` with the value of the counter. If `TAG` and `CODE` are correct, data are sent to the interface with the detector specific

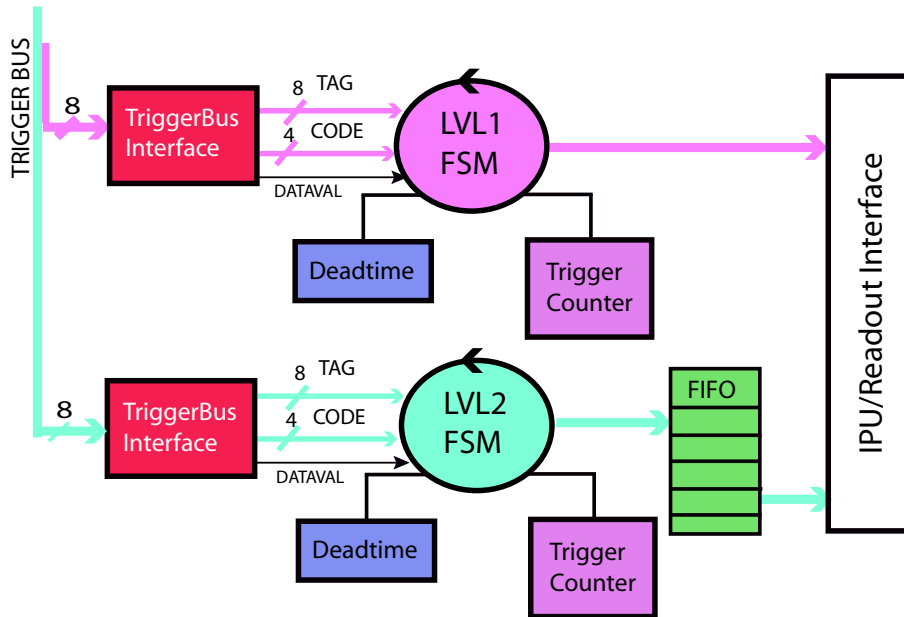


**Figure 5.15:** Block diagram of the basic functions in the DTU's FPGA.

block (LVL1) or stored in a FIFO (LVL2). Otherwise, the state machines will reach an error state. In this state, the error line of the `TRIGGERBUSINTERFACE` is asserted and no further process is possible. The LVL1/LVL2 state machines also set a `BUSY` while processing. The LVL1 State machine is busy since `DATAVAL` is received until data are sent to the readout controller. The LVL1 state machine waits for the communication with the readout controller to be successfully finished. The LVL2 is busy from the arrival of `DATAVAL` until the tag and code are written into the FIFO.

Besides the logical busies set by the state machines, a programmable *dead time* is foreseen. The `DEADTIME` module is started with the rising edge of the `DATAVAL` signal. It reads the value of the 8-bit wide `deadtime_register` (this is accessible via VME), and sets `deadtime_busy` high for some time proportional to the value in the register. The `deadtime_busy` and the busy of the state machines are *ORed* and then linked to the `BUSY` line in the `TRIGGERBUS`.

For the communication with the readout electronics and IPU's of the different detectors there are several solutions.

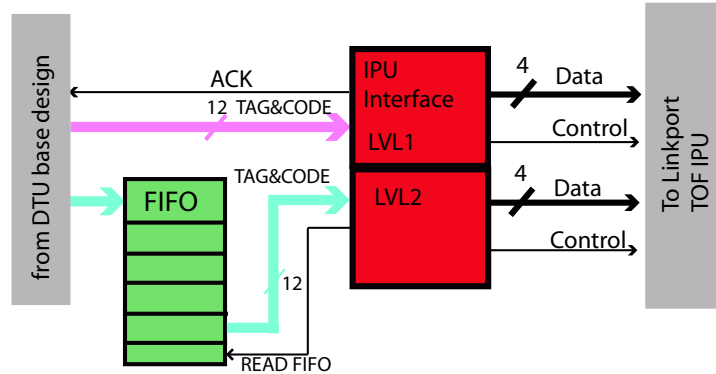


**Figure 5.16:** Block diagram of the TOF DTU.

### TOF DTU

The TOF IPU and readout controller board system provides two parallel buses to receive the trigger data from the DTU. LVL1 and LVL2 are transported independently and in parallel (fig. 5.16). The IPU INTERFACE translates the data (TRIGGER TAG and CODE) from the 12 bit wide bus to three serial 4 bit words on the IPU link.

### MDC DTU

The MDC DTU (fig. 5.17) communicates with the SAM module (*Steuerungs- und Auslese-Modul*, i.e. the control and readout module) and the readout controller (ROC) modules of the MDC system. Both interfaces are similar. They provide a 4 bit wide data bus (S-BUS and D-BUS plus several control signals (busy, error, acknowledge and *data strobe*). The data is set on the S- and D-Bus sequentially, first the trigger code, then the lower half of the trigger tag (from 3 to 0) and last the upper half of the trigger tag (from 7 to 4). After each word is set, the *data strobe* signal is asserted for one clock cycle.

On the S-Bus, connected to the SAM controller, only LVL2 data is transported. The D-Bus, connected to the ROC controllers, is shared by the LVL1 and the LVL2 triggers. Therefore it is necessary to multiplex the two levels of the trigger.

Due to electronic noise in the communication lines during the readout of the MDC detector, it is not desirable to perform any LVL2 processing while reading out the detector.

To overcome these two requisites in the communication with the MDC system, LVL1 and LVL2 are not send independently but rather in a coupled

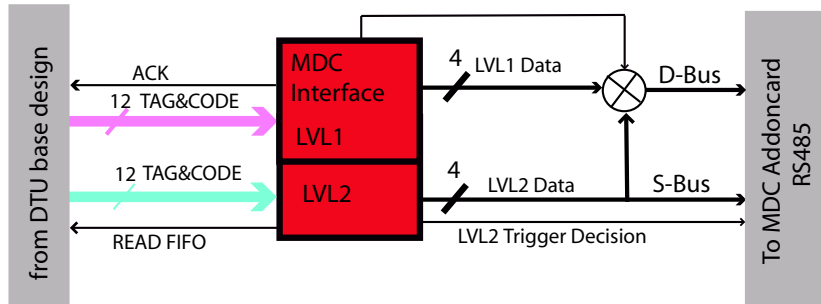


**Figure 5.17:** Diagram of the communication DTU–MDC system.

way. LVL1 data needs priority. Hence, whenever a LVL1 trigger arrives, the data is sent to the detector. LVL2 data is kept on hold in the FIFO. There they wait until a LVL1 arrives and is sent. After that, the DTU keeps the LVL1 BUSY high on the triggerbus (this way it ensures that no further LVL1 triggers may arrive) and sends the LVL2 data in the FIFO.

## 5.4 Trigger Performance

During the beam time which took place between October and November 2002 (C+C with Beam Kinetic Energy = 2AGeV), the HADES’s second level trigger was fully operational for the first time. As this was the first full system test and, as the multiplicity of C+C reactions is much lower than the one of Au+Au for which it was designed, trigger settings were not applied to the maximum of its reduction possibilities. Cuts in invariant mass or opening angle of the pair would alter the physics of the enhanced sample. As this was a testing experiment, such an online physical selection can only be applied after thorough studies of the efficiency of the trigger system, i.e. comparison with *unbiased* data<sup>1</sup> and *well known* particle yields (for instance  $\eta$ -Dalitz). On the other hand, due to the low multiplicity of C+C, the HADES’s data acquisition system is able to store in the order of 20% of the total LVL1 triggered data, thus an event reduction in the order of 1:100 is not mandatory. All in all, the operation conditions of the HADES data acquisition and trigger system for November 2002 were as follows:

- Maximum event LVL1 rate accepted by the DAQ system : 20 KHz.

<sup>1</sup>unbiased data is data after LVL1 or multiplicity trigger, i.e. there is a selection on the centrality of the reaction already done

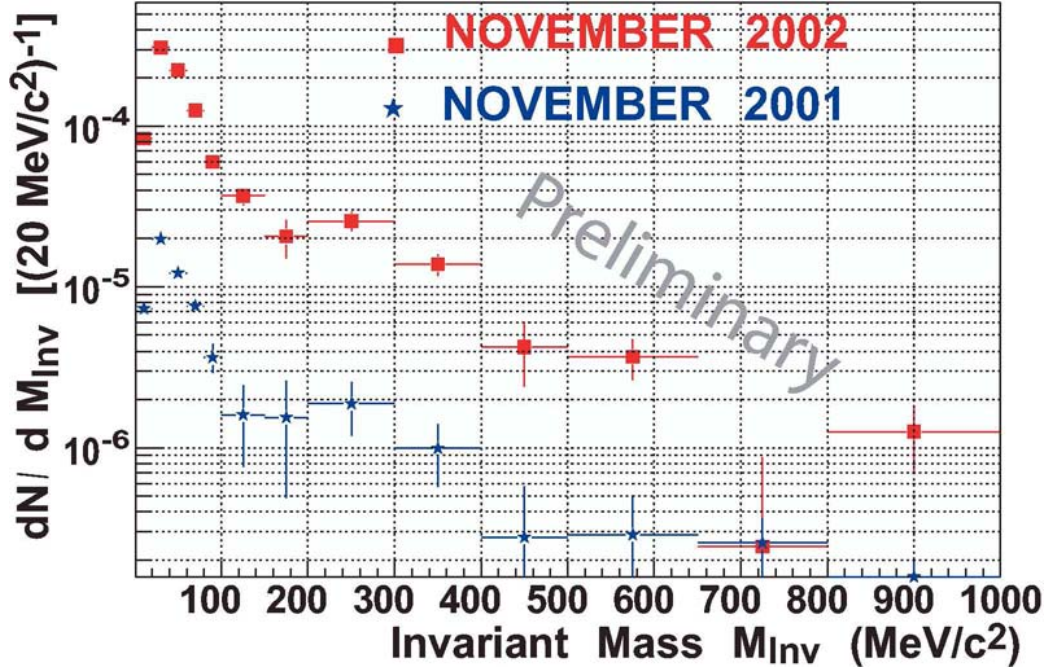


**Figure 5.18:** Comparison of the  $e^+e^-$  pair probability per event for LVL2 triggered data (red squares) and untriggered data (blue stars), both normalized to the same number of LVL1 triggers. It is apparent that by using the LVL2 trigger the lepton content of the sample is enhanced by an order of magnitude [Toi04].

- LVL2 Trigger Conditions:

- RICH thresholds (ring, veto) : (8,3). This means more than 8 pads fired in the ring region and less than 3 pads in the veto region (fig. 5.5).
- Pre-Shower : *local maximum search* only (i.e. no cluster search).
- TOF : Selection of particle with  $\text{ToF} < 20$  ns.
- M.U. : not cut in  $\Delta\theta$ ,  
 $\Delta\varphi < 8^\circ + \frac{\varphi_{\text{Rich}}}{4}$  (see figure 5.10).

- Enhancement: Relative to LVL1 triggered data

1 Lepton	7.5
Dilepton (opening angle $> 4^\circ$ )	10
Dilepton (opening angle $> 8^\circ$ )	11.

This altogether led to a total event reduction of 1:12 [Toi04]. A comparison of the dielectron pair multiplicity, normalized to the same number of level 1 triggers, in the beamtimes of November 2001 and November 2001 is shown in figure 5.18. During the November 2002 beam time 242 million events were collected. 55% of them, 135 millions, were downscaled LVL1 triggered events and 44%, 106 millions, were positively selected by the LVL2 trigger.



## Part III

# Analysis of Elementary Reactions with HADES



# Chapter 6

## The Analysis Software Framework

Besides the ability of the detectors to quickly react and produce an electric signal whenever there is a particle passing through (i.e. *to detect*), analog signals still need to be digitised and stored into some media in any convenient format (DAQ). This data are then process by some means to obtain the relevant physical variables (momentum, velocity...) of the primary particles.

### 6.1 Data Flow

Data in HADES travel several stages before it is possible to yield any physics result. These stages can be synthesise on three major items:

1. Data Acquisition (DAQ): Experiment or Simulation
2. Event Reconstruction
3. Physics Analysis

The data sources are the electric or light pulses produced in each subdetector whenever a particle crosses through their active part.

#### Data Acquisition

The Data Acquisition System can be defined as the ensemble of hardware and software tools needed to read out, digitise, transport and combine the initial analog information from every subdetector into a digital portion of data ready to store into any convenient medium (typically a tape or a hard disk). This portion of data is called *Event*. The data at this level is known as *Raw Data*. Raw because every event is just a compilation of the raw digital information as it comes out from the analog-to-digital converters (ADC) plus

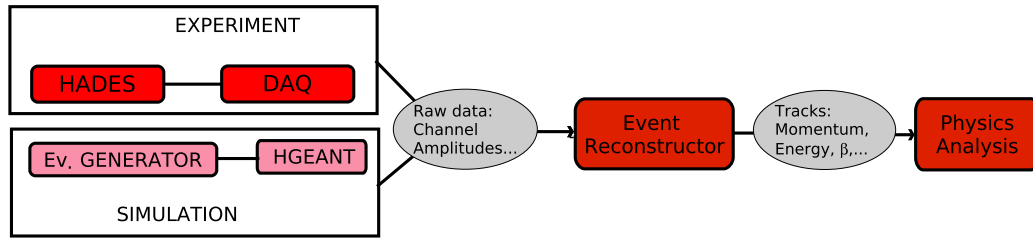


**Figure 6.1:** Schematic view of the HADES data flow.

some header information with the address of the detector which did produce them.

### Simulations

The source of every simulation is the event generator. The event generator simulates the reaction itself, i.e. given some initial conditions, like beam energy and composition, it yields the information on what kind of particles with which energy-momentum are produced. In HADES we use either simple generators based on thermal models like PLUTO [Kag05] or some more complex generators based on quantum transport models like UrQMD [Bas98] or HSD [Cas99].

The detector itself is simulated by the HGEANT [Hol05] package. HGEANT is the HADES simulation package based on GEANT3 [Gea]. It has information about the geometry of the detector as well as about the different materials they are made of. The GEANT3 package simulates the interaction of particles with matter and calculates the energy deposited in any material. With this information, and knowing the detector characteristics, it is possible to estimate the height and shape of the signals in the detectors. Simulated data produced are digitised and stored in a format similar to the experimental raw data level. From this point on, both simulated and experimental events will follow the same data path and will be process in the same way, with the clear exception that the simulated data will carry always a tag with the simulated information.

## 6.2 The Event Reconstruction Framework

HYDRA (the HADES sYstem for Data Reduction and Analysis) [Sán03] is the HADES software framework for simulation and analysis.

### 6.2.1 Overview

The main responsibility of HYDRA is to reconstruct events out of the HADES experimental or simulated raw data and calculate the kinematic variables necessary for further high level physics analysis.

More in detail, the HADES software framework is a collection of rules, interfaces and services put at disposal of the programmers who can extend it to perform a set of tasks. The actual implementation is written in C++ and some its main characteristics are:

1. Use of Object Oriented Programming.  
This programming paradigm allows the implementation of complex algorithms in a solid way. Specially when the development is performed by a dispersed group of people. The programming language is C++, and the compiler chosen is g++ [gcc06].
2. ROOT [Bru06] is used as a class library:  
The ROOT framework provides all the standard functionality necessary for analysis of physics experiments. It is widely spread among the physics community and it is freely available for almost any computer architecture. ROOT provides a well established user interface, a structured Input/Output system, graphics and histograming capabilities and a documentation generation system.
3. Graphic Notation: UML.  
The use of a standard graphic notation for class diagrams simplifies the software development and transfer of information in a large collaboration.
4. CVS is used as a version control system.
5. Parameter Control: Oracle, ROOT files, ASCII files.  
To keep track of the different conditions of the different runs (thresholds applied, voltages in the detectors...), all parameters are stored in an Oracle database. The possibility to use normal files, either plain text (ASCII) or a ROOT file is foreseen for local copies or debugging purposes.

The source of data for the event reconstructor, HYDRA, is the HADES raw data. They can come either from the experiment DAQ system or from simulations. Eventually, partially reconstructed events can be fed back into HYDRA for further processing. Once the data are read, several reconstruction procedures have to be run. They can be grouped in three major levels;

pattern recognition at subdetector level, tracking and, particle identification and high level analysis.

### Pattern Recognition

Raw data is just a collection of channel numbers and ADC counts coming from the different subsystems. These data need to be calibrated prior to perform any analysis on them. Each detector group is in charge of providing the necessary parameters to be able to reconstruct the values of the amplitude, deposited charge, time and positions of the signals.

In a later stage, pattern recognition algorithms are applied to the data to find signatures of particle detections. At this stage the reader should be aware that an electric signal in one or more read-out modules does not imply always the actual detection of any particle. Electronic noise on the read-out and trigger modules play an important role here. At this level of the reconstruction, one has to be sure that the signal matches what is expected from actual particles. For instance, in the RICH detector (section 4.2.3), only electrons or positrons should produce a cone of Cherenkov light that will be detected as a circle of a well defined radius. Hence, the combination of signals which fulfil the *ring* condition, will be declared as a detection or a *hit*. After this level of reconstruction, data are known as *hit level data*.

### Tracking

Tracking is the procedure of fitting the trajectory of a particle through HADES based on the information provided by each subdetector. Once the trajectory is known, and hence the path length, from the measured time of flight, the velocity can be calculated. Also, the tracking procedure, from the deflection obtained in the known magnetic field provides a reconstruction of the initial momentum of the particle. The data level where all the physical relevant variables (momentum, mass, velocity, path length, time of flight,  $dE/dx...$ ) are reconstructed is called *Data Summary Tape* or, in short, *dst*.

The tracking algorithm used to calculate the momentum in January 2004 was based on the Runge-Kutta formalism [Myr79, Koe06]. This consist basically in the numerical calculation of the differential equations of motion in an inhomogeneous magnetic field along the track path.

### Particle Identification

Particle identification is the matching of fitted tracks to known particle species. This is performed comparing the kinematics and detector response

of the tracks with what is expected from known particles. This includes comparing the experimental momentum–velocity distributions with what it is expected from

$$P = \gamma m \beta$$

or checking properties like energy deposited and Cherenkov radiation.

### High Level Physics Analysis

After all kinematic properties of the tracks have been calculated and track have been assigned to particles, further analyses can be performed to address certain physics topics. In the context of this thesis, the physics analysis includes the identification of the  $\eta$  resonance out of events containing four charge particles in their final state (chapter 8).

Event though in the original conception, high level physics analysis was not considered as a goal of HYDRA [Sán03], the HYDRA framework has proved itself as a powerful and flexible tool. This leads to the fact that many parts of the high level physics analysis are being performed now inside the framework.

#### 6.2.2 The HYDRA Structure

The HADES event reconstruction framework, HYDRA, is realised in five sets of classes [Sán03]:

1. Fundamental Class: `HADES`.
2. Classes to contain data:  
`HEvent` and `HCategory`
3. Manage I/O: `HDataSource`
4. Contain and Manage Parameters: `HRuntimeDB`
5. Classes to perform tasks: `HTask`

#### The HADES class

HADES is fundamental class of HYDRA. It encapsulates the whole reconstruction program and provides the methods to control the different tasks. This includes methods to set the input and output, or methods to launch the reconstruction program itself.

### Classes to contain data

The basic data structure in HYDRA is the event. An event holds all the information collected by the different detectors in reaction. In any stage of the reconstruction procedure, the event may also contain the data reconstructed up to this point. There can be several kinds of event. They are basically real, simulated and calibration events.

An event is represented by an `HEvent` object. The `HEvent` is an abstract class, this enforces to inherit other classes to contain the actual events. These are the classes to hold the actual kind of events.

Inside a `HEvent` data are organised in the so called *categories*. A category is any set of data of the same kind. Categories hold the actual data containers, objects which inherit from the `HDataObject` class. The `HDataObject` provides the method needed to access the data via array of indexes as if they were in a matrix .

### Classes to manage Input/Output data

Due to the requirement of HYDRA to have access to any kind of data source, the input/output capabilities are realised by an Abstract Base Class, the `HDataSource`. This class provides only the definition of the interface that the actual classes have to follow. Inherited classes may provide the actual implementation for any kind of data source. From the `HADES` point of view the access to the data is independent of the specific kind of data.

### Classes to manage parameters

A large number of numerical parameter are needed in order to event reconstruction. These are related typically to the calibration and geometry and position of the detectors. They may change in time (even in the same beam-time they may change from file to file), hence a version control of the parameter is needed. This is realised by the runtime database class, `HRuntimeDb` and the `HParIo` class. The `HParIo` class manages the parameter sources. They can be either a ROOT file, a plain text (ASCII) file or a query to the ORACLE database. The `HRuntimeDb` is responsible of the version management. It provides methods to get/add parameter to the database as well as to update the database.

### Classes to perform tasks

In each event a certain number of tasks or actions need to be performed. This is represented by `HTask` objects. The `HTask` class is an abstract class

which provides only a generic interface. `HReconstructor` and `HTaskSet` are two subclasses of `HTask`.

`HReconstructor` is a task dedicated to perform reconstruction algorithms. An ensemble of several tasks can be grouped together into a `HTaskSet` object.



# Chapter 7

## The Event Hypothesis

In elementary reactions (proton-proton or  $\pi$ -proton), due to their low multiplicity, it is possible to detect all or all minus one of the produced particles. Thus, knowing the incoming energy and momentum, the kinematics of the produced tracks are strongly constraint.

### 7.1 Overview

The Event Hypothesis Framework is a software tool developed to aid in the analysis of kinematically complete elementary reactions. It utilises the combined information of all detected tracks to produce particle identification. The use of the coupled information of all detected tracks to do the identification lead to a more efficient and accurate particle identification. For example, as will be shown in the chapter 8, the wrong assignation of particles species in the reaction  $pp \rightarrow pp\pi^+\pi^-X$  leads to an invariant mass of the resultant particles being larger than the incoming invariant mass in a large fraction of the events.

Moreover, the kinematic constrains of an complete reaction can be used to refit the tracks of an event altogether. So, instead of minimising the  $\chi^2$  of the fit of a single track, it is possible to perform a minimisation of all the tracks. On the analysis of the  $\eta$  production (chap. 8), the tracks are refitted and their momenta recalculated based on the assumption that there is a  $\pi^0$  missing (the reaction studied is  $pp \rightarrow pp\pi^+\pi^-\pi^0$ , thus the total missing mass should be equal to the mass of the  $\pi^0$  meson [Rus06]).

## 7.2 Software Structure

The Event Hypothesis framework is arranged as a series of tasks embedded into the HYDRA framework. The method works in a hierarchical way following a tree-like structure (fig. 7.1). It establishes a coherent and unified way to hold different analysis algorithms, by providing a clear interface between the algorithms; the class HHypList.

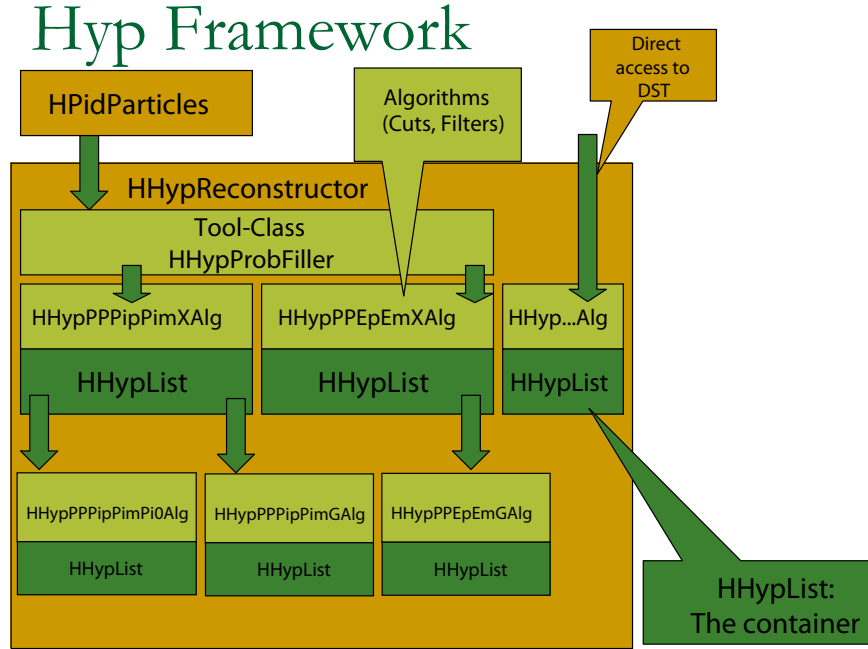


**Figure 7.1:** Structure of the Event hypothesis Framework for the analysis of elementary reactions with HADES [Frö05].

Each algorithm reads one list, performs the algorithm itself (this includes typically a selection of data and/or the calculation of some parameter interesting for a future selection.) and writes a new list.

The first algorithm will normally read directly from a dst file and perform a selection of events with the multiplicity and polarities of the reaction object of study. In the specific case of the reactions interesting for this thesis:

$$pp \rightarrow pp\eta \rightarrow pp\pi^-\pi^+\pi^0$$

and

$$pp \rightarrow pp\eta \rightarrow pp\pi^-\pi^+\gamma,$$

this will imply the selection of all events which fulfil the condition of having four charge particles (HADES can detect only charged particles) with polarities: “+ + + -”.

From the selected events, three combinations of particle identification are generated. Each combination assumes a different particle identity hypothesis as it is shown in the figure 7.2.

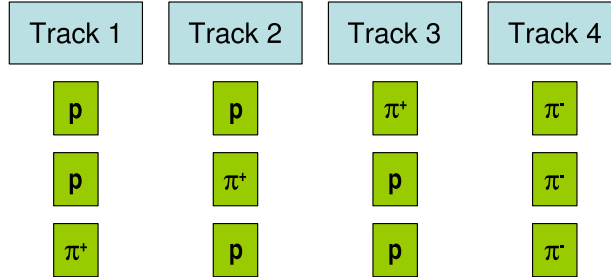


**Figure 7.2:** Example of combinations for the reaction target  $pp \rightarrow pp\eta \rightarrow pp\pi^+\pi^-\pi^0$ . The four charged particles are tracked, therefore the number of combinations is three.

Each hypothesis is assigned a probability. This is an estimation calculated by the algorithms applied and will be based on the kinematic properties of the tracks.

As already mentioned, algorithms read from a “hhyplist”, perform some calculation and write a new “hhyplist”. The calculation itself would involve typically one or more of the different items:

- Calculate and set the probability.  
For example, the standard particle identification method for hadrons is based on the comparison of the momentum- $\beta$  distribution with the theoretical curves for the different species. From the distance of one of the tracks to the theoretical curves we can estimate a probability for the track to be one or another particle. The product of all four individual probabilities will yield the probability for the hypothesis.
- Calculate some kinematic value.  
Values like missing mass of the four particles or the invariant mass of the two pions are very interesting for further analysis and selection of specific reactions. These values are used very often so it is very convenient to calculate them once and store them with the hypothesis.
- Perform a selection of hypotheses.  
Wrong hypotheses lead normally to unrealistic values in some variables and/or to low probabilities. To obtain a cleaner sample (free of misidentified hypotheses) or to select interesting channels, hypotheses

with a low probability or those which do not fulfil certain kinematic conditions can be discarded.

The event hypothesis framework provides a general development framework for the analysis of elementary reaction.

By applying some basic selection filters to the data (multiplicity) and calculating some general physical quantities it reduces the amount of event actually needed to perform any high level analysis and reduces as well the number of calculations needed by the final developers.

### 7.3 The “Delta TOF” Algorithm

Inside the event hypothesis framework and as part of this thesis, the “delta TOF” algorithm has been developed as a method to calculate the start time and perform particle identification in elementary reactions.

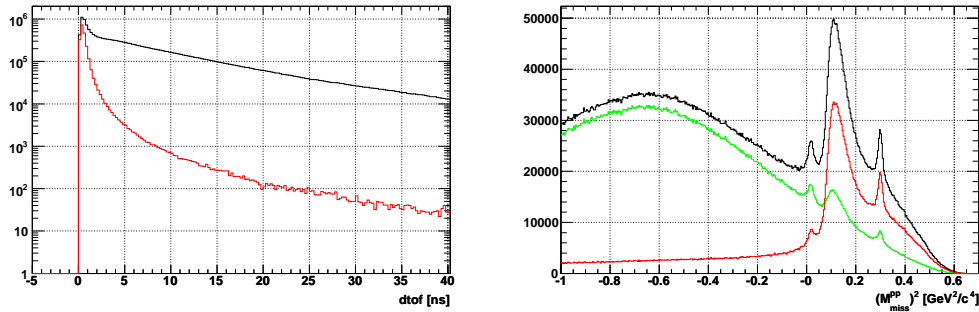
During the beam time of January 2004 there was no detector providing a start time for the data taking. Diamond detectors (START/VETO) can not be used under proton beams, because the energy loss inside the detector material is so small that it does not produce a useful signal. Therefore for the proton experiment it was decided to use a pair of hodoscope detectors, made of scintillating rods. Each hodoscope is constituted by 16 rods of Bicron BC408, each one 1 cm wide and 12 cm long. Each rod is read out on both ends by photomultipliers. For technical reasons, the scintillator hodoscopes were not ready for production use during the January 2004 run.

In absence of any start signal, all detectors did use the time of the first particle arriving as time zero for their measurements. This was specially critic for the MDC system. Where the absence of a proper start time lead to bad determination of the drift time and therefore bad determination of the hit positions.

Also, without an absolute time reference the calculation of the velocity and all the derived quantities becomes not straight forward. Hence, particle identification cannot be performed via the comparison of the *time-of-flight versus momentum* ideal curves for the different known species with the measured data.

To overcome this problem two methods to calculate the total time of flight of the particles have been proposed inside the collaboration.

The first method uses fastest negative track as a reference. If the track produced a ring in the RICH detector is assumed to be an electron or otherwise to be a  $\pi^-$ . With the information of the mass from the previous assumption



(a) Delta TOF distribution for all combinations (black) and  $pp\pi^+\pi^-$  events (red). The Y axis is in logarithm scale. The distribution of properly identified combinations peaks sharply towards Delta TOF equals zero.

(b) Effect of a selection of combinations with Delta TOF smaller than 1 ns on the proton-proton missing mass distribution. In black, all combinations; red, combinations with  $\Delta TOF < 1 ns$  and green, combinations with  $\Delta TOF > 1 ns$ .

**Figure 7.3:** The Delta TOF method. The identity selection power is apparent. Simulated events proton-proton at 2.2 GeV kinetic energy.

plus the path length and momentum obtained by the deflection of the track in the magnetic field (the determination of the momentum has a bad resolution due to the lack of proper drift time information), velocity and time of flight can be calculated [Spa05b].

In addition after the start time has been recalculated, it is still necessary to perform particle identification of the positive tracks.

The “Delta TOF” is a method which yields time of flight and produces particle identification in exclusive reactions. This method was developed inside the Event Hypothesis framework, and it is based on the comparison of the time differences measured in the time of flight wall with what would be expected from each hypothesis. As it was mentioned already, even though there is not a proper start time measurement, low resolution tracking can still be performed. Thus, momentum and path length for each particle can be obtained. With this data plus the mass of our hypothesis, it is possible to calculate the expected time of flight for each particle,  $t_i^{theo}$ .

Experimentally, the times measured,  $t_i^{exp}$ , are not the total time of flight of each track due to the lack of the start detector. Nevertheless, time differences between any two tracks has been correctly measured.

In the case of an hypothesis with a correct particle identity, the value of the difference of time differences between the first and  $i$ th track,  $\Delta t_{1,i}$ , calculated

as

$$\Delta t_{1,i} = (t_1^{exp} - t_i^{exp}) - (t_1^{theo} - t_i^{theo}), \quad (7.1)$$

should be compatible with zero inside the detector resolution.

The sum of all differences

$$\Delta t = \sum_{i=2}^N |\Delta t_{1,i}| \quad (7.2)$$

can be used as a parameter to select good hypothesis.

On the figure 7.3, left, we can see simulations of the distribution of  $\Delta t$  of all hypothesis (black) and of hypothesis with the correct hypothesis (red). It is apparent how the  $\Delta t$  parameter peaks strongly at zero (note the logarithm scale on the vertical axis).

# Chapter 8

## Exclusive Reconstruction of the $\eta$ Meson

### 8.1 Introduction

The Dalitz decays of the  $\pi^0$  and  $\eta$  mesons, i.e.  $\pi^0 \rightarrow e^+e^-\gamma$  and  $\eta \rightarrow e^+e^-\gamma$ , are the main contributions to the dielectron spectrum in the invariant mass region below  $500 \text{ MeV}/c^2$ . Therefore, for understanding the the HADES heavy ion  $e^+e^-$  spectrum, it is of major importance to accurately know the production mechanisms and the decays of these mesons.

The HADES spectrometer offers a few important advantages:

1. The comparison of the production in pp and AA collisions, and
2. the comparison of electromagnetic and hadronic decay channels,

can be both performed in the same detector and with the same systematic errors.

In particular, the pp reaction offers a final state with only a few particles, thus a clean environment for reconstruction.

In order to provide kinematic constraints in the 5-particle final state, for this work an exclusive <sup>1</sup> reconstruction has been chosen. HADES is specially well suited for exclusive measurements due to its large acceptance.

In chapter 5, the trigger system as well as its importance to select interesting physics channels in heavy ion reaction has been discussed. There, it has been

---

<sup>1</sup>In an exclusive reconstruction the kinematics of a n-particle final state is fully constrained. This can be achieved by the measurement of n-1 particles.

already mentioned the necessity of a reference reaction to obtain an overall normalization and efficiency of the dilepton trigger.

The following chapter will present a study of the  $\eta$  production in proton-proton collisions and its decay into hadronic final states. Complementary, the reconstruction of electromagnetic decay channels is given in references [Spa05a, Rus06, Spr06].

The channels reconstructed were the two dominant charged decay modes of the  $\eta$  meson:

$$\eta \rightarrow \pi^+\pi^-\pi^0 \text{ (dominant charged decay mode, b.r. 22.6\% [Eid04])}$$

$$\eta \rightarrow \pi^+\pi^-\gamma \text{ (b.r. 4.68\% [Eid04]).}$$

The analysis has been done inside the Hydra and Event Hypothesis frameworks introduced in the previous chapters.

The analysis strategy to identify the interesting channels is based on the missing mass technique. The neutral  $\pi^0$  and  $\gamma$  will be identified from the missing mass between the initial and final states of the reaction.

## 8.2 Reaction Overview

In January of 2004, HADES has recorded 300 millions proton-proton events. The reactions were produced by a proton beam of 2.2 GeV kinetic energy colliding against a fixed target of protons (liquid Hydrogen, LH<sub>2</sub>. Technical details about the target can be read in section 4.2.1). The total available energy in the centre of mass was  $\sqrt{s} = 2.765$  GeV. The  $\eta$  production threshold is  $\sqrt{s}_{th} = 2.425$  GeV. Therefore, the energy excess over the  $\eta$  production threshold was 339 MeV.

The relevant kinematic values of the reaction are displayed on the table 8.1.

January 2004 Beamtime : February 6 <sup>th</sup> – 18 <sup>th</sup> , 2004		
Beam	Protons	$E_{kin} = 2.2$ GeV $P = 2.995$ GeV
Target	Protons	Liquid $H_2$
Energy (c.m.)		$\sqrt{s} = 2.765$ GeV

**Table 8.1:** Characteristics of the reaction.

The total number of events recorded during the January 2004 run is 302 millions. From these, a subset of 7.5 millions events with four tracks, three positive and one negative, were considered for this analysis.

The HADES spectrometer is able to track charged particles but neutral particles are not detected. In the following, for the exclusive reconstruction of the  $\eta$  meson, we assume that all the charged particles produced in the reaction are detected, i.e. we detect the two protons and the two pions.

For every event considered three combinations with different hypothesis on the identity of the tracks were generated as follows:

Track 1 (+)	Track 1 (+)	Track 3 (+)	Track 4 (-)
$\pi^+$	p	p	$\pi^-$
p	$\pi^+$	p	$\pi^-$
p	p	$\pi^+$	$\pi^-$

The total number of combinations is 22.5 millions.

The neutral  $\pi^0$  and  $\gamma$  will be identified from the missing mass between the initial and final state of the reaction (eq. 8.1).

The initial conditions are fixed by the beam and target characteristics.

$$E_{in} = \sqrt{m_{proton}^2 + P_{beam}^2} + m_{proton}$$

$$\vec{P}_{in} = \vec{P}_{beam}$$

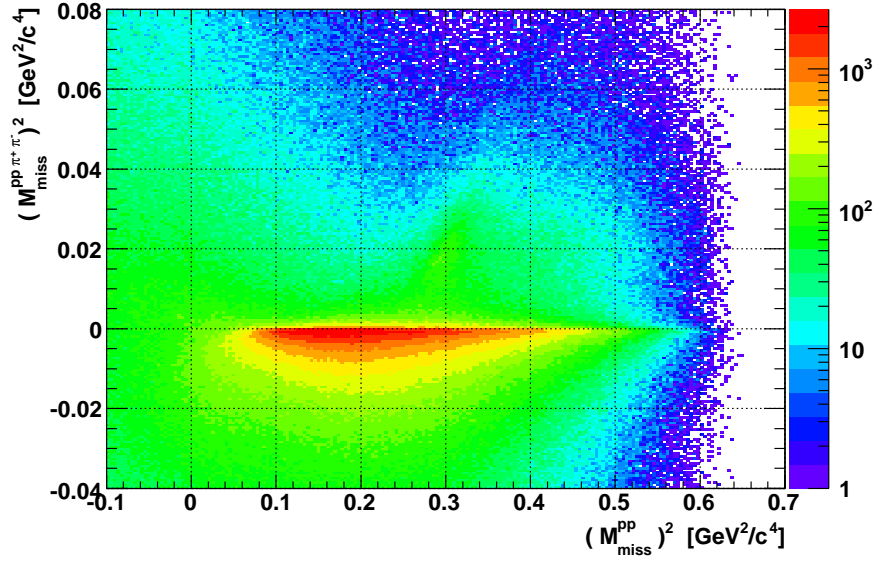
The final state momenta and energies are obtained from the tracking of the particles in the spectrometer. For each combination, masses are assigned following the identities of the hypotheses.

The square of the mass difference between the beam plus target and the four detected particles (eq. 8.1, in the following  $(M_{miss}^{pp\pi^+\pi^-})^2$ ); the square of the mass difference between beam plus target and the two outgoing protons (eq. 8.1),  $(M_{miss}^{pp})^2$ ; as well as the invariant mass squared of the two pions (eq. 8.2),  $(M_{inv}^{\pi^+\pi^-})^2$ , have been calculated, for all combinations.

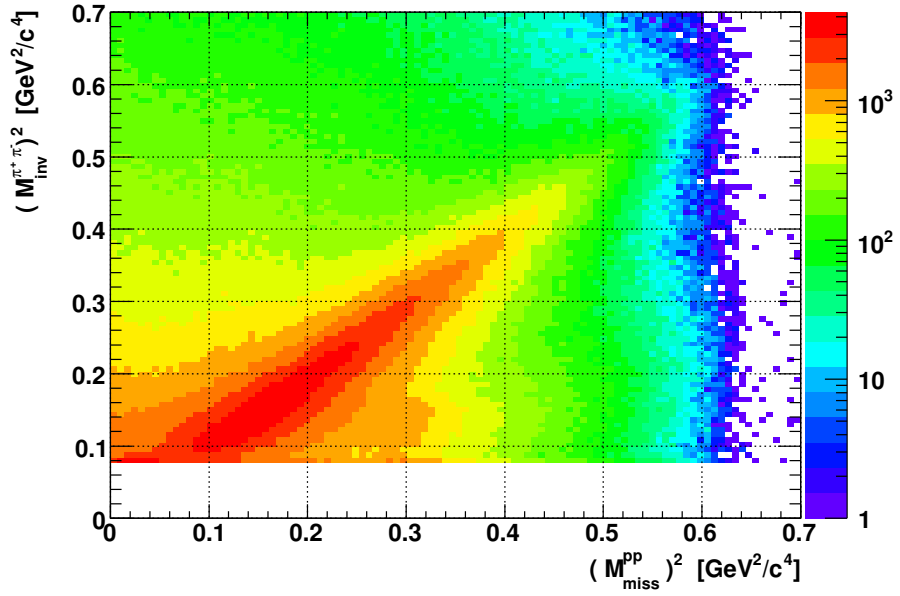
$$M_{miss}^2 = \left( E_{in} - \sum_i E_{out}^i \right)^2 - \left( \vec{P}_{in} - \sum_i \vec{P}_{out}^i \right)^2 \quad (8.1)$$

$$M_{inv}^2 = (E_1 - E_2)^2 - (\vec{P}_1 - \vec{P}_2)^2 \quad (8.2)$$

The distributions of  $(M_{miss}^{pp})^2$  versus  $(M_{miss}^{pp\pi^+\pi^-})^2$  and  $(M_{miss}^{pp\pi^+\pi^-})^2$  versus  $(M_{inv}^{\pi^+\pi^-})^2$  of all combinations are shown in the figure 8.1.



(a)  $(M_{miss}^{pp})^2$  vs.  $(M_{miss}^{pp\pi^+\pi^-})^2$



(b)  $(M_{miss}^{pp})^2$  vs.  $(M_{inv}^{\pi^+\pi^-})^2$ .

**Figure 8.1:** Two dimensional plots generated from all the combinations before any selection criteria were applied.

### 8.3 Reconstruction of the $\eta \rightarrow \pi^+\pi^-\pi^0$ Channel

In this section it will be shown how the identification of the  $\eta$  decay to three pions has been performed. The complete reaction is given as:

$$pp \rightarrow pp\eta \rightarrow pp\pi^+\pi^-(\pi^0)$$

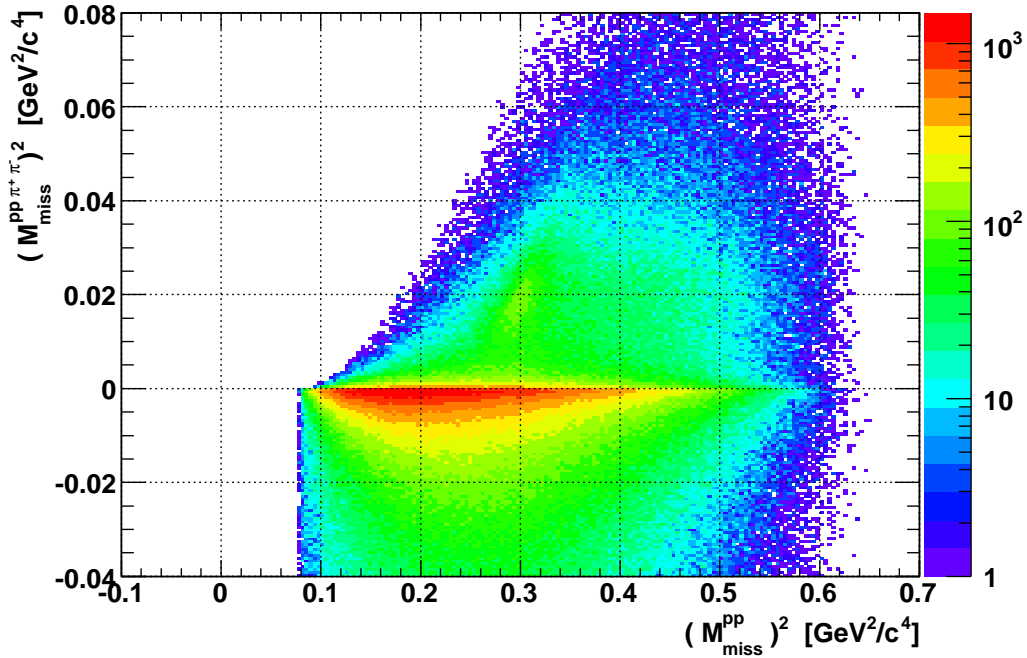


**Figure 8.2:** Effect of the selection of events with  $M_{miss}^{pp} > M_{inv}^{\pi^+\pi^-}$  on the proton-proton missing mass squared vs. 4 particle missing mass squared.

For the events which we are interested in, the two pions are products of the  $\eta$  decay. The  $\eta$  meson decays into three pions, hence the reconstructed invariant mass of the two pions has to be smaller than the  $\eta$  mass. The assumption that only one  $\eta$  has been produced implies that the missing mass of the two protons is equal to  $M_\eta$ . Taking that into account any  $\eta$  decay has to fulfil the condition  $M_{miss}^{pp} > M_{inv}^{\pi^+\pi^-}$ . Figures 8.2 and 8.3 show the result of this selection on the data.

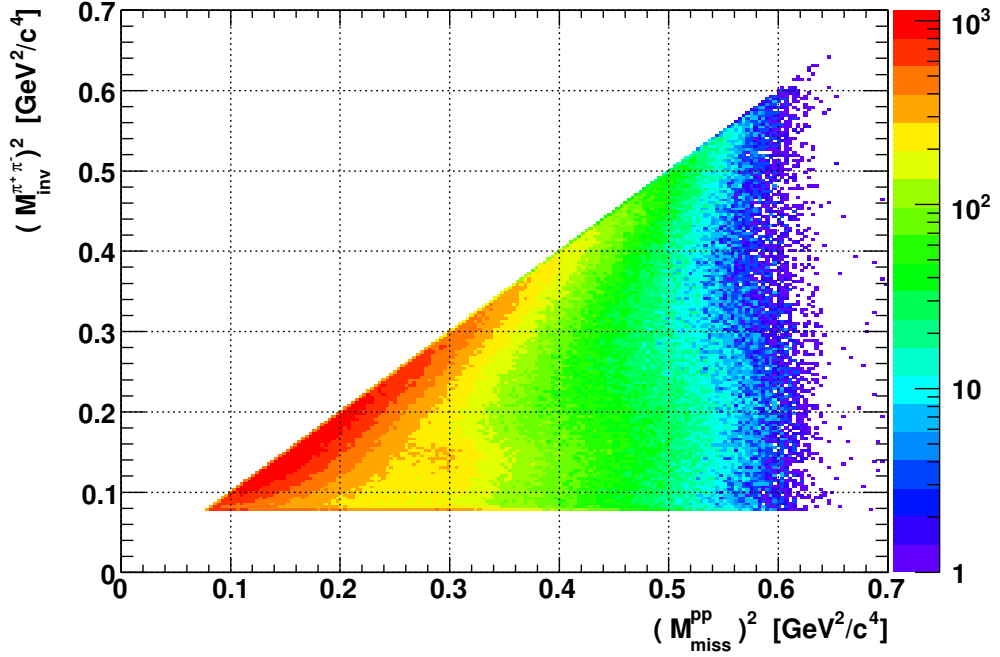


**Figure 8.3:** Effect of the selection  $M_{miss}^{pp} > M_{inv}^{\pi^+\pi^-}$  on the  $\pi\pi$  invariant mass squared versus the missing mass of the two protons proton histogram.

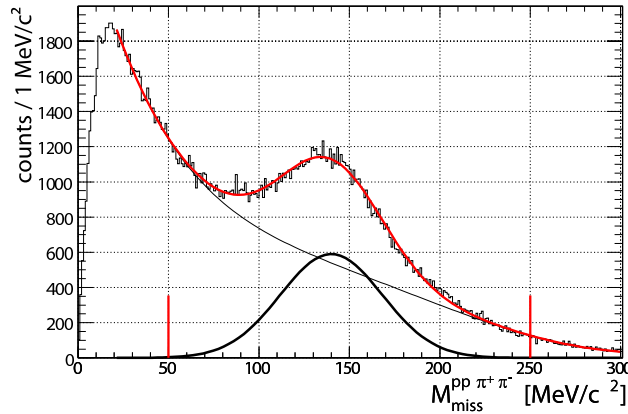
### 8.3.1 Identification of the Missing $\pi^0$ .

The  $M_{miss}^{pp\pi^+\pi^-}$  after the selection of data shown in the previous section is plotted <sup>2</sup> on the histogram of figure 8.4.

The enhancement visible around  $M_{miss}^{pp\pi^+\pi^-} \sim 150 \text{ MeV}/c^2$  corresponds to the events with a missing  $\pi^0$ . The histogram has been fitted using a polynomial of grade four as an estimation for the background plus a Gaussian function for the signal. The results of the fit can be reviewed on the table below the figure 8.4.

**Error discussion.** The statistical errors are relatively small here compared to the systematic errors. The histogram in fig. 8.4 has more than 145.000 entries and, as it can be seen on the figure, bins in the relevant area (around the  $\pi^0$  mass) have in the order of 1,000 entries each. The uncertainties in

<sup>2</sup>Due to technical reasons, like finite detector resolution, internally, energies and masses are always squared. Hence what it is really calculated is  $(M_{miss}^{pp\pi^+\pi^-})^2$ . What it is actually plotted on the figure 8.4 is the  $\sqrt{(M_{miss}^{pp\pi^+\pi^-})^2}$  for all the events with  $(M_{miss}^{pp\pi^+\pi^-})^2 > 0$ .



Signal (50–250 MeV)	$35,000 \pm 3,000$
mean	$138.9 \pm 0.3$ MeV
sigma	$25.9 \pm 0.9$ MeV

**Figure 8.4:** Missing mass of the four outgoing particles under the condition  $M_{miss}^{pp} > M_{inv}^{\pi^+\pi^-}$ . Fit done with a polynomial grade 4 plus a Gaussian function.

the parametrization of the background, lead to significant systematic errors. The function to fit the background was chosen to be a polynomial of grade 4 as:

$$f(x) = a_0x^4 + a_1x^3 + a_2x^2 + a_3x + a_4$$

Other functions have been tested (several polynomials, exponential and Gauss). From all those, the fourth grade polynomial was the one which yields the best value of  $\chi^2/ndf$  and thus the best description of the background shape. The histogram on the figure has been fitted in the range from 21 MeV/c<sup>2</sup> to 300 MeV/c<sup>2</sup>. Several fits have been tested within the range 15 – 35 to 270 – 350 MeV/c<sup>2</sup>. The values of yield, mean and sigma have been calculated as the mean of the values produced by all the fits which have  $\chi^2/ndf < 1.2$ . The  $\pi^0$  yield varies in the range from 33,000 to 38,000. The value given on the table is just the average between minimum and maximum yield:

$$Y = 35,000 \pm 3,000.$$

The signal itself is very well described by a Gauss function. The mean of the Gauss stays between 138.7 MeV/c<sup>2</sup> and 139.2 MeV/c<sup>2</sup> for all different fit ranges, with a sigma between 25.0 MeV/c<sup>2</sup> and 28.6 MeV/c<sup>2</sup> (even using other functions to parametrize the background, the mean and sigma of the

$\pi^0$  signal stays always in this range). Again, the values given for  $M_{\pi^0}$  and  $\sigma$  are just the averages between all minima and maxima.

$$M_{\pi^0} = 138.9 \pm 0.3 \text{ MeV}/c^2.$$

$$\sigma = 25.9 \pm 0.9 \text{ MeV}/c^2.$$

The fact that the  $\pi^0$  signal is so well described, in spite of the uncertainties on the background determination, and that the selection applied is so wide ( $3\sigma$ ), implies that the final  $\eta$  signal will not be affected by this selection while the background is highly suppressed.

### 8.3.2 Identification of $\eta$

After the  $\pi^0$  selection, a kinematic refit is applied to improve the mass and momentum resolution [Rus06]. The nominal  $\pi^0$  mass [Eid04] is used as a constraint in the kinematic refit. This refit is performed imposing the conditions that the missing particle is a  $\pi^0$  and that the four detected tracks are correctly identified as  $pp\pi^+\pi^-$ .

The two proton missing mass distribution of the kinematic fitted events is displayed in figure 8.5. The fifth grade polynomial used to fit the background is shown with a full blue line. The  $\eta$  signal was obtained by subtracting the fitted background from the histogram. The characteristics of the signal are shown in the table 8.2.

$M_{miss}^{pp}$	
Yield	$21,500 \pm 1,000$
S/B	50 %
M	$547.0 \pm 0.3 \text{ MeV}/c^2$
FWHM	$28 \pm 2 \text{ MeV}/c^2$

**Table 8.2:** Characteristics of the  $\eta$  signal of figure 8.5. On the second row, S denotes "signal" and B denotes "background".

The signal is centred at  $M_\eta = 546.7 \pm 0.3 \text{ MeV}/c^2$  and has a width of  $\text{FWHM} = 28 \pm 2 \text{ MeV}/c^2$ .

**Error discussion.** Similar to the previous subsection, the  $M_{miss}^{pp}$  histogram has sufficient entries so that the statistical errors are smaller than 3%. In this case the uncertainties in the parametrization of the background are the main source of error, about 5–10%. A polynomial of grade five has been used

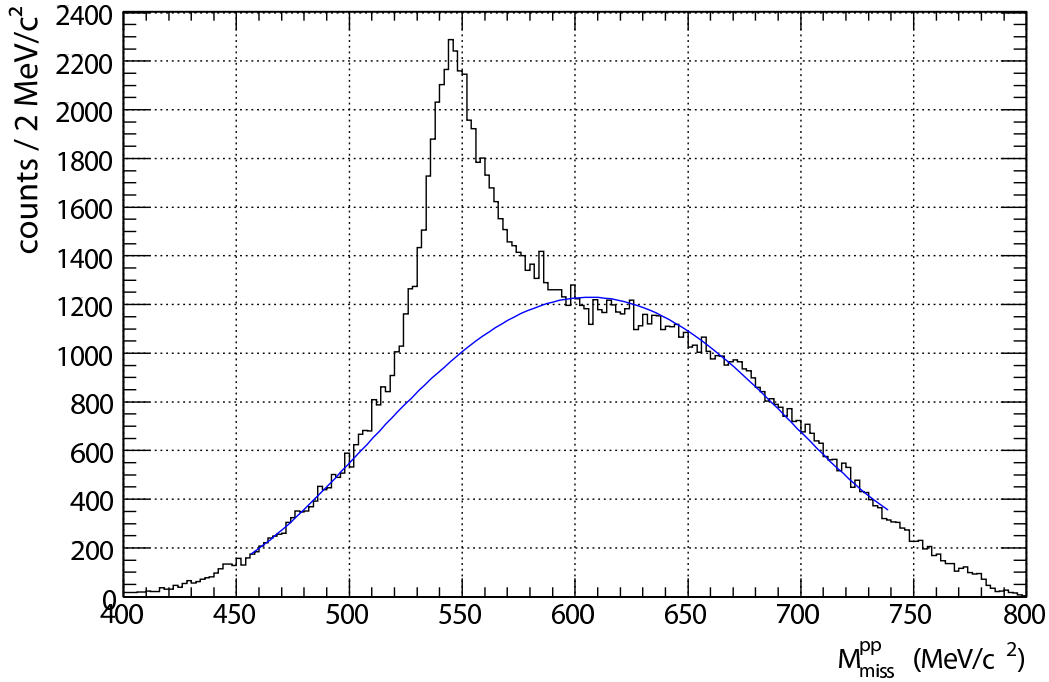


**Figure 8.5:** Final proton proton missing mass histogram after a kinematic refit and the selections explained. The fit was performed with a polynomial grade 5 plus a Gaussian.

because it provides a smooth ad hoc description of the background in a wide range outside the signal region.

The figure 8.5 shows the best fit obtained ( $\chi^2/ndf = 1.7$ ). A series of fits has been tried by modifying systematically the different fitting ranges; with minima between 400 and 470  $\text{MeV}/c^2$ , and maxima between 680 and 800  $\text{MeV}/c^2$ . The final values of table 8.2 are obtained as the average values from all the fits with  $\chi^2/ndf$  smaller than 2. The value of the yield varies between 20,500 and 22,500; thus the average yield has an error of  $\pm 1000$ .

$$Y = 21,500 \pm 1000$$

The values obtained for  $M_\eta$  and FWHM are;

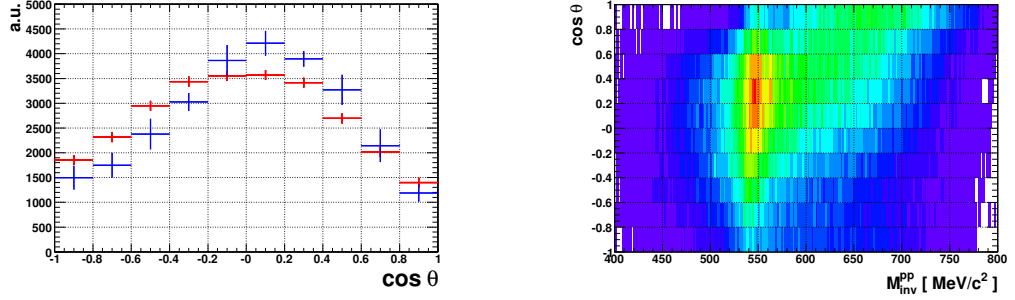
$$M_\eta = 547.0 \pm 0.3 \text{ MeV}/c^2$$

and

$$FWHM = 28 \pm 2 \text{ MeV}/c^2.$$

The mass and the width are consistent with [Eid04] when taking into account the HADES tracking resolution.

### 8.3.3 $\eta$ Angular Distribution.



(a)  $\eta$  emission angle. BLUE: Experimental data. RED: Simulations

(b)  $M_{miss}^{pp}$  versus the cosine of the emission angle.

**Figure 8.6:**  $\eta$  angular distribution.

The distributions of the  $\eta$  emission angle are shown in figure 8.6. The right panel on the figure shows the  $M_{miss}^{pp}$ , on the X axis, versus the cosine of the  $\eta$  emission angle on the Y axis.

The histogram with the  $\eta$  yield as a function of the cosine of the  $\eta$  emission angle in the centre of mass frame is shown on the left panel in figure 8.6. The blue crosses represent the experimental data points.

The errors shown are the sum of the estimated statistical and systematic errors. The latter are derived mainly from the uncertainties in the parametrization of the background as explained in the subsection 8.3.2. The red crosses depict the simulated spectrum normalized to the identical number of entries. For simulations, only statistical errors are shown. Data are not corrected for the acceptance.

The simulations have been performed using only an isotropic model [Sai05a, Prz05]. Thus the simulated  $\eta$  angular distribution correspond to a pure phase space distribution.

The experimental data shown in figure 8.6 (a) show a slight enhancement over the simulations in the region perpendicular to the beam line ( $\cos \theta \sim 0$ ); while in the angular region below  $\cos \theta < -0.2$ , the simulations overestimate the data. This is shown more clearly in figure 8.7, where the ratio of the experimental over the simulated spectrum is drawn. At this stage new simulations, which take into account the latest data on the hadronic  $\eta$  decay [Ams95, Bal04b], would be necessary to compare to our experimental results.

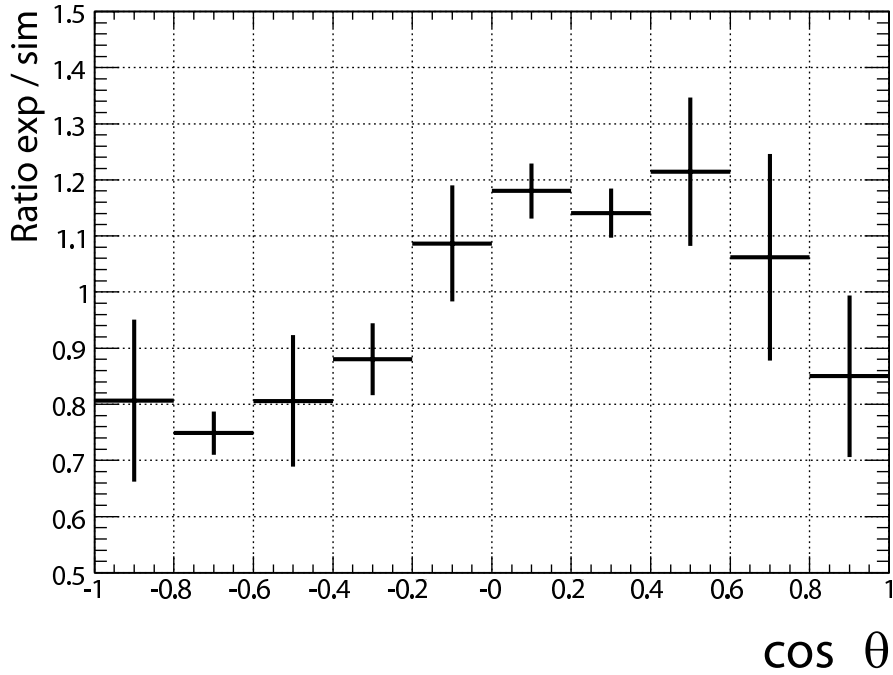


**Figure 8.7:** Ratio of the experimental over the simulated distributions of figure 8.6 (a).

### 8.3.4 Dalitz Plot

The Dalitz plot of the  $pp\eta$  system is shown in figure 8.8. The invariant mass of the low momentum proton and the  $\eta$  is plotted on the X axis. The invariant mass of the second proton, the proton with higher momentum, and the  $\eta$  is shown on the Y axis. This proton does not intervene in the resonance and is therefore also called *spectator* proton. Data are not corrected for the HADES acceptance.

In the region around  $M_{inv}^{p_2\eta} \sim 1.5 \text{ GeV}/c^2$  we can see an enhancement due to the  $N^*(1535)$  resonance.

This has been shown [Bal04b] to dominate the  $\eta$  production in the HADES energy regime.

In the figure, the HADES acceptance cut-off is apparent in the region where the invariant mass of  $p\eta$  is around  $1,770 \text{ MeV}/c^2$ . This has been reasoned to be related with the missing acceptance in the forward direction. The HADES acceptance (The description of the HADES spectrometer can be found in chap. 4) covers from  $8^\circ$  to  $85^\circ$  in the polar direction. The fact that the region from  $0^\circ$  to  $8^\circ$  degrees is not accepted may prevent to detect all four decay particles ( $pp\pi^+\pi^-$ ) of  $\eta$  decay in an important fraction of the

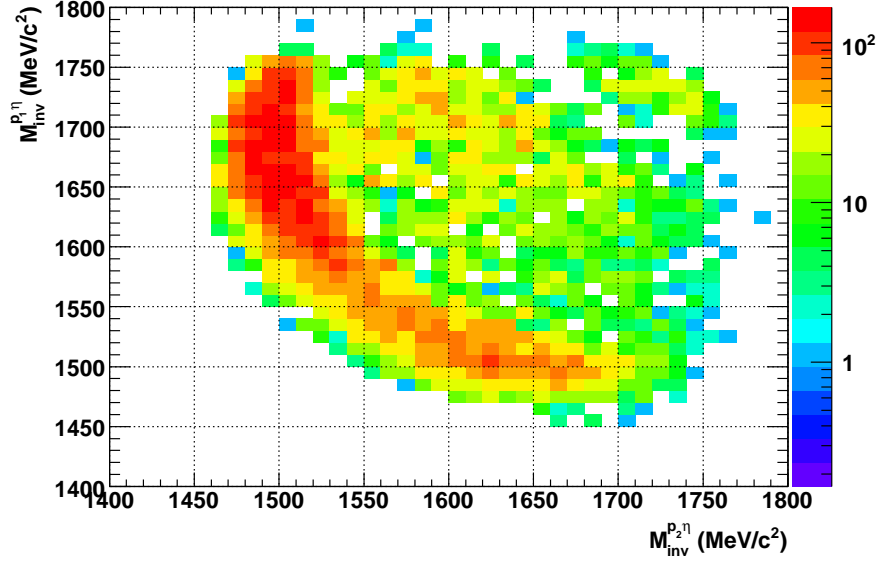


**Figure 8.8:** Dalitz plots of the  $\eta$  decay. On the X axis invariant mass squared distribution of the low momentum proton and  $\eta$ . On the Y axis the same distribution with the high energy proton. The enhancement in the region around  $M_{inv}^{p_2\eta} \sim 1.5$  GeV/c<sup>2</sup> corresponds to the N\*(1535) resonance.

reactions.

## 8.4 Reconstruction of the $\eta \rightarrow \pi^+\pi^-\gamma$ Channel

The dominant contribution to the four particle final state,  $pp\pi^+\pi^-$ , in the HADES energy regime is the direct non resonant  $pp \rightarrow pp\pi^+\pi^-$  without any missing particle. Hence, most of the four track events have a total missing mass compatible with zero. This is shown clearly in figure 8.1 (a). Hence, to identify the reaction  $\eta \rightarrow \pi^+\pi^-\gamma$  in the huge background, we will take into account not only the missing mass but also the missing momentum carried away by the photons.

If the assumption that the two pions of the final channel arise from the decay of an  $\eta$  meson, the calculated two pion invariant mass,  $M_{inv}^{\pi^+\pi^-}$ , can not be greater than the  $M_{miss}^{pp}$ . Hence, a first filtering of the data is performed asking for the condition:

$$\text{Condition 1: } M_{miss}^{pp} > M_{inv}^{\pi^+\pi^-}$$

The results of this selection are shown in figures 8.2 and 8.3.

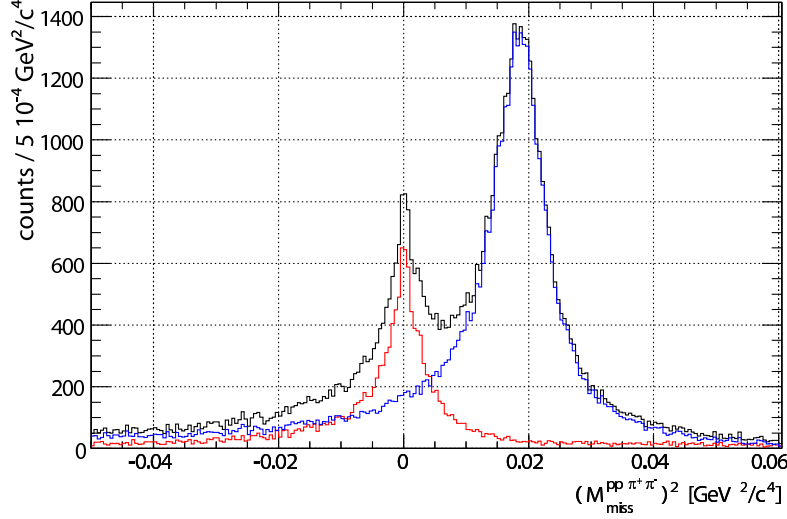


**Figure 8.9:** Four particle missing mass squared for simulated  $\eta$ 's. Black line: all  $\eta$ . Blue: events with  $\eta \rightarrow \pi^+\pi^-\pi^0$ . Red : events with  $\eta \rightarrow \pi^+\pi^-\gamma$ . In the  $\gamma$  region, still around 40% of the events come from the  $\eta$  decay to  $\pi^+\pi^-\pi^0$ .

### 8.4.1 Missing Mass.

Photons have no mass. Nevertheless, due to the finite experimental resolution of the spectrometer, the  $(M_{miss}^{pp\pi^+\pi^-})^2$  of  $\eta$  events is not a delta function centred at 0 but rather a broader distribution (the shape of the distribution of  $(M_{miss}^{pp\pi^+\pi^-})^2$  for simulated  $\eta$  events can be seen on the figure 8.9). On the following, only events which fulfil the condition:

$$\text{Condition 2: } \left| \left( M_{miss}^{pp\pi^+\pi^-} \right)^2 \right| < 7,500 \text{ MeV}^2/\text{c}^4$$

are considered for further analysis.

The value of  $7,500 \text{ MeV}^2/\text{c}^4$  was chosen as a compromise value which minimises the contribution of the  $\eta \rightarrow \pi^+\pi^-\pi^0$  to the signal and reduces highly the background while still most of the signal remains.

From the study of simulated events (fig. 8.9) we find that with this selection 61% of the signal survives and the ratio of  $\eta \rightarrow \pi^+\pi^-\gamma$  over  $\eta \rightarrow \pi^+\pi^-\pi^0$  is enhanced from the 23 to the 62 %. The background is strongly reduced. In the  $3\sigma$  region around the fitted  $\eta$  signal, the background decreases from

557,000 to 202,000 entries.

## 8.4.2 Missing Momentum.

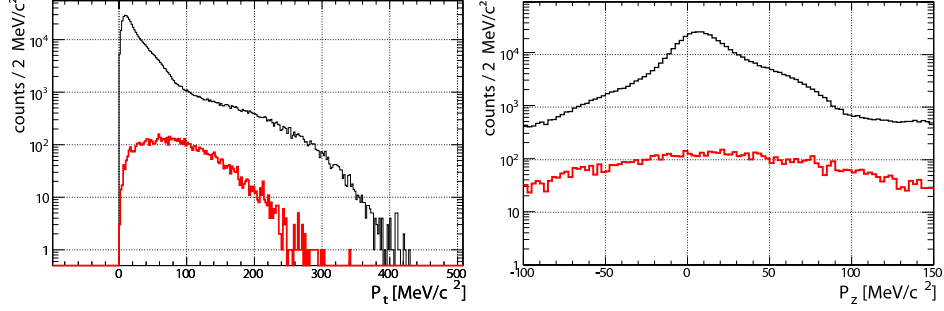


**Figure 8.10:** Comparison of the  $P_t$  (left) and  $P_l$  (right) distributions for all events (black) and events with  $\eta \rightarrow \pi^+ \pi^- \gamma$  (red).

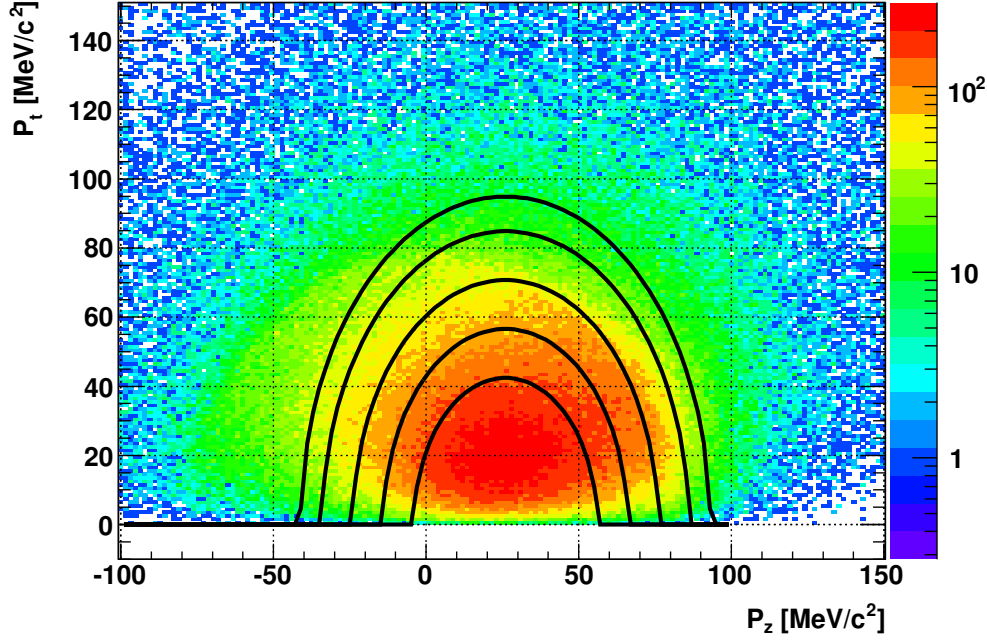
The missing momentum distribution of  $pp\pi^+\pi^-$  events peaks strongly at 0  $\text{MeV}/c$  and decreases exponentially between 0 and 100  $\text{MeV}/c$ . For simulations (see the  $P_t$  and  $P_l$  distributions of simulated  $\eta$ 's in figure 8.10) we observe that in events with an  $\eta$  decay to  $\pi^+\pi^-\gamma$ , most of the photons carry a transversal momentum between 0 and 200  $\text{MeV}/c$  with a most probable value at around 80  $\text{MeV}/c$ .

Figure 8.11 shows the experimental distribution of  $P_t$  vs.  $P_l$  after the selections 1 and 2. The black lines on the picture depict the different filters studied. Events inside the semi-ellipses are removed and from the surviving combinations the two proton missing mass squared histograms are plotted on the figure 8.12.

It is apparent that as the selected  $P_t$ - $P_l$  region moves away from the maximum, the  $\eta$  signal to background ratio increases. Removing the events inside the first ellipses in the fig. 8.11, we obtain a signal to background ratio of 3%. This values increases up to the final 9% that can be obtained with the most restrictive selection (outermost line in fig. 8.11 and lower right panel of fig. 8.12). The final histogram of fig. 8.13 was obtained asking for the condition:

$$\text{Condition 3: } \frac{P_t^2}{2} + (P_l - 26 \text{ MeV}/c)^2 > 3200 \text{ MeV}^2/c^2.$$

The histogram has been fitted using a polynomial of third grade, to estimate the background, plus a Gaussian function for the signal. The  $\eta$  signal is fitted at  $M_\eta^2 = 0.295 \text{ GeV}^2/c^4$  with a width of  $\sigma = 0.018 \text{ GeV}^2/c^4$ .



**Figure 8.11:** Distribution of  $P_t$ - $P_l$  for all the combinations with 4 charged tracks after  $M_{miss}^{pp} > M_{inv}^{\pi^+\pi^-}$  and  $\left| (M_{miss}^{pp\pi^+\pi^-})^2 \right| < 7,500 \text{ MeV}^2/c^4$ .

**Errors.** The unknown systematics in the determination of the background shape are the largest source of error. At least their size can be estimated observing the variations on the fit results by varying the fitting parameters. The histogram of fig. 8.13 was fitted several times with different extremes, i.e. minima from  $0.15$  to  $0.22 \text{ GeV}^2/c^4$  and maxima from  $0.40$  to  $0.50 \text{ GeV}^2/c^4$ . As a result the mean shifted between  $0.30$  and  $0.29 \text{ GeV}^2/c^4$ , and the sigma between  $0.017$  and  $0.020 \text{ GeV}^2/c^4$ . The final results for the calculated mean and sigma were:

$$M_\eta^2 = 0.295 \pm 0.006 \text{ GeV}^2/c^4 \quad (8.3)$$

$$\sigma = 0.018 \pm 0.002 \text{ GeV}^2/c^4 \quad (8.4)$$

The  $\eta$  yield, defined as the integral of the fitted signal in the  $3\sigma$  region around the fitted mean, was obtained as:

$$Y = 3,900 \pm 700.$$

The error of the yield, the mean and the sigma result from uncertainties in the determination of the background.

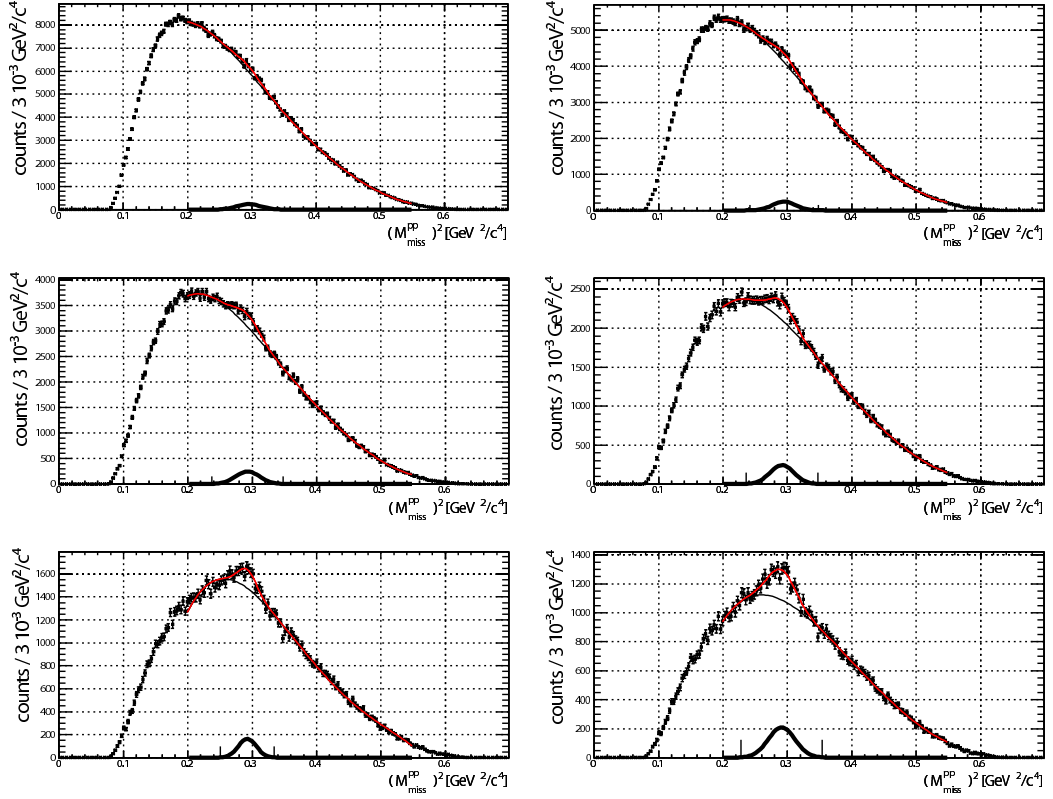


**Figure 8.12:** Effect of the of the selections as shown in the fig. 8.11 on the proton-proton missing mass squared.

The value of the fitted  $\eta$  mass is obtained from the square root of the value given in 8.3

$$M_\eta = 543 \pm 6 \text{ MeV}/c^2.$$

The width in the natural scale is calculated as:

$$\sigma(m) = \frac{1}{2} \frac{1}{\sqrt{M_\eta^2}} \sigma(M_\eta^2), \quad (8.5)$$

and hence the final figure for the fitted sigma is:

$$\sigma(m) = 16.6 \pm 1.8 \text{ MeV}/c^2.$$

### 8.4.3 Simulations.

To compare with the experimental results, 250 million proton–proton collisions in the same energy range as the January 2004 beam time were simulated [Sai05a, Sai05b]. Events were generated using the PLUTO [Kag05] event

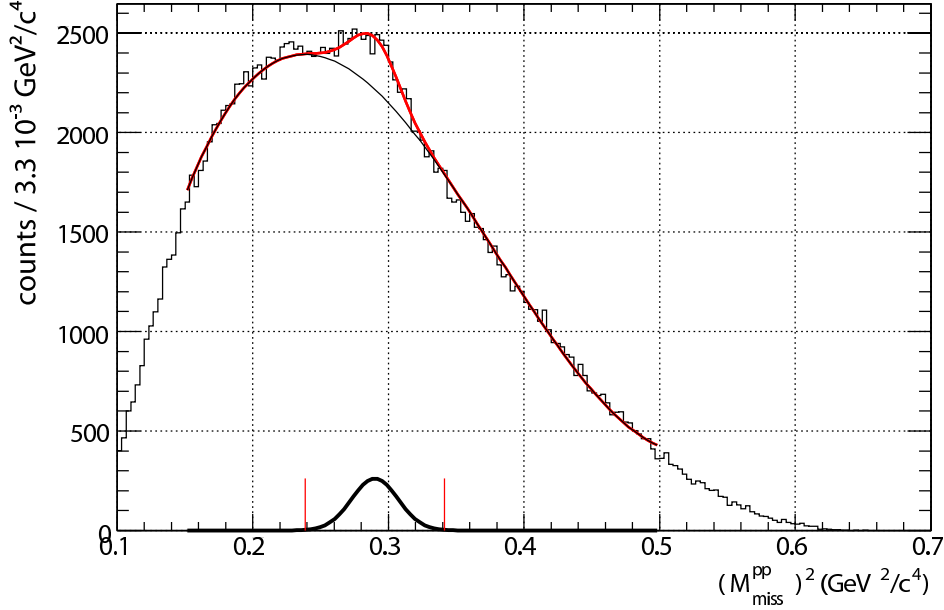


**Figure 8.13:** Missing mass of the 2 protons with the condition  $\frac{P_t^2}{2} + (P_l - 26)^2 > 3200 \text{ MeV}/c^2$  (the fourth circle in the fig. 8.11).

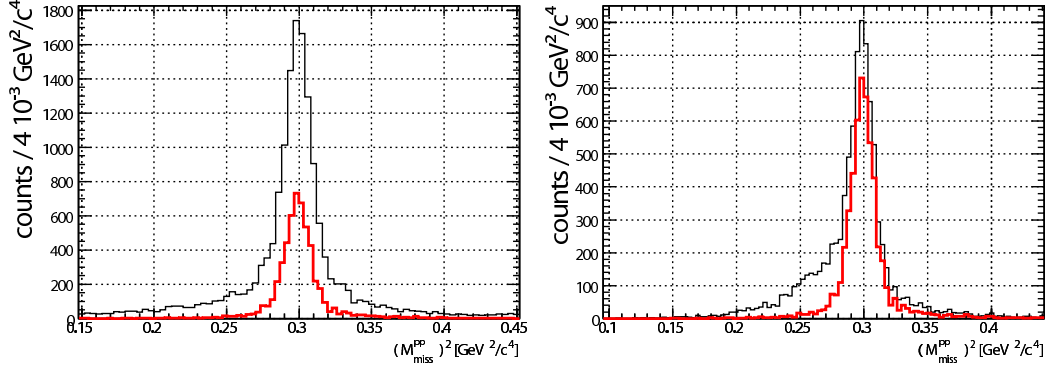
generator with a *cocktail* of known branching ratios [Prz05]. The simulated produced particles are then tracked through a simulated HADES detector. The interaction of the particles with the material of the detector as well as the geometry of the detector itself were described using the HGEANT [Hol05] simulation package; a software tool based on the GEANT3 Detector description and simulation tool [Gea].

Figure 8.9 shows the simulated  $(M_{miss}^{pp\pi^+\pi^-})^2$  distribution for the hadronic  $\eta$  decay. It is apparent that in the region around 0  $\text{GeV}^2/c^4$ , still approximately half of the events originate from the tails of the  $\eta$  decay to  $\pi^+\pi^-\pi^0$ .

The histogram in the right panel of figure 8.14 was obtained applying the same selection filters explained before on the simulations. On the  $3\sigma$  region around the fitted  $\eta$  mass, the number of  $\eta$  decaying to  $\pi^+\pi^-\gamma$  is 6,493 out of the total number of etas: 10,493. This represents a fraction of 62% from the total  $\eta$  yield in the peak:

$$\frac{\eta_{\pi^+\pi^-\gamma}(3\sigma)}{\eta_{TOTAL}} = 62 \pm 2\%$$

To be able to extract the  $\eta$  signal out of the large experimental background, very tight filtering of the data was required. In our simulations we can see



**Figure 8.14:** Proton – proton missing mass squared for simulated  $\eta$ 's. On the left comparison of the  $\eta$  yields before and after applying the selection conditions. Right, comparison of the total  $\eta$  yield (black) and the  $\eta \rightarrow \pi^+\pi^-\gamma$  yield (red).

that the number of  $\eta$  surviving all the selection conditions were 6,493 while the total number of  $\eta \rightarrow \pi^+\pi^-\gamma$  tracked with HADES were 14,197 (left panel of fig. 8.14). Thus the 46% of the events survive the cuts:

$$\frac{\eta_\gamma(\text{After})}{\eta_\gamma(\text{Before})} = 46 \pm 1\%.$$

The errors quoted in the last two figures are purely statistical.

With these figures we may scale the value of the experimental  $\eta$  yield to get an estimation of the total number of  $\eta \rightarrow \pi^+\pi^-\gamma$  tracked by HADES. This value can be calculated as the product of the original eta yield times the fraction of  $\eta$  to  $\pi\pi\gamma$  over all  $\eta$ 's, divided by the fraction of  $\eta$  which survived the selection filters (eq. 8.6):

$$Y_{\eta \rightarrow \pi\pi\gamma} = \frac{Y \cdot 0.62}{0.46}, \quad (8.6)$$

$$Y_{\eta \rightarrow \pi\pi\gamma} = 5,500 \pm 990.$$

#### 8.4.4 Energy Distribution of the Missing Gamma.

After the successfully identification of the  $\eta$  signal in the  $\eta \rightarrow \pi^+\pi^-\gamma$  channel the distribution of the energy carried away by the missing photon has been studied.

The experimental photon energy distribution from our study is shown as red crosses in figure 8.15.

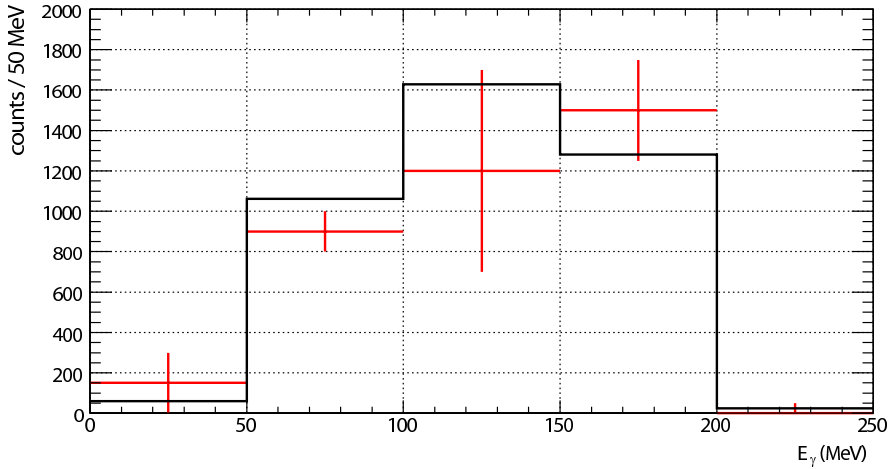


**Figure 8.15:** Energy distribution of the missing gamma. In red experimental data. Black, simulations.

In order to compare the experimental results to a simulation, 1,000,000 simulated events were generated and filtered through the HADES acceptance (black histogram in fig. 8.15). These simulations have been generated using a very simple event generator which just follows the phase space. This seems to show reasonable agreement between simulation and data for the HADES case, although statistics are limited and the systematic errors are large.

However, figure 8.16 shows a comparison between published data (Gormley *et al.*, 1970 [Gor70]) and the simple event generator we used. In this figure, the [Gor70] data are depicted with blue crosses, and simulation is drawn as a full black line. Both histograms have been scaled to the same number of entries. In this case the two  $E_\gamma$  distributions show a significantly different shape, indicating that the matrix elements used in the PLUTO event generator are not describing the reaction dynamics correctly. As mentioned in sec. 8.3.3, the particle distribution on the event generator level was based upon pure phase space. The above [Gor70] data clearly show a deviation from the phase space distribution.

A possible explanation is the orbital angular momentum in the  $\eta$  decay, possibly not correctly modelled in the simulation. In terms of  $J^p$  quantum numbers, the decay  $\eta \rightarrow \pi^+\pi^-\gamma$  can be written as  $0^- \rightarrow 0^-0^-1^-$ . Two important factors can be seen:

1. The total angular momentum on the left hand side is 0, on the right hand side is 1. Thus, at least an orbital angular momentum  $L=1$  must

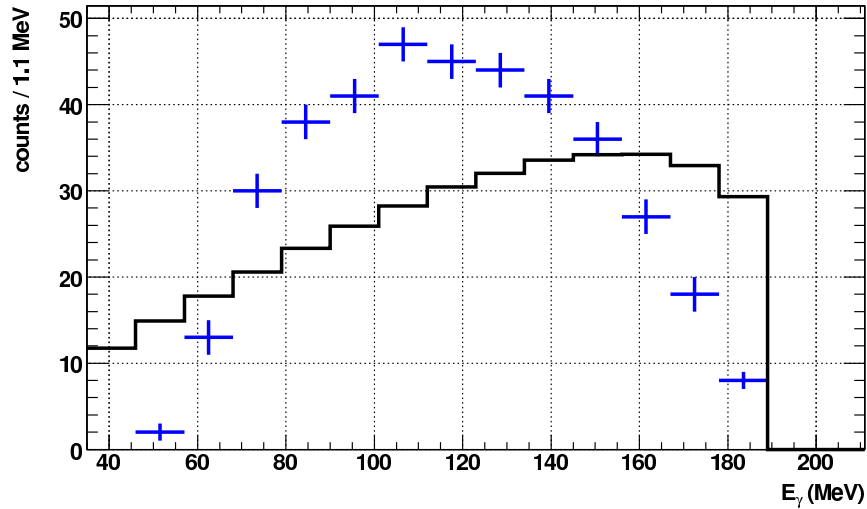


**Figure 8.16:** Data from [Gor70] compared with our simple event generator.

be present in the final state.

2. An  $L=1$  orbital angular momentum must be considered in the parity calculation. It leads to a positive final state parity, which does not agree with the parity of the initial  $\eta$ .

This indicates that there might be a  $L=1$  orbital angular momentum in the  $(\pi\pi, \gamma)$  system and a  $l = 1$  orbital angular momentum in the  $(\pi, \pi)$  system. These complicated final state interactions are not taken into account in the simulations yet.

At this stage, new simulations which include the matrix elements and angular distributions obtained by previous experiments [Gor70, Ams95, Bal04b] are necessary to compare to our data.

On the other hand, future HADES proton-proton beamtimes should provide an order of magnitude more statistics than the data set of January of 2004. Also, together with an improved kinematical refit will provide a better signal characterization and hence smaller experimental errors.

## 8.5 Comparison $\eta_\gamma/\eta_{\pi^0}$

One of the main motivations to study elementary reaction with HADES resides on the fact that the simplicity (low multiplicity) of the reactions allows to select exclusively some channels. Channels with known branching ratios and decay modes can be used to calibrate the acceptance as well as to establish how well do we understand the different features of our detector.

In this line we have presented the exclusive reconstruction of the two mayor charged decay modes of the  $\eta$  meson;  $\eta \rightarrow \pi^+\pi^-\pi^0$  and  $\eta \rightarrow \pi^+\pi^-\gamma$ . Both reactions are very similar from the detector's point of view. They have the same four charge particle produced:

$$pp \rightarrow pp\eta \rightarrow pp\pi^+\pi^-$$

where in one case the  $\pi^0$  is missing and in the second case the photon is missing.

On the table 8.3 we have a comparison of the yields of the exclusive reconstruction of the  $\eta$  decay in the two mentioned channels. The numbers of the first column, *SIM*, correspond to the number of tracked  $\eta$ , i.e. the number of  $\eta$  that could be, in principle, reconstructed. Due to the fact that both  $\eta$  decays are very similar, it can be assumed that the number of tracked  $\eta$  should be, at least in a first order, similar to the number of  $\eta$  actually reconstructed. The fact that both ratios on the table 8.3 agree, implies that the simulated acceptance and efficiency of HADES have been properly simulated, i.e. it is well understood, at least at the accuracy level of the estimated errors.

	SIM	EXP	pdg2004 [Eid04]
$\pi^+\pi^-\gamma$	15,400	$5,500 \pm 990$	4.68%
$\pi^+\pi^-\pi^0$	50,400	$21,000 \pm 1000$	22.6%
ratio	0.30	$0.26 \pm 0.06$	0.21

**Table 8.3:** Ratios between the branching ratios of  $\eta \rightarrow \pi^+\pi^-\gamma$  and  $\eta \rightarrow \pi^+\pi^-\pi^0$  for simulations, experimental data and literature value.

These results are not acceptance corrected. Hence the experimental ratio of  $\eta \rightarrow \pi^+\pi^-\gamma$  to  $\eta \rightarrow \pi^+\pi^-\pi^0$  do not match the literature value [Eid04]. Even though both channels studied have similar acceptances, they are not exactly equal, as the average momenta carried by  $\pi^0$  and  $\gamma$  are different.



# Conclusion



# Summary and Discussion

This thesis has presented the work performed for the HADES experiment at GSI Darmstadt.

One of the main objectives of HADES is to study of the properties of mesons in nuclear media. Any possible change in mass or width of mesons, when embedded in a nuclear medium, may be related to a partial restoration of chiral symmetry in dense environments. The understanding of this chiral symmetry restoration may provide a valuable insight into the basic mechanism of hadron mass generation.

More specifically, HADES is optimized to investigate the decay of vector mesons to  $e^+e^-$  pairs in heavy ion reactions. The dielectron channel was chosen because electrons, as non strong interacting particles, are very likely to leave the dense medium without interaction and hence, the reconstruction of the properties of the original meson is independent of any model or simulation.

The dielectron spectrum in the invariant mass region below the vacuum mass of the  $\rho$  meson is dominated by the  $\eta$  Dalitz decay;  $\eta \rightarrow e^+e^-\gamma$ . This is exactly the region where the mass of light vector mesons ( $\rho$  and  $\omega$ ) may be shifted to. The study of the characteristics and yield of the  $\eta$  meson is, therefore, very important as a reference measurement for HADES.

The work conducted in this thesis can be divided into two parts. A technical part which deals with the hardware developments for the trigger system and a more physics motivated part about the analysis of the production of the  $\eta$  meson.

The trigger system is very important to enhance the lepton content of the HADES data. As part of this work the trigger distribution system was improved and updated. The existing implementation of the DTU (detector trigger unit) modules was based on static schematics hard linked the actual architecture being used up to now. The design of the DTU was change from a schematic based design to solution based on VHDL code. This makes the

new DTU design architecture independent, easier to maintain, upgrade and portable to any new readout/trigger hardware the may come.

As a matter of fact, the new DTU design has been already successfully ported and embedded into the new readout module developed for the RPC detector, one of the HADES upgrade projects (see below).

In the second, more physics motivated, part of this thesis, the  $\eta$  meson production in the reaction  $pp \rightarrow pp\eta$  at an incident beam energy of 2.2 GeV has been investigated. The  $\eta$  meson decays into several final states which are accessible by HADES:

$$\eta \rightarrow \pi^+\pi^-\pi^0$$

$$\eta \rightarrow \pi^+\pi^-\gamma$$

$$\eta \rightarrow e^+e^-\gamma.$$

From these, this thesis focuses on the analysis of the hadronic final states,  $\pi^+\pi^-\pi^0$  and  $\pi^+\pi^-\gamma$ , whereas the electromagnetic decay channel is studied in [Spa05a] and [Spr06].

For the identification of  $\eta$  decays, the event hypothesis software framework has been developed and tested within this thesis.

The event hypothesis framework is a tool to help in the analysis of exclusive reactions, i.e. when all or all except one of the decay products of a reaction are detected.

The whole analysis of the hadronic  $\eta$  decays presented in this thesis has been performed using the framework, which centralizes all the non physics related work (like file accesses, the access of objects inside ROOT trees, etc.) and provides a unique and easy to use interface to the developer. Another advantage of this framework is that provides a tree like structure for the analysis, where several *algorithms* can be concatenated either in one or in several branches. It also allows to save the analysis after the completion of any step. This way, the whole analysis can be pipelined into smaller steps; which permits to save some work, as some algorithms needed by all developers (selection of events with polarity “+++” or the calculation of basic variables like the  $M_{miss}^{pp}$ ) can be ran at the beginning and only once.

In total, 25,000 eta decays have been analysed. From those, the decay to three pions,  $\eta \rightarrow \pi^+\pi^-\pi^0$  with a branching ratio of 22.6% [Eid04] yielded 21,000 events. The Dalitz analysis of this channel confirmed the observation

of the DISTO experiment [Bal04b] that the  $\eta$  production at this energy is dominated by the intermediate  $N^*(1535)$  resonance. This analysis increases the statistics of DISTO by around a factor 10.

For the first time at HADES, the decay channel  $\eta \rightarrow \pi^+\pi^-\gamma$  with a branching ratio as low as 4.68% [Eid04] has been clearly identified. This channel differs from the previous  $\eta \rightarrow \pi^+\pi^-\pi^0$  as pions have spin 0 and the gamma has spin 1. Therefore, whereas the decay to three pions is pure s-wave final state with orbital momentum  $L=0$ , in the decay to two pion and a photon either the two pions or the dipion relative to the photon are in a relative p-wave with  $L=1$ . An analysis of the photon energy distribution has been made and the results compared to [Gor70]. Unfortunately, a Dalitz analysis of this channel could not be performed due to insufficient statistics and due to the difficulties to isolate this channel. The reconstruction of the  $\eta \rightarrow \pi^+\pi^-\gamma$  channel is more difficult than the  $\eta \rightarrow \pi^+\pi^-\pi^0$  because of the larger background in the region with  $M_{miss}^{pp\pi^+\pi^-} = 0$ .

The reconstructed yields of both decay channels agree with each other and agree with the simulations. This is a clear indication of the very good performance of HADES for the exclusive reconstruction of meson decay in pp collisions in the few GeV region.

Complementary to this thesis, the  $\eta$  decay to  $e^+e^-\gamma$  is, as well, being analysed for HADES [Spa05a, Spr06].

The  $\eta$  signal in this channel is known to be dominated by the decay of eta to two photons where one of the photons converts into an  $e^+e^-$  pair,  $\eta \rightarrow 2\gamma \rightarrow e^+e^-\gamma$ . This effect may account for up to 80 % of the signal in the eta region according to our actual simulations [Spr06]. Very tight cuts have to be applied to the data in order to extract the  $\eta \rightarrow e^+e^-\gamma$  signal from the background of photon conversion. These cuts reduce the statistics notably so that the remaining signal have only in the order of 100 counts [Spr06].

The HADES pp program will continue in the next few years. In May 2006, HADES recorded 700 million inelastic events in pp collisions at 1.275 GeV. The analysis of this new data sample is currently underway. For January 2007 a new experiment with pp at 3.5 GeV is envisaged. The main goal of this data taking is the investigation of the channel  $pp \rightarrow pp\omega$ .

The analysis in this thesis has been performed with a tracking system of three layers of drift chambers. This year HADES has completed the installation of the fourth layer of drift chambers. With this new layer the HADES tracking

system is complete to its full extension. With the full four layers of drift chambers the momentum resolution of HADES will improve by a factor of 3 to 4 depending upon particle species and particle momentum.

In addition several upgrades are planned for HADES in the near future.

A new time of flight detector with 1024 RPC (resistive plate counters) with an improved time resolution of 100 ps has succeed its R&D phase and it is being currently tested. The new DTU implementation for the trigger distribution system, developed in the frame of this thesis, has been already ported to the RPC readout system and successfully tested.

A forward hodoscope will be installed to cover the polar angles below 7 degrees. This is of major importance in the exclusive reconstruction of mesons, as it will improve the probability of detecting spectator protons (the  $p_1$  proton in the Dalitz plot of fig. 8.8) in reactions such as  $pp \rightarrow pN^* \rightarrow pp\eta$ .

A new quadrupole magnet in the target region has been commissioned for experiments with pion beams. With pion beams, different  $N^*$  resonances can be excited compared to proton beams.

Within this thesis it was demonstrated that HADES is well suited for the investigation of meson production in pp collisions, and thus prepared for the investigation of meson production in nucleus-nucleus collisions.

# List of Figures

1.1	Rotation curve of NGC 6503. The dotted, dashed and dash-dotted lines are the contributions of gas, disk and dark matter, respectively [Beg91]. . . . .	14
1.2	The Cosmic Microwave Background, CMB. From [NAS]. . . . .	15
1.3	Masses of the six quark flavours. Masses generated by electroweak symmetry breaking ( <i>current quark mass</i> ) are shown in blue. The additional term portion of the light quarks mass, generated by chiral symmetry breaking in QCD ( <i>constituent quark mass</i> ) are shown in yellow [Mul04]. . . . .	16
2.1	The QCD phase diagram. Red dots show the experimental freeze-out parameters deduced from hadro-chemical analyses of particle production yields at SIS, AGS and SPS energies[Bra98b, Bra01, Sto99]. The Pink line is the Cleymans-Redlich curve $E/N = 1\text{GeV}$ [Cle98]. The blue line represents the phase boundaries calculated from Lattice QCD [Fod01]. . . . .	18
2.2	The <i>Mexican Hat</i> potential, a mechanical example of spontaneous symmetry breakdown. . . . .	21
2.3	The quark condensate value as a function of the nuclear matter temperature (T) and the density ( $\rho$ ) according to the Nambu-Jona-Lasinio (NJL)[Nam61] model, from [Kli90, Wei93]. . . . .	22
2.4	Calculated spectra of current-current correlation functions. The dashed lines show the vacuum spectra in the $\rho$ and $\omega$ channels normalised such that they can be compared directly with the corresponding $e^+e^- \rightarrow$ hadrons data. The long dashed and solid lines show the spectral functions in nuclear matter at densities $\rho_0/2$ and $\rho_0 = 0.17 = fm^{-3}$ (figures from [Kli98]). . . . .	23
2.5	Resonance-hole self-energy diagrams for the rho meson. The double dashed line stands for a physical rho meson that contains the $\pi\pi$ -width [Pet98]. . . . .	24

2.6	Self-consistent spectral function of the rho meson for $\rho_N = \rho_o$ . On the right: Cuts through the spectral function for different three-momenta together with the vacuum spectral function [Pet98]. . . . .	25
3.1	Low-mass dilepton experiments at a glance . . . . .	27
3.2	Dielectron invariant mass spectra from the KEK-PS E325 experiment obtained with a Carbon target (up) and a Cooper target (down). In red sum of all known sources and green, estimated combinatorial background. An enhancement $e^+e^-$ pairs below the $\omega$ meson mass is apparent, as well as the <i>dissolving</i> of the $\rho$ meson [Nar05]. . . . .	28
3.3	DLS measurements of the dielectron cross sections from (a) Ca+Ca, (b) C+C, (c) He+Ca and (d) d+Ca reactions. Panel (a) also contains the calculated signal from BUU simulations and histograms showing the $\pi^0$ and $\eta$ decay contributions as estimated from TAPS measurements and an isotropic thermal model. The dashed line represents the $\eta$ component of the BUU calculations. The solid lines in the four panels show fits to the low-mass data using $\pi^0$ and $\eta$ decay estimate with adjustable normalisations [Por97]. . . . .	29
3.4	Dielectron mass spectrum with the hadron decay cocktail (left) and with the models (right). The spectrum contains $2571 \pm 224$ $e^+e^-$ pairs with $M_{inv} > 0.2$ GeV/c <sup>2</sup> , with the signal to background ratio of 1:21. The multiplicity of charged particles, averaged over event centralities and over the acceptance, is $\langle dN_{ch}/d\eta \rangle = 335$ [Mis05]. . . . .	30
3.5	Experimental dimuon spectrum (open circles) from In-In collisions at 158 AGeV recorded by the NA60 [Arn06] experiment. The triangles show the excess of dimuon yield over the hadronic decay cocktail. On the right, comparison of the excess spectrum with various theoretical predictions for the $\rho$ meson in-medium. free $\rho$ , solid thin line. The thick solid line depict in-medium broadening [Cha96, Rap00] models and the dotted-dashed line models predicting broadening plus shifting [Bro91] of the $\rho$ mass (event though the actual calculation of this curve is arguable, see recent letters of Brown and Rho in [Bro05]). . . . .	31

3.6	Left: $\pi^0\gamma$ invariant mass spectrum for Nb data (solid histogram) and LH <sub>2</sub> data (dashed histogram) after background subtraction. Right: In-medium decays of the $\omega$ meson. The vertical dashed line indicates the vacuum $\omega$ mass [Trn05]. . . . .	32
4.1	View of the HADES spectrometer at GSI. The beam (green line) enters the set up at a height of 2.5 m [Sch06]. . . . .	38
4.2	Extended view of HADES with all its subdetectors [Sch06]. . . . .	39
4.3	Reconstruction of two different targets. . . . .	40
4.4	Photograph of the LH2 target cell. . . . .	40
4.5	The start and veto . . . . .	41
4.6	The RICH detector . . . . .	43
4.7	Vertical cut (left) and front view (right) of the superconducting toroid (schematically). 6 coils are mounted in individual vacuum chambers which are connected by a support ring upstream of the target. A hexagonal front plate compensates the magnetic forces between the coil cases. . . . .	45
4.8	The MDC detector. The labels in (b) illustrate where each plane has been produced. . . . .	46
4.9	The SHOWER detector. Three gas chambers and two lead converters. Lepton/hadron discrimination is done by comparing the number of particles before and after the lead converters. . . . .	47
4.10	Photograph of the <i>Time Of Flight</i> , <b>TOF</b> , detector. The 6 sector symmetry is apparent. . . . .	49
4.11	Photograph of one of the TOF Photomultipliers together with the curved light guides used to couple them to the scintillating rods. . . . .	50
4.12	Schematic view of the <b>TOFino</b> detector with the four scintillator plates per sector. . . . .	51
5.1	The two levels of the HADES Trigger System. . . . .	53
5.2	Histogram of charged particle multiplicities in simulated Au+Au collisions at 1 AGeV for several impact parameters $b$ [Gar93]. . . . .	54
5.3	Data flow in the HADES trigger. After the LVL1 trigger, data are read out and stored in the first level pipe. Then, the system waits for the LVL2 trigger. If the LVL2 trigger is positive the data will be forwarded to the event builder, else they will be discarded. . . . .	55
5.4	Block diagram of the RICH Image Processing Unit [Leh99]. . . . .	56

5.5	Ring recognition searching mask. The ring region and the inner/outer veto regions are shown. Pads are not added individually, but rather grouped to save resources [Leh99]. . . . .	57
5.6	Simulation of velocity distribution for different particle species in central Au+Au collisions. Separation based on velocity is more effective for polar angles $> 45^\circ$ (right) than for angles below $45^\circ$ (left) [Gar93]. In that region the TOF measurements are complemented with the production of electromagnetic avalanches in the Pre-Shower detector. . . . .	58
5.7	Block diagram of the Image Processing Unit of the Time-Of-Flight detector . . . . .	59
5.8	Scheme of an electromagnetic <i>shower</i> with the 3x3 pad integration area depicted. . . . .	60
5.9	Diagram of the functional blocks of the Shower IPU. Black arrows show the data flow [Pet00]. . . . .	61
5.10	$\Delta\phi$ ( $\phi_{\text{RICH}} - \phi_{\text{META}}$ ) as a function of $\phi_{\text{RICH}}$ of all the leptons found by the Matching Unit. All the hits are inside the azimuthally variable matching window, marked in red [Toi04].	62
5.11	Block diagram of the Matching Unit [Tra01]. . . . .	63
5.12	Schematic view of the Trigger Distribution System [Lin01]. . .	64
5.13	Timing diagram on the trigger bus. The total transmission time is $1 \mu\text{s}$ ; TB is kept high longer to account for delays in the lines and reaction time of the different subsystems. . . . .	66
5.14	Diagram of the logic blocks in the DTU/CTU VME module [Lin01]. . . . .	67
5.15	Block diagram of the basic functions in the DTU's FPGA. . .	69
5.16	Block diagram of the TOF DTU. . . . .	70
5.17	Diagram of the communication DTU-MDC system. . . . .	71
5.18	Comparison of the $e^+e^-$ pair probability per event for LVL2 triggered data (red squares) and untriggered data (blue stars), both normalized to the same number of LVL1 triggers. It is apparent that by using the LVL2 trigger the lepton content of the sample is enhanced by an order of magnitude [Toi04]. . . . .	72
6.1	Schematic view of the HADES data flow. . . . .	78
7.1	Structure of the Event hypothesis Framework for the analysis of elementary reactions with HADES [Frö05]. . . . .	86
7.2	Example of combinations for the reaction target $pp \rightarrow pp\eta \rightarrow pp\pi^+\pi^-\pi^0$ . The four charged particles are tracked, therefore the number of combinations is three. . . . .	87

7.3	The Delta TOF method. The identity selection power is apparent. Simulated events proton-proton at 2.2 GeV kinetic energy. . . . .	89
8.1	Two dimensional plots generated from all the combinations before any selection criteria were applied. . . . .	94
8.2	Effect of the selection of events with $M_{miss}^{pp} > M_{inv}^{\pi^+\pi^-}$ on the proton-proton missing mass squared vs. 4 particle missing mass squared. . . . .	95
8.3	Effect of the selection $M_{miss}^{pp} > M_{inv}^{\pi^+\pi^-}$ on the $\pi\pi$ invariant mass squared versus the missing mass of the two protons proton histogram. . . . .	96
8.4	Missing mass of the four outgoing particles under the condition $M_{miss}^{pp} > M_{inv}^{\pi^+\pi^-}$ . Fit done with a polynomial grade 4 plus a Gaussian function. . . . .	97
8.5	Final proton proton missing mass histogram after a kinematic refit and the selections explained. The fit was performed with a polynomial grade 5 plus a Gaussian. . . . .	99
8.6	$\eta$ angular distribution. . . . .	100
8.7	Ratio of the experimental over the simulated distributions of figure 8.6 (a). . . . .	101
8.8	Dalitz plots of the $\eta$ decay. On the X axis invariant mass squared distribution of the low momentum proton and $\eta$ . On the Y axis the same distribution with the high energy proton. The enhancement in the region around $M_{inv}^{p_2\eta} \sim 1.5 \text{ GeV}/c^2$ corresponds to the $N^*(1535)$ resonance. . . . .	102
8.9	Four particle missing mass squared for simulated $\eta$ 's. Black line: all $\eta$ . Blue: events with $\eta \rightarrow \pi^+\pi^-\pi^0$ . Red : events with $\eta \rightarrow \pi^+\pi^-\gamma$ . In the $\gamma$ region, still around 40% of the events come from the $\eta$ decay to $\pi^+\pi^-\pi^0$ . . . . .	103
8.10	Comparison of the $P_t$ (left) and $P_l$ (right) distributions for all events (black) and events with $\eta \rightarrow \pi^+\pi^-\gamma$ (red). . . . .	104
8.11	Distribution of $P_t - P_l$ for all the combinations with 4 charged tracks after $M_{miss}^{pp} > M_{inv}^{\pi^+\pi^-}$ and $\left  (M_{miss}^{pp\pi^+\pi^-})^2 \right  < 7,500 \text{ MeV}^2/c^4$ . . . . .	105
8.12	Effect of the of the selections as shown in the fig. 8.11 on the proton-proton missing mass squared. . . . .	106
8.13	Missing mass of the 2 protons with the condition $\frac{P_t^2}{2} + (P_l - 26)^2 > 3200 \text{ MeV}/c^2$ (the fourth circle in the fig. 8.11). . . . .	107

- 8.14 Proton – proton missing mass squared for simulated  $\eta$ 's. On the left comparison of the  $\eta$  yields before and after applying the selection conditions. Right, comparison of the total  $\eta$  yield (black) and the  $\eta \rightarrow \pi^+\pi^-\gamma$  yield (red). . . . . 108
- 8.15 Energy distribution of the missing gamma. In red experimental data. Black, simulations. . . . . 109
- 8.16 Data from [Gor70] compared with our simple event generator. 110

# Bibliography

- [Abr96a] M. C. Abreu *et al.* (NA50 Coll.). Nucl. Phys. **A610** (1996) 331.
- [Abr96b] M. C. Abreu *et al.* (NA38 Coll.). Phys. Lett. B **368** (1996) 230.
- [AD] Analog Devices, Inc. Norwood, MA, USA. <http://www.analog.com>.
- [Ago02] C. Agodi *et al.* Nucl. Inst. & Meth. **A492** (2002) 14.
- [Alv04] H. Alvarez Pol *et al.* Nucl. Inst. & Meth. **A535** (2004) 277.
- [Ams95] C. Amsler *et al.* (Cristal Barrel Coll). Phys. Lett. B **346** (1995) 203.
- [Arn06] R. Arnaldi *et al.* (NA60). Phys. Rev. Lett. **96** (2006) 162302. [nucl-ex/0605007](http://arxiv.org/abs/nucl-ex/0605007).
- [Ave97] R. Averbeck *et al.* (TAPS Coll.). Z. Phys. **A359** (1997) 65.
- [Bal98] A. Bałanda *et al.* Nucl. Inst. & Meth. **A417** (1998) 360.
- [Bal04a] A. Bałanda *et al.* Nucl. Inst. & Meth. **A531** (2004) 445.
- [Bal04b] F. Balestra *et al.* (DISTO Coll.). Phys. Rev. **C69** (2004) 064003.
- [Bar77] B. C. Barrois. Nucl. Phys. **B129** (1977) 390.
- [Bas98] S. A. Bass *et al.* (UrQMD). Prog. Part. Nucl. Phys. (1998) 225. UrQMD web-site: <http://www.th.physik.uni-frankfurt.de/~urqmd/>.
- [Beg91] K. Begeman, A. Broeils and R. Sanders. MNRAS **249** (1991) 523.
- [Ber99] E. Berdermann. Nucl. Phys. B (*Proc. Suppl.*) **78** (1999) 533.
- [Ber04] G. Bertone, D. Hooper and J. Silk. [hep-ph/0404175](http://arxiv.org/abs/hep-ph/0404175) (2004).

- [Bic] Bicron is a registered trademark of Compagnie de Saint-Gobain, Les Miroirs - 18, avenue d'Alsace - 92 400 Courbevoie - France. <http://www.bicron.com>.
- [Böh99] M. Böhmer. Das Auslesesystem für den Ringabbildenden Cherenkovdetektor im HADES Spektrometer. Master's thesis, Institut E12 – T.U. München (1999).
- [Bra98a] E. L. Bratkovskaya *et al.* Nucl. Phys. **A634** (1998) 168. [nucl-th/9710043](http://nucl-th/9710043).
- [Bra98b] P. Braun-Munzinger and J. Stachel. Nucl. Phys. **A638** (1998) 3.
- [Bra99] E. L. Bratkovskaya and C. M. Ko. Phys. Lett. **B445** (1999) 265. [nucl-th/9809056](http://nucl-th/9809056).
- [Bra01] P. Braun-Munzinger. Nucl. Phys. **A681** (2001) 119.
- [Bre99] T. Bretz. Magnetfeldeigenschaften des Spektrometers HADES. Ph.D. thesis, T.U. München (1999).
- [Bro91] G. E. Brown and M. Rho. Phys. Rev. Lett. **66** (1991) 2720.
- [Bro05] G. E. Brown and M. Rho. [nucl-th/0509001](http://nucl-th/0509001) and [nucl-th/0509002](http://nucl-th/0509002) (2005).
- [Bru06] R. Brun and F. Rademakers. ROOT, an Object Oriented Data Analysis Framework. <http://root.cern.ch> (2006).
- [Cas95] W. Cassing, W. Ehehalt and C. Ko. Phys. Lett. **B363** (1995) 35.
- [Cas99] W. Cassing and E. L. Bratkovskaya. Phys. Rev. **308** (1999) 65. HSD web-site: <http://www.th.physik.uni-frankfurt.de/~brat/hsd.html>.
- [Cha92] G. Chanfray and P. Schuck. Nucl. Phys. **A545** (1992) 271c.
- [Cha96] G. Chanfray, R. Rapp and J. Wambach. Phys. Rev. Lett. **76** (1996) 368.
- [Che37] P. A. Cherenkov. Dokl. Akad. Nauk. SSSR [Sov. Phys. Dokl.] **2** (1937) 37.
- [Cle98] J. Cleymans and K. Redlich. Phys. Rev. Lett. **81** (1998) 5284.

- [Coh92] T. D. Cohen, R. J. Furnstahl and D. K. Griegel. Phys. Rev. C **45** (1992) 1881.
- [Dir28] P. A. M. Dirac. Proc. Roy. Soc. London **A117** (1928) 610.
- [Dru90] E. G. Drukarev and E. M. Levin. Nucl. Phys. **A511** (1990) 679.
- [Eid04] S. Eidelman *et al.* Review of Particle Physics. Phys. Lett. B **592** (2004).
- [Fab03a] L. Fabbietti. Study of the  $e^+e^-$  pair acceptance in the dilepton spectrometer HADES. Ph.D. thesis, T.U. München (2003).
- [Fab03b] L. Fabbietti *et al.* Nucl. Inst. & Meth. **A502** (2003) 256.
- [Fod01] Z. Fodor, S.D. Katz. [hep-lat/0106002](https://arxiv.org/abs/hep-lat/0106002) (2001).
- [Fri73] H. Fritzsch, M. Gell-Mann and H. Leutwyler. Phys. Lett. **B 47** (1973) 365.
- [Fri97] B. Friman and H. Pirner. Nucl. Phys. **A617** (1997) 496.
- [Fri99] J. Friese *et al.* Nucl. Inst. & Meth. **A438** (1999) 86.
- [Fri03] J. Friese *et al.* Nucl. Inst. & Meth. **A502** (2003) 241.
- [Frö02] I. Fröhlich. Untersuchungen zur  $\eta$ -Produktion in  $pp$ -Reaktionen mit dem DISTO- und HADES-Spektrometer. Ph.D. thesis, Justus Liebig Universität Gießen (2002).
- [Frö05] Event Hypothesis picture courtesy of I. Fröhlich, University of Frankfurt (2005).
- [Fuc04] C. Fuchs and A. Faessler. [nucl-th/0402102](https://arxiv.org/abs/nucl-th/0402102) (2004).
- [Gar93] K. Garrow. HADES simulation of TOF and SHOWER (1993).
- [gcc06] GCC, the GNU Compiler Collection. <http://gcc.gnu.org> (2006).
- [Gea] GEANT - A Detector Description and Simulation Tool. <http://wwwasd.web.cern.ch/wwwasd/geant/index.html>.
- [Gla61] S. Glashow. Nucl. Phys. **20** (1961) 179.
- [Gor70] M. Gormley *et al.* Phys. Rev. D **1** (1970) 501.
- [HAD] HADES. <http://www-hades.gsi.de>.

- [HAD94] HADES Collaboration. A proposal for a high acceptance dielectron spectrometer. [GSI Darmstadt](#) (1994).
- [Her92] M. Herrmann, B. Friman and W. Nörenberg. Nucl. Phys. **A545** (1992) 267c.
- [Hig64] P. Higgs. Phys. Rev. Lett. **13** (1964) 508.
- [Hol05] R. Holzmann *et al.* The HADES simulation package HGeant. <http://www-hades.gsi.de/holzmann/hadsimul.html> (2005).
- [Kag05] M. A. Kagarlis *et al.* Pluto++, a ROOT based event generator. <http://www-hades.gsi.de/computing/pluto/html/PlutoIndex.html> (2005).
- [Kan04] K. Kanaki *et al.* IEEE Trans. Nucl. Sci. **51** (2004) 939.
- [Kli90] S. Klimt, M. Lutz and W. Weise. Phys. Lett. **B 249** (1990) 386.
- [Kli96] F. Klingl and W. Weise. Nucl. Phys. **A606** (1996) 329.
- [Kli98] F. Klingl, W. Weise. [hep-ph/9802211](#) (1998).
- [Koc95] V. Koch. [nucl-th/9512029](#) (1995).
- [Koe06] I. Koenig. [Status of Runge Kutta tracking in HYDRA](#). Technical report, GSI (2006).
- [Lan85] L. G. Landsberg. Phys. Rep. **128** (1985) 301.
- [Leh99] J. Lehnert *et al.* Nucl. Inst. & Meth. **A433** (1999) 268.
- [Leh03] J. Lehnert *et al.* Nucl. Inst. & Meth. **A502** (2003) 261.
- [LEP05] LEP Electroweak Working Group, status of summer 2005. <http://lepewwg.web.cern.ch/LEPEWWG/> (2005).
- [Leu98] S. Leupold, W. Peters and U. Mosel. Nucl. Phys. **A628** (1998) 311. [nucl-th/9708016](#).
- [LHC] LHC, Large Hadron Collider. <http://lhc.web.cern.ch/lhc>.
- [Li95] G. Q. Li, C. M. Ko and G. E. Brown. Phys. Rev. Lett. **75** (1995) 4007.

- [Lin01] E. Lins. Entwicklung eines Auslese- und Triggersystems zur Leptonenidentifizierung mit dem HADES-Flugzeitdetektor. Ph.D. thesis, Justus Liebig Universität Gießen (2001).
- [Lit73] J. Litt *et al.* Cherenkov counter technique in high energy physics (1973).
- [Lut92] M. Lutz, S. Klimt and W. Weise. Nucl. Phys. **A542** (1992) 521.
- [Mar05] J. Markert. Untersuchung zum Ansprechverhalten der Vieldraht Driftkammern niedriger Massenbelegung des Hades Experiments. Ph.D. thesis, University of Frankfurt (2005).
- [Mas95] M. Masera (HELIOS-3 Coll.). Nucl. Phys. **A590** (1995) 93.
- [Mil83] M. Milgrom. ApJ **270** (1983) 365.
- [Mis05] D. Miskowiec (CERES Coll.). [nucl-ex/0511010](#) (2005).
- [Mul04] B. Muller. [nucl-th/0404015](#) (2004).
- [Mün04] C. Müntz *et al.* Nucl. Inst. & Meth. **A535** (2004) 242.
- [Myr79] J. Myrheim and L. Bugge. Nucl. Inst. & Meth. (1979).
- [Nam61] Y. Nambu and G. Jona-Lasinio. Phys. Rev. **122** (1961) 345.
- [Nar05] M. Naruki *et al.* (E325 Coll.). [nucl-ex/0504016](#) (2005).
- [NAS] NASA. <http://www.nasa.gov>.
- [Pet98] W. Peters *et al.* Nucl. Phys. **A632** (1998) 109. [nucl-th/9708004](#).
- [Pet00] M. Petri. Entwicklung eines kombinierten Auslese- und Echtzeit-Triggersystems zum Nachweis von Elektronen/Positronen-Signaturen in einem elektromagnetischen Schauerdetektor. Ph.D. thesis, Justus Liebig Universität Gießen (2000).
- [Pis95] R. Pisarki. Phys. Rev. **D52** (1995) R3773.
- [Por97] R. J. Porter *et al.* (DLS Coll.). Phys. Rev. Lett. **79** (1997) 1229.
- [Prz05] W. Przygoda. PROTON + PROTON collisions. Technical report, GSI (2005). [http://www-aix.gsi.de/~przygoda/logbook/18AUG2004/pp\\_cross\\_sections.html](http://www-aix.gsi.de/~przygoda/logbook/18AUG2004/pp_cross_sections.html).

- [Rap97] R. Rapp, G. Chanfray and J. Wambach. Nucl. Phys. **A617** (1997) 472.
- [Rap00] R. Rapp and J. Wambach. Adv. Nucl. Phys. **25** (2000) 1.
- [Rus06] A. Rustamov. *in preparation*. Ph.D. thesis, GSI – T.U. Darmstadt (2006).
- [Sai05a] B. Sailer. [DST production Simulation of Jan04, Generation 3](#). Technical report, E12, T.U. München (2005).
- [Sai05b] B. Sailer. pp Simulation DST Status. XV HADES coll. meeting, Dubna (2005).
- [Sán03] M. Sánchez. Momentum Reconstruction and Pion Production Analysis in the HADES Spectrometer at GSI. Ph.D. thesis, Universidade de Santiago de Compostela (2003).
- [Sch06] HADES pictures courtesy of A. Schmah, GSI (2006).
- [She03] K. Shekhter *et al.* Phys. Rev. **C68** (2003) 014904.
- [Shy03] R. Shyam and U. Mosel. Phys. Rev. **C67** (2003) 065202. [hep-ph/0303035](#).
- [Spa05a] S. Spataro. Characterization of the HADES spectrometer in pp collisions at 2.2 GeV: elastic scattering and exclusive eta reconstruction. Ph.D. thesis, INFN Catania (IT) (2005).
- [Spa05b] S. Spataro. In Proceedings of the XLII international winter meeting on nuclear physics. Bormio (I) (2005), (page 305).
- [Spr06] B. Spruck. HADES collaboration meeting, Dresden (2006).
- [Sri96] D. K. Srivastava, B. Sinha and C. Gale. Phys. Rev. C **53** (1996)(2) R567.
- [Sto99] R. Stock. Phys. Lett. B **456** (1999) 277.
- [Tev] Tevatron, Fermi National Accelerator Laboratory. <http://www-bdnew.fnal.gov/tevatron>.
- [Toi04] A. Toia. [Performance of the HADES Spectrometer for Dilepton Identification in the Reaction C+C at 1-2 AGeV](#). Ph.D. thesis, Justus Liebig Universität Gießen (2004).

- [Tra00] M. Traxler *et al.* IEEE Transactions in Nuclear Science **47** (2000) 376.
- [Tra01] M. Traxler. [Real-Time Dilepton Selection for the HADES Spectrometer](#). Ph.D. thesis, Justus Liebig Universität Gießen (2001).
- [Trn05] D. Trnka *et al.* (CBELSA/TAPS Collaboration). Phys. Rev. Lett. **94** (2005) 192303. [nucl-ex/0504010](#).
- [Wei67] S. Weinberg. Phys. Rev. Lett. **19** (1967) 1264.
- [Wei93] W. Weise. Nucl. Phys. **A610** (1993) 59.
- [Wei05] W. Weise. In T. Bresani, A. Filippi and U. Wiedner, editors, Proceedings of the international school of physics “Enrico Fermi”. Società Italiana de Fisica, Bologna, Italy (2005), (pages 1–34).
- [XIL] XILINX, Inc. San José CA, USA. <http://www.xilinx.com>.
- [Zwi33] F. Zwicky. Helv. Phys. Acta **6** (1933) 110.